Advanced Ceramic Materials Series Volume 2

edited by Aleksander Gurlo

Stephan van Duren

Development of in situ methods for process monitoring and control and characterization of Cu-Zn-Sn-S based thin films

Universitätsverlag der TU Berlin

Technische Universität Berlin

Stephan van Duren

Development of in situ methods for process monitoring and control and characterization of Cu-Zn-Sn-S based thin films

The scientific series *Advanced Ceramic Materials* is edited by Prof. Dr. Aleksander Gurlo.

Advanced Ceramic Materials | 2

Stephan van Duren

Development of in situ methods for process monitoring and control and characterization of Cu-Zn-Sn-S based thin films

Universitätsverlag der TU Berlin

Bibliographic information published by the Deutsche Nationalbibliothek
The Deutsche Nationalbibliothek lists this publication in the Deutsche Nationalbibliografie; detailed bibliographic data are available on the Internet at http://dnb.dnb.de.

Universitätsverlag der TU Berlin, 2019
http://verlag.tu-berlin.de

Fasanenstr. 88, 10623 Berlin
Tel.: +49 (0)30 314 76131 / Fax: -76133
E-Mail: publikationen@ub.tu-berlin.de

Zugl.: Berlin, Techn. Univ., Diss., 2018
Gutachter: Prof. Dr. Aleksander Gurlo
Gutachter: Prof. Dr. Walter Reimers
Gutachter: Dr. Thomas Unold (Helmholtz-Zentrum Berlin)
Die Arbeit wurde am 8. Oktober 2018 an der Fakultät III unter Vorsitz von Prof. Dr. Walter Reimers erfolgreich verteidigt.

Cover image: David Karl | Segerkegel | 2017

Print: Pro Business
Layout/Typesetting: Stephan van Duren

ISBN 978-3-7983-3064-1 (print)
ISBN 978-3-7983-3065-8 (online)

ISSN 2569-8303 (print)
ISSN 2569-8338 (online)

Published online on the institutional repository of the Technische Universität Berlin:
DOI 10.14279/depositonce-7732
http://dx.doi.org/10.14279/depositonce-7732

To Marijke

Es ist nicht genug, zu wissen, man muss auch anwenden.
Es ist nicht genug, zu wollen, man muss auch tun.

Man muss immer tun, was man nicht lassen kann.
- J.W. Goethe

Summary

In recent years, kesterite Cu_2ZnSnS_4 (CZTS) has become an interesting alternative to copper indium gallium (di)selenide (CIGS) due to its non-toxic and earth abundant constituents. A variety of methods is being used to fabricate kesterite thin films, such as coevaporation, sputtering, electrodeposition, spray pyrolysis and others. Most of them include an annealing step to stimulate elemental mixing and interdiffusion. Although conversion efficiencies of kesterite solar cells have increased among different research groups, the record value of 12.6 % set by IBM in 2014 has not been broken yet. Therefore, experimental and theoretical studies are needed to predict the effect of the secondary phases and detrimental defects on the electronical properties of the CZTS based solar devices.

The work presented here studies non-destructive techniques for in situ process control and monitoring. With the aim to detect phases and phase transitions to optimize crucial processing steps such as pre-annealing of metal precursors, high temperature annealing and vacuum deposition of Cu-Zn-Sn-S based thin films. The research consists of three parts in which Raman spectroscopy, X-ray diffraction (XRD) and reflectometry are used to explore this objective.

In the first part Raman spectroscopy is investigated as an in situ monitoring technique during high temperature annealing of thin films. It investigates whether the occurrence of CZTS can be monitored when it is created from

annealing a Mo/CTS/ZnS layered thin film. CuS, SnS, ZnS and CTS (Cu-Sn-S) films are prepared by physical vapor deposition. The Raman scattering intensity was compared to investigate whether their specific vibrational modes can be distinguished from each other at room temperature. Then, the CTS film is annealed between 50 and 550 °C in order to investigate whether CTS vibrational modes can be identified at elevated temperatures and to see which transitions take place within the thin film. Also, a CZTS reference film is annealed between 50 and 550 °C for reference purposes. The temperature dependence of the main CZTS modes is examined to investigate whether it can be used for in situ temperature control. Finally, a ZnS layer is deposited on the unannealed CTS film to obtain a Mo/CTS/ZnS layered film. This film is used to study the conversion of CTS/ZnS into CZTS at elevated temperatures. It was found that Raman spectroscopy can successfully be used to monitor formation of CZTS by identifying its main vibrational mode during the annealing process. The intensity of the CTS modes reduces at elevated temperatures. At 450 °C, the main CZTS mode at 338 cm^{-1} can be clearly identified.

The second part also focuses on high temperature annealing. However, in this part the focus lies on annealing of the metal precursor films. It is explored whether specific alloys benefit or hinder the formation of secondary phases during formation of the CZTS absorber films. Also, to what extent this influences solar cell performance. In situ XRD was investigated for in situ monitoring of the pre-annealing

process. Cu-poor metal precursor films are prepared by sputtering deposition. The precursors are annealed at 150 °C, 200 °C, 300 °C and 450 °C in a three zone tube furnace. The effect on the structural properties is analysed by XRD to study the formation mechanism of alloys. The precursor films are then sulfurized in a three zone tube furnace. The structural properties of the absorber are analysed and correlated with structures in the precursor. It is found that formation of SnS_2 in the absorber is proportional to the remaining Sn in the pre-annealed precursor. Also, electron micrographs showed that pre-annealing temperature influences grain growth and surface precipitation of Sn-S and Zn-S. Pre-annealed absorbers at 450 °C did not exhibit these phases on the surface. Solar devices are fabricated from the absorber films and best performing devices were obtained from pre-annealed absorbers at 450 °C. They showed absence of Sn and SnS_2 in, respectively, the precursor and absorber. It could be concluded that SnS_2 phases are detrimental to device efficiency and that SnS_2 XRD peak intensity follows an inverse proportionality with device efficiency.

The third part explores reflectometry as a method to monitor a growing film during thermal evaporation in a physical vapor deposition (PVD) system. A set of six CZTS absorbers is examined by ex situ Raman spectroscopy and reflectometry to study the influence of secondary phases CuS and ZnS on reflection spectra. Composition strongly influences reflection spectra and CuS leaves a characteristic

dip in the reflection spectrum at about 600 nm. An integration method was used to analyze this phenomenon quantitatively. Subsequently, a reflectometry setup is designed, developed and integrated in the PVD system. Four different CZTS co-evaporated and multi-layered films are deposited. Structural, morphological and vibrational properties are investigated. The reflection spectra are monitored during deposition and time-dependent reflection spectra are analyzed for characteristic aspects related to properties such as thickness, band gap and phase formation. CuS could not be detected in the films by the integration method due to the superposition of the CuS dip with developing interference fringes during film growth. However, in multilayered CTS/ZnS film it is found that the onset of ZnS deposition can be detected by increased reflection intensity due to reduced surface roughness. Additionally, the shifting onset of the interference fringes to lower photon energies can be used as a characteristic fingerprint during the deposition process.

In conclusion, this work showed that Raman spectroscopy, XRD and reflectometry could be successfully implemented for in situ process control and monitoring of high temperature annealing and vacuum deposition of Cu-Sn-Zn-S based precursors and absorbers. The application of these in situ techniques can lead to the optimization of thin film material properties and solar cells. As such, this study has paved the way for further improvement of Cu-Sn-Zn-S based precursors and thin film absorbers.

Zusammenfassung

Innerhalb der letzten Jahre hat sich Kesterit Cu_2ZnSnS_4 (CZTS) aufgrund seiner ungiftigen Bestandteile und deren hoher Verfügbarkeit zu einer interessanten Alternative zu Kupfer Indium Gallium (di-)Selenid (CIGS) entwickelt. Zur Herstellung von Kesterit Dünnschichten wird eine Vielzahl von Methoden verwendet wie Ko-Verdampfung, Sputtern, Elektrodeposition, Spray Pyrolyse und andere. Die meisten davon beinhalten einen Temper-Schritt um die Durchmischung und Interdiffusion der Elemente zu stimulieren. Obwohl der Wirkungsgrad der Kersterit Solarzellen von verschiedenen Forschungsgruppen erhöht wurde, ist der Rekordwert von IBM von 12.6 % noch nicht gebrochen worden. Daher werden experimentelle und theoretische Studien benötigt, die den Einfluss von Fremdphasen und schädlichen Defekten auf die elektronischen Eigenschaften der CZTS Solarzellen vorhersagen.

Die vorliegende Arbeit untersucht zerstörungsfreie Methoden für die in situ Prozesskontrolle und -überwachung. Dabei ist das Ziel, entscheidende Prozessschritte wie das Vortempern der Metall-Vorläufer sowie das Hochtemperatur-Tempern und die Vakuum-Abscheidung von Cu-Sn-Zn-S basierten Schichten zu optimieren. Die Untersuchung besteht aus drei Teilen, in denen Raman-Spektroskopie, Röntgendiffraktion (XRD) und Reflektometrie benutzt werden um dieses Ziel zu erreichen.

Im ersten Teil wird die Ramanspektroskopie als in situ Methode zur Überwachung des Hochtemperatur-Temperns von Dünnschichten betrachtet. Es wird untersucht, ob das Entstehen von CZTS beim Tempern von gestapelten Mo/CTS/ZnS Dünnschichten beobachtet werden kann. CuS, SnS, ZnS und CTS (Cu-Sn-S) Schichten werden durch physikalische Gasabscheidung hergestellt. Die Intensität der Raman Streuung wurde vergleichen um zu untersuchen, ob die spezifischen Vibrations-Moden bei Raumtemperatur voneinander unterschieden werden können. Dann werden die CTS Schichten zwischen 50 °C und 550 °C getempert um zu untersuchen, ob die CTS Vibrations-Moden bei höheren Temperaturen identifiziert werden können und um festzustellen, welche Übergänge innerhalb der Schicht auftreten. Außerdem wurde eine CZTS Referenzschicht zwischen 50 °C und 550 °C für Referenzzwecke getempert worden. Die Temperaturabhängigkeit der CZTS Haupt-Moden werden betrachtet, um zu untersuche, ob sie für die in situ Temperaturüberwachung verwendet werden können. Abschließend wurde eine ZnS Schicht auf einem nicht getemperten CTS Film abgeschieden, um eine gestapelte Mo/CTS/ZnS Schicht zu erhalten. Diese Schicht wird verwendet, um die Umwandlung von CTS/ZnS zu CZTS bei erhöhten Temperaturen zu untersuchen. Es wurde festgestellt, dass Raman Spektroskopie erfolgreich verwendet werden kann, um die Bildung von CZTS zu überwachen, indem die Haupt-Vibrations-Moden während des Temperns identifiziert werden. Die Intensität der CTS

Moden verringert sich bei höheren Temperaturen. Bei 450 °C kann die CZTS Hauptmode bei 338 cm^{-1} klar identifiziert werden.

Der zweite Teil konzentriert sich ebenfalls auf das Hochtemperatur-Tempern. In diesem Teil liegt der Fokus allerdings auf dem Tempern der Metal-Vorläufer-Schichten. Es wird erforscht, ob bestimmte Legierungen die Entstehung von Fremdphasen während der Entstehung der CZTS Absorberschichten begünstigen oder hemmen und welchen Einfluss dies auf die Leistung der Solarzelle hat. In situ XRD wird verwendet, um die Prozesse des Vortemperns zu überwachen. Kupfer arme Metall-Vorläufer-Schichten werden durch Sputtern aufgetragen. Die Vorläufer werden bei 150 °C, 200 °C, 300 °C und 450 °C in einem Drei-Zonen-Röhren-Ofen getempert. Die Auswirkungen auf die strukturellen Eigenschaften werden mit XRD analysiert, um den Entstehungsmechanismus der Legierungen zu untersuchen. Die Vorläuferschichten werden dann in einem Drei-Zonen-Röhren-Ofen sulfurisiert. Die strukturellen Eigenschaften des Absorbers werden analysiert und mit der Struktur der Vorläufer korreliert. Es wurde festgestellt, dass die Entstehung von SnS_2 im Absorber proportional zum verbleibenden Sn im vorgetemperten Vorläufer ist. Außerdem zeigen Bilder des Rasterelektronenmikroskops, dass die Temperatur des Vortemperns das Kornwachstum und das Abschieden von Sn-S und Zn-S an der Oberfläche beeinflusst. Bei 450 °C vorgetemperte Absorber weisen keine dieser Phasen an der Oberfläche auf. Solarzellen

werden aus diesen Absorber-Schichten hergestellt und die besten Zellen entstanden aus den bei 450 °C vorgetemperten Absorbern. Bei diesen traten Sn und SnS_2 weder im Vorläufer noch im Absorber auf. Es konnte geschlussfolgert werden, dass SnS_2 Phasen schädlich für den Wirkungsgrad der Zellen sind und dass die Intensität der SnS_2 XRD Peaks invers proportional zum Wirkungsgrad der Zellen ist.

Der dritte Teil erforscht die Reflektometrie als Methode zur Überwachung des Schichtwachstums während des thermischen Verdampfens in einer Anlage zur physikalischen Gasabscheidung (PVD). Ein Satz aus sechs CZTS Absorbern wird mittels ex situ Raman-Spektroskopie und Reflektometrie vermessen, um den Einfluss der Fremdphasen CuS und ZnS auf die Reflexionsspektren zu untersuchen. Die Zusammensetzung beeinflusst die Reflexionsspektren stark und CuS hinterlässt eine charakteristische Senkung bei 600 nm im Reflexionsspektrum. Eine Integrationsmethode wurde verwendet um dieses Phänomen quantitativ zu analysieren. Anschließend wurde ein Reflektometrieaufbau entworfen, entwickelt und in die PVD-Anlage integriert. Vier verschiedene CZTS koverdampfte und Mehrschicht-Filme wurden abgeschieden. Strukturelle, morphologische und Vibrationseigenschaften werden untersucht. Die Reflexionsspektren werden während des Abscheidens aufgenommen und zeitabhängige Reflexionsspektren werden auf charakteristische Aspekte im Zusammenhang

mit Eigenschaften wie Dicke, Bandlücke und Entstehung von Phasen untersucht. CuS konnte in den Schichten mit der Integrations-Methode wegen der Überlagerung der CuS Senkung mit dem entstehenden Interferenzmuster nicht detektiert werden. Allerdings wurde in gestapelten CTS/ZnS Schichten beobachtet werden, dass der Beginn der ZnS Abscheidung durch eine ansteigende Intensität der Reflektion aufgrund der verringerten Oberflächenrauigkeit detektiert werden kann. Zusätzlich kann die Verschiebung des Startpunkts der Interferenzen zu niedrigeren Photonenenergien als charakteristischer Fingerabdruck während des Abscheidungsprozesses verwendet werden.

Zusammenfassend zeigt diese Arbeit, dass Raman-Spektroskopie, XRD und Reflektrometrie erfolgreich als in situ Prozesskontrolle und -überwachung bei Hochtemperatur-Tempern und Vakuum-Abscheidung von Cu-Sn-Zn-S basierten Vorläufern und Absorbern realisiert werden konnten. Die Anwendung dieser in situ Techniken kann zu einer Optimierung der Eigenschaften von Dünnschicht-Materialien und von Solarzellen führen. Als solche hat diese Untersuchung den Weg für weitere Verbesserung von Cu-Sn-Zn-S basierte Vorläufer und Dünnschicht-Absorber geebnet.

Table of contents

Summary.....viii
Zusammenfassung.....xii

1 | Introduction 20

1.1 World energy outlook..... 20
1.2 Thin film photovoltaics..... 22
1.3 Kesterite 23

1.3.1 Kesterite challenges 24
1.3.2 Preparation methods 25
1.3.3 Process control..... 26

1.4 Structure and aim of the thesis..... 28

2 |Experimental techniques 32

2.1 Thin film deposition and annealing..... 32

2.1.1 Sputtering..... 32
2.1.2 Thermal (co-)evaporation 33
2.1.3 Annealing and sulfurization..... 35

2.2 *In situ* process control and monitoring 36

2.2.1 Raman spectroscopy 37
2.2.2 Reflectometry..... 39
2.2.3 X-ray diffraction..... 44

2.3 Morphology and composition characterization..... 45
2.4 Solar cell characterization 47

3 | Results 50

3.1 Manuscript I – In situ monitoring of Cu_2ZnSnS_4 absorber formation with Raman spectroscopy during $Mo/Cu_2SnS_3/ZnS$ thin-film stack annealing 51

3.1.1 Abstract 53
3.1.2 Introduction 54
3.1.3 Experimental methods 56
3.1.4 Results and discussion 59
3.1.5 Conclusion 72
3.1.6 References 74
3.1.7 Supplementary information 83

3.2 Manuscript II – Pre-annealing of metal stack precursors and its beneficial effect on kesterite absorber properties and device performance 91

3.2.1 Abstract 93
3.2.2 Introduction 93
3.2.3 Experimental methods 96
3.2.4 Results and discussion 98
3.2.5 Conclusion 113
3.2.6 References 115
3.2.7 Supplementary information 122

3.3 Manuscript III – Investigation of reflectometry for *in situ* process monitoring and characterization of co-evaporated and stacked Cu-Zn-Sn-S based thin films 127

3.3.1 Abstract 129
3.3.2 Introduction 130
3.3.3 Experimental methods 132
3.3.4 Results and discussion 134

3.3.5 Conclusion 154
3.3.6 References 156
3.3.7 Supplementary information 163
4 Conclusions and outlook 165
5 References 171
6 List of abbreviations and symbols 179
7 Acknowledgements 182

1 | Introduction

This introduction provides a background to the importance of research in the field of energy science. It shows a current picture of the energy use in the world and its future direction. It addresses the requirement to move towards sustainable energies and how solar energy contributes to that. Finally, the aim of the thesis is described.

1.1 World energy outlook

The increase of the global population has broad implications for life essentials such as water, food and energy [1]. A transition to a sustainable way of living is unavoidable in order to reduce the environmental impact. Burning of fossil fuels contributes to the biggest portion of greenhouse gas emissions due to human activities, as depicted in Figure 1. The consequence of increasing greenhouse gas emissions is global warming and this drives several unwanted environmental changes such as retraction and melting of ice glaciers, droughts and other extreme weather conditions.

To reduce and possibly rewind consequences of fossil fuel use it is important to make a transition to sustainable energy sources such as wind, solar and geothermal energy. The key world energy statistics from 2017 indicate that these

energy sources currently contribute less than 1.5 % of the total energy supply in 2015. Although it has increased from 0.1 % in 1973, there is still a huge potential for renewable energy sources [2].

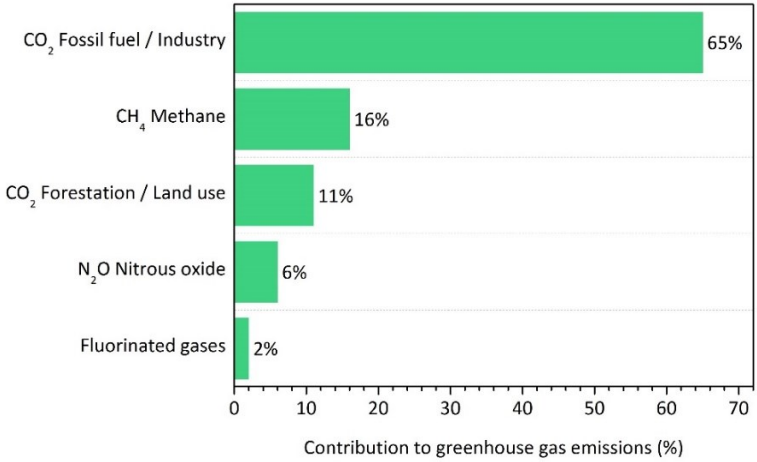

Figure 1 Relative contribution of greenhouse gases emissions from human activities

Figure 2 shows the global electricity generation, which sums up to 24255 TWh in 2015 [3]. Since 1973, electricity from renewables has strongly increased. While renewables contribute 1.5 % to the total energy supply, they account for 7 % to the total *electricity* generation, where 1.02 % is generated by photovoltaic solar energy (PV). In the last decade, electricity production from solar PV increased from 4 TWh to 247 TWh. The biggest suppliers are China and Germany, they provide 18.3 % and 15.7 %, respectively. Followed by Japan, United States and Italy with 14.5, 13.0 and 9.3 %, respectively. In order to reach Paris Agreement

targets, fossil fuel use should be reduced strongly. This implies a huge potential for solar PV and other renewables to shape the energy transition.

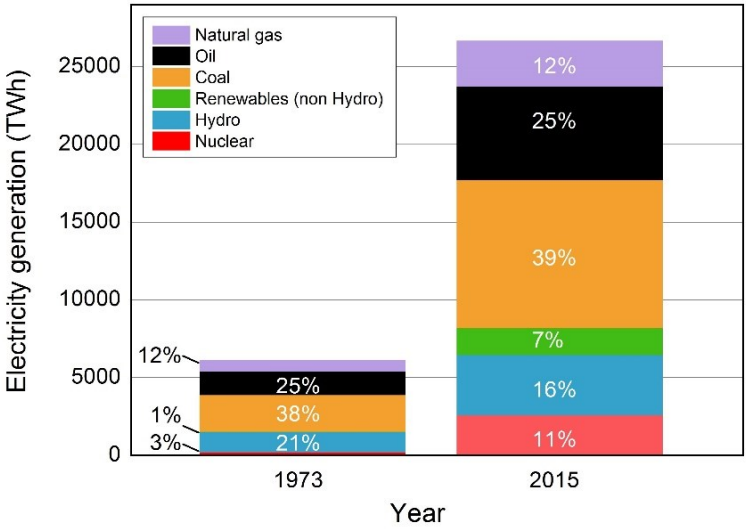

Figure 2 Global electricity generation divided into energy sources for the years 1973 and 2015

1.2 Thin film photovoltaics

The field of photovoltaics has been studied extensively and silicon solar panels have been commercially available for decades. However, thin film solar modules are an attractive alternative because they use less material, are lightweight and are interesting due to their broad applications as opposed to thicker crystalline silicon panels. CIGS (copper, indium, gallium, sulfur/selenium) and CdTe (cadmium telluride) are well developed thin film PV technologies. However, indium is used in CIGS and is also being used in

many electrical devices and other applications as a component in transparent conductive oxides. Indium and gallium are not seen as earth abundant and cadmium and tellurium are considered as toxic elements. To reduce future environmental impact, non-toxic and earth abundant alternatives are preferred. Alternatively to CIGS, kesterite with copper, zinc, tin, sulfur and/or selenium, also known as CZTS/Se, is recently being investigated. It has an ideal direct band gap between 1 and 1.5 eV and a high absorption coefficient of 10^4 cm^{-1}. More recently, groups are starting to investigate the incorporation of other elements, such as germanium or silver, to improve opto-electronic kesterite properties.

1.3 Kesterite

Kesterite or CZTS can be seen as a derivative from CIGS with non-toxic and earth abundant constituents replacing indium and gallium. CZTS/Se is typically used with sulfur and selenium or a ratio of both. This leads to a tunable direct band gap between 1 and 1.5 eV. This is perfectly positioned with respect to the Shockley–Queisser limit, which describes the maximum theoretical efficiency of a single junction solar cell.

Figure 3 shows the record efficiencies of single junction solar cells with respect to their current technological level. Silicon, CIGS and CdTe are being exploited commercially, while CZTS and others are still in the

research & development phase or in the manufacturing phase. There is substantial room for improvement for CZTS since it is currently below 50 % of the maximum attainable efficiency.

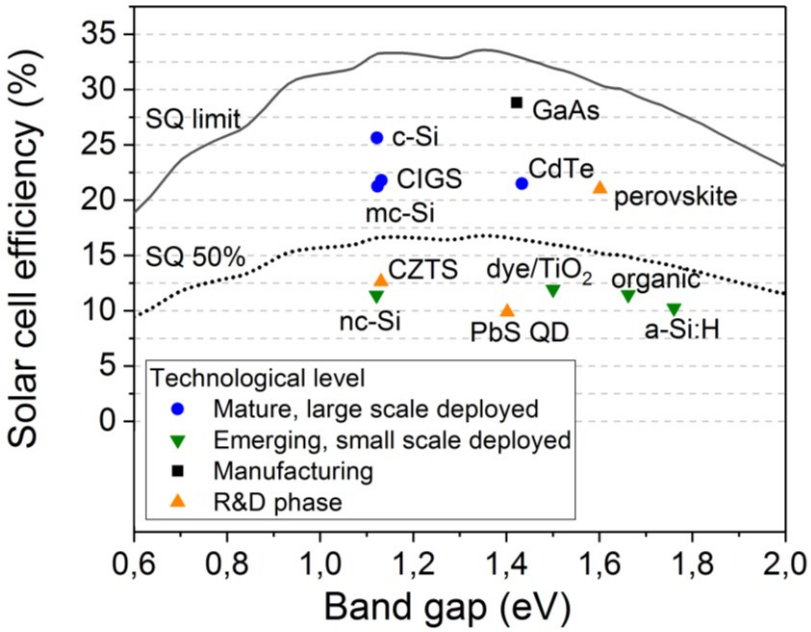

Figure 3 S-Q limit with respect to record efficiencies of solar cell technologies and its current technological level (after [4]*)*

1.3.1 Kesterite challenges

Despite the important benefits of kesterite, it also has challenges. Figure 4 indicates the narrow stoichiometric point of kesterite [5], [6]. Outside this region other, often unwanted phases are present besides CZTS. It was found

that off stoichiometric kesterite delivers better device performance. This easily results in unwanted secondary phases such as Cu-S, Sn-S, Zn-S and Cu-Sn-S compounds and lattice defects within the host kesterite crystal [5], [7]–[11]. Also, decomposition of kesterite and elemental loss might occur during the fabrication process, depending on the process conditions [12], [13]. During high temperature annealing, CZTS might react with the Mo back contact, forming MoS and other unwanted phases in the back contact region [14]. These aspects lead to inhomogeneities within the bulk of the absorber, as well as precipitation of secondary phases on the surface [15]–[17]. Etching methods have been applied to remove Cu-S, Sn-S and Zn-S phases on the surface [9], [16], [18]. Although this can lead to an increase in device efficiency, it may create pathways/voids for CdS during chemical bath deposition of this buffer layer. Also, from an industrial and cost effective perspective, it is preferred to have as little number of processing steps as possible.

1.3.2 Preparation methods

Several deposition techniques can be used to fabricate kesterite thin films. Vacuum deposition techniques such as sputtering and co-evaporation, as well as non vacuum techniques, such as solution based, spray pyrolysis and electrodeposition [9], [10], [15], [19]–[24]. Precursor and absorber deposition may consist of one or multiple steps. In

most cases, deposition is followed by an annealing process taking place in a tube furnace that can be operated under vacuum or inert atmosphere. This annealing step is included to stimulate intermixing of the elements and accelerate grain growth.

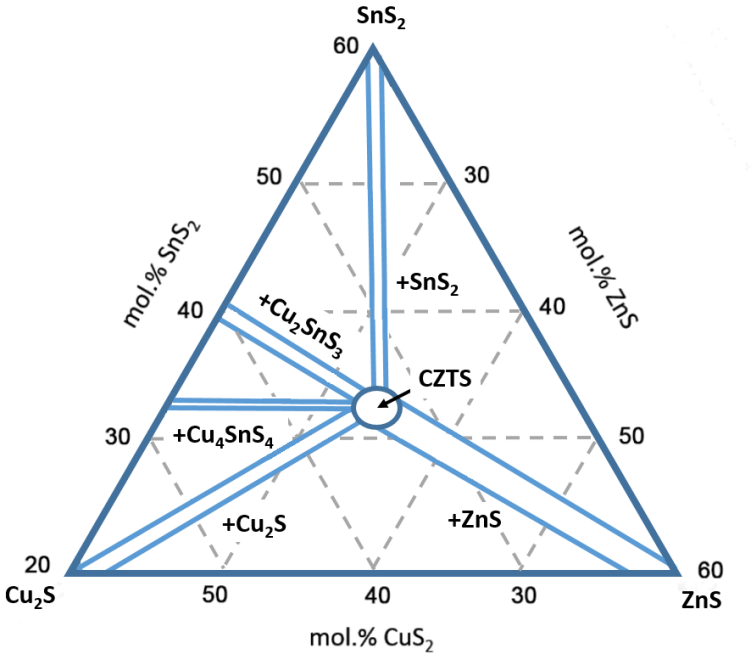

Figure 4 Ternary phase diagram at 400 °C of the Cu_2S-SnS_2-ZnS system with isothermal lines, adjusted from [5], [6]*.Outside the narrow Cu_2ZnSnS_4 (CZTS) region additional unwanted phases are present.*

1.3.3 Process control

Process parameters such as time, pressure and temperature determine thin film growth. The optimum can possibly be determined by trial and error for each system. However, this

can be a time consuming approach and might obstruct reproducibility. It would be more sustainable to develop methods that can be used for in situ process monitoring. These methods should be non-destructive in order to prevent interference with the growth process itself.

Common methods for in situ process control and monitoring are optical techniques such as Raman spectroscopy and reflectometry. Their common use is due to their non-destructive character [25]–[29]. In previous studies, it was shown that Raman spectroscopy can be used ex situ for detection of secondary phases and detection of Se/(S+Se) and Cu/(In+Ga) ratios in chalcopyrites. It was also used in situ for the assessment of crystal quality in CIGSe layers by analysis of the shape and (relative) position of specific vibrational modes. It was also shown that Raman spectroscopy is a valuable technique for the detection of CZTS and Cu-,Zn-,Sn-S based secondary phases [15], [30], [31].

X-ray diffraction can be used to obtain structural properties of thin films during deposition. Small scale table top setup and large scale synchrotron based setups are used. Identification of phases and phase transitions can be observed in CIGS and CZTSe [32], [33]. ZnSe can be distinguished from CZTSe at elevated temperatures [34]. Though in situ investigations on CIGS-based films have been reported more frequently, in situ XRD studies on CZTS/Se films are scarce.

1.4 Structure and aim of the thesis

The motivation for working on Cu-Zn-Sn-S based thin film and the necessity for process control has been illustrated in sections 1.1–1.3 of this chapter. This section will further elaborate on the aim of the thesis. The following chapter 2 will elaborate on the experimental techniques and its theoretical background. In chapter 3, the results of the three publications will be presented, followed by the conclusions and outlook in chapter 4.

The aim of this thesis is to investigate Raman spectroscopy, reflectometry and X-ray diffraction as non-destructive techniques for process control and monitoring. With the purpose of process optimization such that it can lead to thin films and devices with desired properties. Typical processing steps for Cu-Zn-Sn-S based thin films are depicted in Figure 5. The focus of this thesis lies on two main processing steps of Cu-Zn-Sn-S based absorber and precursor films: high temperature annealing and vacuum deposition.

The investigation is threefold. In the first part it is investigated whether Raman spectroscopy can be used during high temperature annealing of CTZS based films. For this purpose, in situ monitoring of Mo/CTS, Mo/CZTS and Mo/CTS/ZnS films during annealing between 50 and 550 °C is investigated. The peak position and intensity of their specific vibrational modes are analysed. CTS and CZTS are examined to serve as a reference.

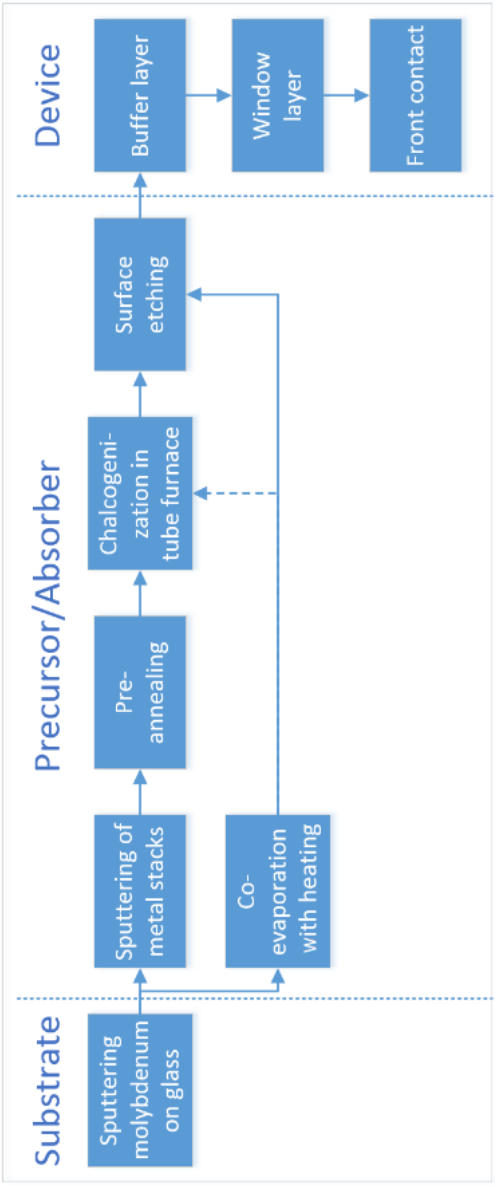

Figure 5 Typical process steps in the preparation of Cu-Zn-Sn-S based thin films and solar devices

Furthermore, it is explored whether vibrational modes of CZTS can serve as a means for temperature control. It is also studied whether formation of CZTS can be monitored during annealing of a CTS/ZnS multi-layer film.

Secondly, X-ray diffraction is explored as a method to study phase transitions in metallic precursor stacks to explore the influence of alloy formation in the precursor on phases in the subsequent absorber. Also, influence of absorber properties on device properties is investigated and correlated with phase observations in the precursor and absorber. Structural, compositional, morphological and vibrational properties are characterized and correlated to device parameters. XRD is used to investigate whether pre-annealing of precursor stacks can be monitored in situ.

Furthermore, reflectometry is studied for in situ monitoring of vacuum co-evaporation of Cu-Zn-Sn-S based films. An optical setup is designed and implemented to operate in conjunction with a PVD chamber to monitor specular reflection during the deposition of co-evaporated and stacked thin films. Time-dependent reflection spectra are analysed for the potential to identify unwanted phases, such as CuS and ZnS. With the aim to obtain thin films with desired properties such as thickness, phase composition and band gap. Structural, compositional, morphological and vibrational properties are studied with ex situ characterization methods to provide in depth information of deposited thin films. The thesis is submitted in cumulative form and it is based on three publications:

1. In Situ Monitoring of Cu_2ZnSnS_4 Absorber Formation With Raman Spectroscopy During Mo/Cu_2SnS_3/ZnS Thin-Film Stack Annealing

Stephan van Duren, Y. Ren, J. Scragg, J. Just and T. Unold
IEEE Journal of Photovoltaics, vol. 7, no. 3, pp. 906-912, May 2017
DOI: 10.1109/JPHOTOV.2017.2686015

2. Pre-annealing of metal stack precursors and its beneficial effect on kesterite absorber properties and device performance

Stephan van Duren, Diouldé Sylla, Andrew Fairbrother, Yudania Sánchez, Simón López-Marino, José A. Márquez Prieto, Victor Izquierdo-Roca, Edgardo Saucedo, Thomas Unold
Solar Energy Materials and Solar Cells, Volume 185, October 2018, Pages 226-232, ISSN 0927-0248
DOI: 10.1016/j.solmat.2018.04.022.

3. Investigation of reflectometry for in situ process monitoring and characterization of co-evaporated and stacked Cu-Zn-Sn-S based thin films.

Stephan van Duren, Sergei Levcenco, Steffen Kretzschmar, Justus Just, Thomas Unold
Journal of Alloys and Compounds, Volume 779, March 2019, Pages 870-878
DOI: 10.1016/j.jallcom.2018.11.337

2 |Experimental techniques

In this chapter experimental techniques which were used in the investigation are described. It provides a background to the methods that were used to prepare and characterize the precursor and absorber films. It elaborates on the characterization methods that are used to investigate the structural, morphological, vibrational, optical and electronical properties of the precursor, absorber films and devices.

2.1 Thin film deposition and annealing

2.1.1 Sputtering

Sputtering is a deposition technique where targets are being used to deposit material on a substrate. The targets are being bombarded with ionized particles originating from an atmospheric gas, such as argon/Ar^+. The gas is ionized by the electrons moving from the target to the substrate due to the potential difference. With magnetron sputtering, electrons move along the magnetic field close to the target. The electron density is highest close to the surface of the target, enhancing ionization and subsequent release of atoms from the target. The elements are released from the target and

directed towards the substrate, where they stick to the surface. The deposited film consists of metals or has a chalcogen incorporated, dependent on the atmosphere. In this thesis, argon and H_2S were used as atmospheric gases.

In the in situ Raman study (chapter 3.1) [35], reactive sputtering in a Von Ardenne CS600 was used to deposit the ZnS layer [20]. The system contains 3 different targets, Cu_2S, Sn and Zn. A 4-inch planar circular target was used with Zn (99.99 %). The target was operated in 20 kHz pulsed direct current mode. Standard process pressure was 5 mTorr with Argon and H_2S (99.5 %) to obtain a ZnS layer. To reduce stress on the substrate during deposition, the substrate temperature was approximately 180 °C. The thickness was verified afterwards with a Dektak profilometer.

For the pre-annealing study (chapter 3.2) metal stacks were prepared by a DC-magnetron sputtering Alliance Ac450 system. The metal targets Cu, Zn, Sn were of 99.99 % purity. The Argon flow was set to 30 cm^3/min and a pressure of 1 x 10^{-3} mbar was used. Substrate rotation was used to obtain a uniform deposited layer and no additional substrate heating was used. A schematic image of a typical sputtering setup is depicted in Figure 6A.

2.1.2 Thermal (co-)evaporation

Another method for thin film deposition is thermal evaporation. With this technique film growth is facilitated by evaporation of elemental metals in a gaseous sulfur

atmosphere. This method was used for film deposition for the studies in chapter 3.1 and 3.3. Individual solid metals of high purity are positioned in separate Knudsen effusion cells. The cells can be heated up to 1500 °C, facilitating the evaporation of copper, zinc and tin towards the substrate. A sulfur cracker is used to provide a sulfur atmosphere in the vacuum chamber.

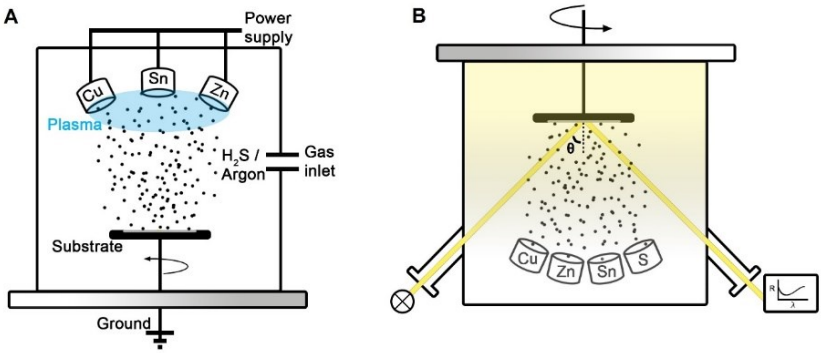

Figure 6 Schematic representation of physical vapour deposition systems. A) Sputtering and B) Co-evaporation

The pressure in the chamber during deposition is approximately 1 x 10^{-5} mbar. The elemental clouds overlap to facilitate uniform deposition of the elements. Substrate rotation and substrate heating were used to facilitate intermixing and deposition of homogeneous films. In order to dissipate heat from the chamber an inner cooling shell with liquid nitrogen is used. A schematic representation of the evaporation system is depicted in Figure 6B.

2.1.3 Annealing and sulfurization

Thermal treatment, or annealing, is used during the preparation of kesterite based thin films at different steps in the process, as shown in Figure 5. It is used to stimulate intermixing and elemental diffusion. Annealing can be performed under inert atmosphere to avoid contamination, or in a sulfur atmosphere in order to obtain sulfur containing compounds. Annealing and sulfurization are typically done in a tube furnace, as depicted in Figure 7A (chapter 3.2). Annealing setups used in conjunction with Raman spectroscopy or X-ray diffraction are much smaller and have a transparent window to perform in situ characterization, as shown in Figure 7B (chapter 3.1, 3.2).

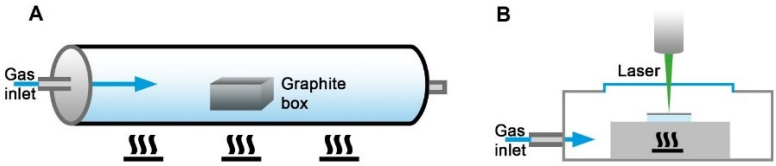

Figure 7 Schematic depiction of annealing systems. A) three zone tube furnace and B) heating stage used for in situ Raman

In the in situ Raman study (chapter 3.1), deposition of the precursor Zn-S, Sn-S, CTS and CuS films was done by co-evaporation at specific temperatures to obtain reference thin films. Deposition of Zn-S on top of CTS was done with sputtering in a H_2S atmosphere. During the in situ Raman study (chapter 3.1) a Linkam heating stage (THMS600) filled with nitrogen was used to anneal the films and to study

phase transitions, see Figure 7B. For the pre-annealing study (chapter 3.2) different methods were used. The metal precursors were prepared by sputtering. The precursors were annealed in a three zone tube furnace at 1 bar Argon in order to obtain mixtures of bronzes and brasses. The samples were placed in quartz crucibles.

The in situ part of this study was performed in a Bruker D8 diffractometer in conjunction with a heating stage, also operated under Argon atmosphere to mimic the treatment in a tube furnace. The absorbers were prepared in a 3-zone tube furnace by placing the thin films in a graphite box (see Figure 7A). The box serves as a confined heat conductive system to reduce elemental losses during sulfurization. Different tubes were used for precursor annealing and sulfurization to avoid cross-contamination.

In the reflectometry study (chapter 3.3), absorbers were prepared by coevaporation and annealed at 550 °C to obtain CZTS films. The in situ monitored films were prepared by coevaporation at around 200 °C, in order to prevent stimulated elemental mixing and monitor deposition of the materials as it is.

2.2 In situ process control and monitoring

The methods that were used for the in situ monitoring studies are Raman spectroscopy, XRD and reflectometry. The following sections will elaborate on each technique and its theoretical background.

2.2.1 Raman spectroscopy

Raman scattering can be detected with Raman spectroscopy. It originates from the inelastic scattering between photons and phonons. The scattering event can lead to a small loss (Stokes) or gain (anti-Stokes) in energy by the photons. As opposed to elastic Rayleigh scattering, where the incoming light has the same energy as the outgoing light. Raman scattering is inefficient and only occurs one in every million scattering events. Therefore, the intensity is much lower than Rayleigh scattering and sensitive detectors are required. The phonon-photon interaction holds material specific information and the measured intensity as a function of the energy is related to specific vibrational modes of the crystal lattice. For the excitation above the band gap of the material the probing depth is dependent on the excitation wavelength and absorption coefficient of the material. In combination with the rather low scattering intensity the method is mainly surface sensitive. Rayleigh and Raman scattering events with respect to energy transitions are depicted in Figure 8.
Figure 9 shows a typical Raman setup in the back scattering geometry with its relevant components. Both Rayleigh and Raman scattering are present in the reflected light when the material is Raman active. In order to detect the Raman signal a notch filter is used to remove the Rayleigh light.

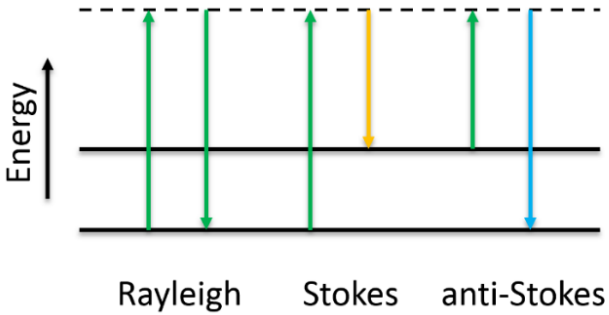

Figure 8 Energy transitions of Rayleigh and Raman scattering. With Rayleigh (elastic) scattering the photon in/out energy is conserved. While with Raman, energy is gained (anti-Stokes) or lost (Stokes), with respect to the incoming photon, during the light-matter interaction as indicated by the changing arrow colors.

The light is diffracted by a grating of the spectrometer in order to obtain a highly dispersed light spectrum. A charge-coupled device (CCD) is then used to convert the dispersed light into an electrical signal and to be able to distinguish light originated from different vibrational modes. For Cu-Zn-Sn-S based thin films Raman spectroscopy has proven to be a technique that can be used to determine secondary phases in the thin film [15], [30], [35]. Vibrational modes of Cu-S, Sn-S and CZTS can be distinguished from each other. Different Cu-Sn-S (CTS) modes are spread across the Raman spectrum and appear in the same region where the modes of the CZTS kesterite phase are present [35]. The intensity of the Zn-S is generally lower than aforementioned phases unless an excitation wavelength (325 nm) is used that coincides with the ZnS bandgap and causes resonant enhancement [36]. A quantitative estimation of the grain size in ZnS nanoparticles

and films can be determined by analysis of the relative peak intensity of higher orders of the main ZnS vibrational mode [36].

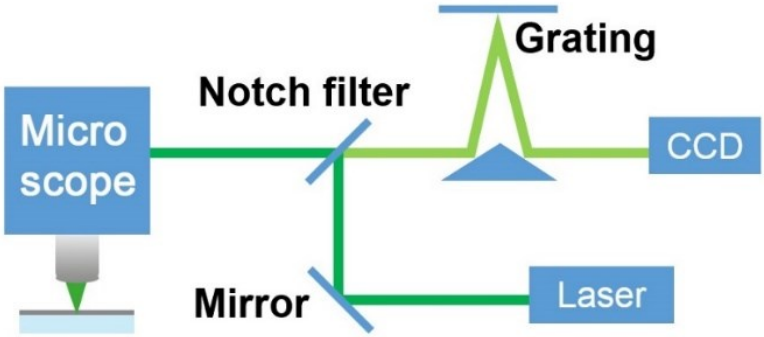

Figure 9 Schematic representation of a Raman microscope setup with main components

During the in situ Raman experiment (chapter 3.1) it is investigated whether phases and phase transitions can be identified at elevated temperatures (50–550 °C). Furthermore, in all studies (chapter 3) Raman spectroscopy is used as a method to verify surface presence of CZTS and related binary and ternary phases as mentioned before.

2.2.2 Reflectometry

Reflectometry is another method where light-matter interaction is used to obtain information about thin film properties. Reflection spectra can be used to extract a variety of thin film properties, such as point-of-formation of

phases, band gap and thickness [25]–[27], [32]. In multi-layer films, presence of interference fringes and its onset are being used for the estimation of thickness and bandgap.

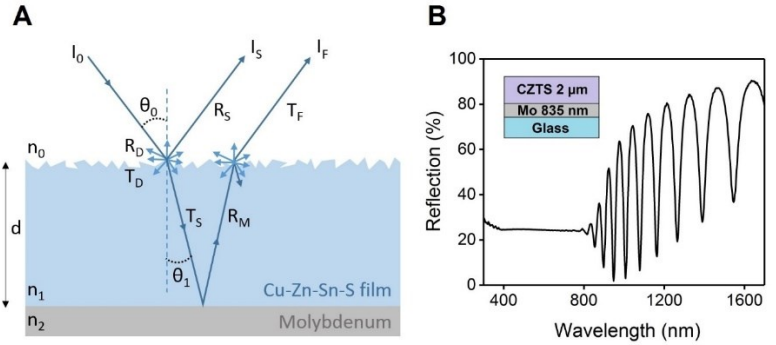

Figure 10 (A) Schematic representation of reflection and transmission in thin films and (B) typical reflection spectrum of a CZTS/Mo/glass film as produced with thermal coevaporation

Figure 10A shows a simplified schematic representation of a thin film where reflection and transmission processes are shown. Light is reflected, transmitted and absorbed by the films. The surface roughness will determine the extend to which light is scattered and determines intensity of direct (specular) and diffuse reflection.

The complex refractive index $n_c = n - ik$, with extinction coefficient *k,* of a material influence how light travels through a medium. The light that eventually leaves the material is the result of reflection, transmission and absorption processes. A typical CZTS reflection spectrum is depicted in Figure 10B.

Light reflected at normal incidence does not change its polarization and its magnitude depends only on the

refractive index of the materials. At oblique incidence, light reflection is different for s- and p-polarized components. The total light intensity for the situation in Figure 10A, where the interference between I_S and I_F beams are considered, can be described by Fresnel equations combined with the scalar scattering theory [32], such that

$$I_{tot} = I_S + I_F + 2\sqrt{I_S I_F}\cos\left[\frac{4\pi d n_1}{\lambda\cos\theta_1}\right] + \Delta\delta \quad (1)$$

with phase shift δ (0 or π), thickness d, roughness σ and specular reflection R_S

$$I_S = R_S = R_{tot}\, e^{-\left[\frac{2\pi\sigma 2 n_0 \cos\theta_0}{\lambda}\right]^2} \quad (2)$$

with

$$R_{tot} = \frac{1}{2}\left[\left[\frac{n_0\cos(\theta_0) - n_1\cos(\theta_1)}{n_0\cos(\theta_0) + n_1\cos(\theta_1)}\right]^2 + \left[\frac{n_0\cos(\theta_1) - n_1\cos(\theta_0)}{n_0\cos(\theta_1) + n_1\cos(\theta_0)}\right]^2\right] \quad (3)$$

and light with intensity passed through the absorber twice

$$I_F = T_S T_F e^{-\frac{\alpha 2 d}{\cos(\theta_1)}} R_M \quad (4)$$

where reflection from molybdenum R_M= R_{tot} with subscripts 0 → 1 and 1 → 2 (e.g. n_1 → n_2) and

$$T_s = T_F = (1 - R_{tot}) e^{-\left[\frac{2\pi\sigma[n_0\cos\theta_0 - n_1\cos\theta_1]}{\lambda}\right]^2} \quad (5)$$

since it is the same interface.

This method can be used for multilayer films by including R and T coefficients for every layer. However, when the amount of layers is increased, calculation of Fresnel coefficients becomes tedious and the transfer matrix method can be applied to obtain the total reflection and transmission. This is a generalized formalism and is integrated in the Optisim program [37]–[39].

With respect to absorption, the absorption coefficient is defined as

$$\alpha = \frac{4\pi k}{\lambda} \tag{6}$$

For the allowed direct transitions at band gap E_g it can be written as

$$\alpha \propto \sqrt{(h\upsilon - E_g)} \tag{7}$$

with $h\upsilon$ and λ the photon energy and wavelength, respectively [40].

It can be concluded that reflection spectra hold information about properties such as thickness, band gap and roughness. Also, because n_c is material specific, reflection spectra can possibly be used as material specific fingerprints during deposition of thin films. However, it should be taken into account that the band gap is temperature dependent and reduces at elevated temperatures. This is caused by increased interatomic spacing due to thermal expansion and electron-phonon interaction, such that

$$E_g(T) \approx E_g(0) - \frac{zT^2}{T+\beta} \tag{8}$$

with temperature T and z, β as fitting parameters [40].

A characteristic aspect of the reflection spectrum is the onset of interference fringes. This depends on the thickness and band gap of the absorber. In the in situ reflectometry study (chapter 3.3), a setup was developed such that it could monitor reflection during deposition in the PVD system. A schematic representation is shown in Figure 11. Optical

cages were mounted on two viewports at opposite sides of the PVD chamber. On one side a halogen lamp (type SLS201L) was fiber coupled to a silver coated collimator with a 90° off-axis parabolic mirror to prevent chromatic aberration. The collimator was mounted on the optical caging system, aiming at the center of the substrate. An iris diaphragm was used to adjust light intensity. On the opposite side of the chamber a similar construction was used to couple the reflected light with the spectrometers connected to a computer.

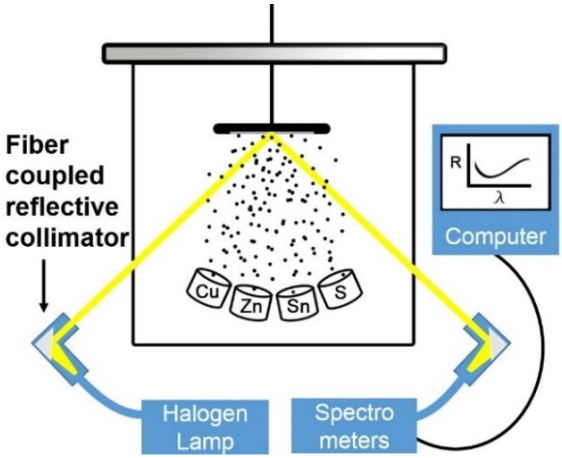

Figure 11 Schematic representation of the PVD system with in situ reflection setup

For the ex situ measurements a commercial Perkin Elmer spectrophotometer was used to measure reflection spectra and to be able to distinguish contributions from specular and diffuse part of the reflection.

2.2.3 X-ray diffraction

With X-ray diffraction it is possible to obtain information on crystal structures in the thin film. The position of atoms in a crystal lattice follows a certain pattern dependent on the material. At different orientations, parallel planes can be drawn through the lattice. Reflection of X-rays from these planes causes constructive interference when Bragg's Law, $2d \sin\theta = n\lambda$ is fulfilled, as shown in Figure 12. This depends on the incident angle and the distance between two lattice planes. With GIXRD only the detector moves and the beam hits the sample at a fixed shallow angle. This provides the possibility to increase the reflection intensity from highly oriented films. A shallow incident angle also increases the path length through the film. Which reduces interaction with the substrate, that otherwise might cause difficulty to distinguish thin film reflections [41]. This typically occurs during a symmetric θ-2θ Bragg-Brentano measurement where the metal back contact layer consists of molybdenum.

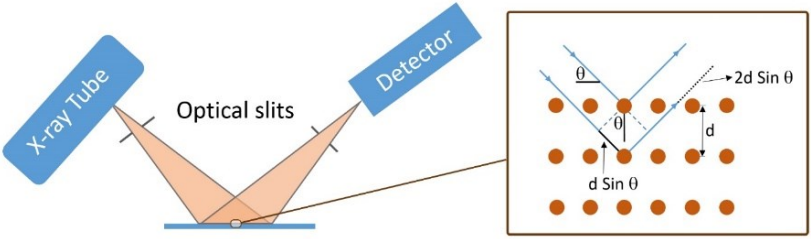

Figure 12 Schematic image of an X-ray diffraction measurement setup with incident X-ray beam illustrating conditions for constructive interference as defined by Bragg's law

In θ-2θ, only reflections parallel to the substrate surface contribute to the diffractogram. Therefore, GIXRD is well-suited for ordered thin films. Upon heating of the sample thermal expansion alters interatomic distances and subsequently lead to a shift in the peak position of reflections observed in the XRD pattern. This has to be taken into account during the annealing experiment (chapter 3.2), such that XRD reflections are properly assigned to the correct phase.

2.3 Morphology and composition characterization

In order to obtain more information about the morphological and compositional properties of the thin films Scanning Electron Microscopy/Energy-dispersive X-ray spectroscopy (SEM/EDX) and X-ray Fluorescence (XRF, Figure 13) were carried out respectively. X-ray fluorescence can be used to determine thin film composition. X-rays are used to excite the material and, similarly to SEM-EDX, characteristic X-rays are being detected.

The electron is pushed out of its shell and leaves a vacancy. The atom becomes unstable and the vacancies are filled by an electron from a higher orbital, see Figure 13. The difference in energy is emitted as a characteristic X-ray, such as Kα and Kβ. Prior calibration with Rutherford backscattering facilitates the XRF counts to be correlated with thin metal films of known composition.

With SEM the electron beam is focused towards the sample with magnetic lenses. Another set of magnets facilitate the

scanning across the surface. The excitation voltage of the primary electrons, typically 5 or 7 keV, determine the penetration depth, and thus the information depth of the sample. The secondary electrons are registered by the detector and the amount of electrons detected at each position will be used to draw a contrasted image of the sample.

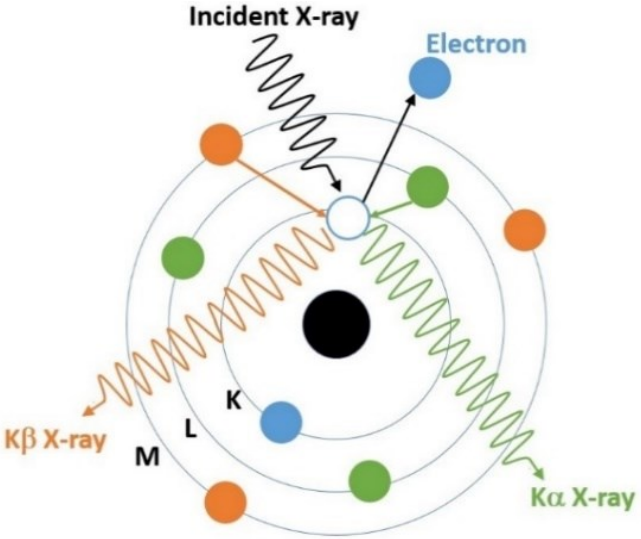

Figure 13 Schematic image of the fundamental process behind X-ray fluorescence, resulting in, for example, Kα and Kβ emissions.

A cross-section image of the sample can provide information such as thickness, morphology and voids in the thin film. For example, ZnS acts as an insulator and charging effects causes ZnS regions to appear brighter in SEM imaging. SEM-EDX can be used to estimate the composition of the film by detection of characteristic X-rays. In that case, the acceleration voltage is set according to the elements that are analysed.

Characteristic X-rays cause current pulses inside the detector, these are converted into a digital signal and conversely assigned to energy slots [41].

2.4 Solar cell characterization

The investigation of in situ process control and monitoring is meant for optimization of CZTS thin films that can serve as the absorber section of a solar cell device.
In the pre-annealing study (chapter 3.2) solar cell properties are correlated to material properties. A solar cell can be described as an electrical device that operates in a similar manner as a diode. The performance of a solar cell can be analyzed by measuring the current-voltage characteristics, as depicted in Figure 14. When the solar cell is illuminated a photocurrent is generated.

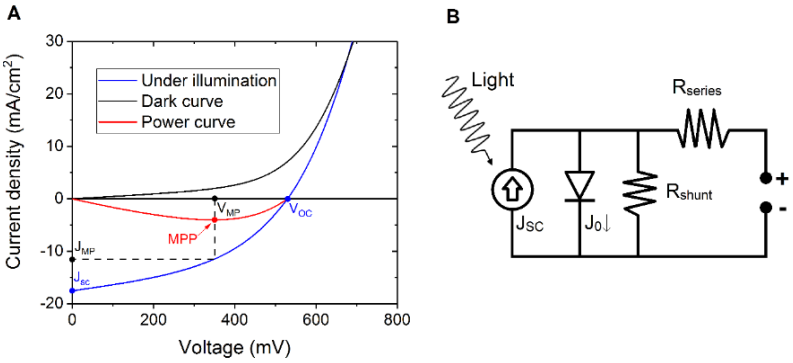

Figure 14 (A) Depiction of a typical IV curve measurement (CZTS, chapter 3.2) performed on a solar cell. (B) Representation of a solar cell as an electrical circuit.

The current at 0 volt is the short circuit current, J_{SC}. The total current-voltage dependency can be described by including

the saturation current, series resistance(R_{series}) and shunt resistance (R_{shunt}) , such that

$$J = J_0 \left(exp \left[\frac{q(V - JR_{series})}{nk_BT} \right] - 1 \right) + \frac{V - JR_{series}}{R_{shunt}} + J_{SC} \quad (9)$$

with elementary charge q, ideality factor n, Boltzmann constant k_B and temperature T. At zero volt $J = J_{SC}$.

The open circuit voltage is found at *J* = 0 and under assumption of high R_{shunt} it leads to

$$V_{OC} = \frac{nk_BT}{q} \ln(1 - \frac{J_{SC}}{J_0}) \quad (10)$$

The voltage at zero current is defined as the open-circuit voltage. Defects, bad interfaces, voids, secondary phases and other non-idealities cause resistances inside the solar cell as indicated by R_{series} and R_{shunt}.

The fill-factor describes the power ratio between the maximum and theoretical limit of the solar cell. In essence, it is a quality indicator of the solar cell and is defined as

$$FF = \frac{V_{MP}J_{MP}}{V_{OC}J_{SC}} \quad (11)$$

The power curve is found by *P=IV,* where the maximum power point (MPP) is found where the derivative of this curve equals 0. The efficiency of the solar cell is then defined as the ratio between the power in (sun AM1.5 = 1000 W/m^2) and power out

$$\eta = \frac{V_{MP} J_{MP}}{P_{in}} \tag{12}$$

These important parameters that determine the quality of the solar cell can be obtained by determining the JV-characteristics. This is typically done by applying a voltage range to a solar cell without light (dark) and under illumination of one sun equivalent, typically with a solar simulator. JV-curves are then obtained as depicted in Figure 14A.

3 | Results

In this chapter the results will be discussed. The results are divided into three sections, where each section is presented as a manuscript. The studies are focused on three commonly used techniques, namely, Raman spectroscopy, X-ray diffraction and reflectometry. These methods are investigated for in situ monitoring of two important processing steps; high temperature annealing and thin film vacuum deposition.

Manuscript I presents the results of a study where Raman spectroscopy is investigated for in situ monitoring. It examines whether main vibrational modes of CZTS and CTS can be observed at elevated temperatures between 50 and 550 °C. Also, it explores wether formation of Cu_2ZnSnS_4 (kesterite) can be monitored in situ by annealing a Mo/Cu_2SnS_3/ZnS multilayer thin film.

Manuscript II discusses the influence of pre-annealing of metallic precursors on the presence of Sn and Cu-Sn alloys and investigates whether XRD can be used for in situ monitoring. It further studies the effect of Sn and Cu-Sn alloys, in the precursor, on SnS_2 formation in the absorber and its subsequent influence on device efficiency.

Manuscript III describes the result of a study where a reflectometry setup was designed and integrated in a physical vapour deposition system. Reflectometry is studied

whether it can be used for detection and identification of unwanted phases during deposition of co-evaporated and stacked Cu-Zn-Sn-S based thin films. Furthermore, it is examined whether time-dependent reflection spectra can be used to serve as a fingerprinting method for in situ process monitoring.

3.1 Manuscript I – In situ monitoring of Cu_2ZnSnS_4 absorber formation with Raman spectroscopy during Mo/Cu_2SnS_3/ZnS thin-film stack annealing

The fabrication of Cu_2ZnSnS_4 (CZTS, kesterite) films involves a high temperature annealing step. Raman spectroscopy is a strong technique to identify CZTS and related phases by their specific vibrational modes. In situ Raman spectroscopy during high temperature annealing of CZTS based films has not yet been investigated. The aim of this study is to investigate whether Raman spectroscopy is suitable to identify CZTS and related phases at elevated temperatures, between 50 °C and 550 °C. In particular, formation of CZTS from a multilayer film Mo/Cu_2SnS_3/ZnS is examined during annealing within this temperature range. It is found that formation of Cu_2ZnSnS_4 could be monitored in situ. This study shows that Raman spectroscopy can be used for in situ for process monitoring in order to gain more insight in the point of formation of CZTS during high temperature annealing.

Publication notification

Title: In situ monitoring of Cu_2ZnSnS_4 absorber formation with Raman spectroscopy during Mo/Cu_2SnS_3/ZnS thin-film stack annealing

Keywords*:* Raman scattering, In situ monitoring, Kesterite, Process control

Authors: Stephan van Duren[1], Y. Ren[2], J. Scragg[2], J. Just[1] and T. Unold[1].

[1]Department Structure and Dynamics of Energy Materials, Helmholtz-Zentrum Berlin, Hahn-Meitner-Platz 1, 14109 Berlin, Germany.

[2]Ångström Solar Center, Solid State Electronics, Uppsala University, Box 534, SE-751 21 Uppsala, Sweden.

Journal: IEEE Journal of Photovoltaics, vol. 7, no. 3, pp. 906-912, May 2017.

DOI: 10.1109/JPHOTOV.2017.2686015

My contribution:

Development and design of the in situ experiments. Preparation of the films by co-evaporation. Performing Raman experiments, SEM and XRD. All data analysis and writing of the manuscript.

3.1.1 Abstract

In recent years, $Cu_2ZnSn(S,Se)_4$ (kesterite) has become increasingly popular as a sustainable alternative absorber material. Many processes for kesterite synthesis involve a high temperature annealing step (>450 °C). This study investigates the possibility of Raman spectroscopy as an in situ monitoring technique during high temperature annealing up to 550 °C. Temperature-dependent behaviour of Cu_2SnS_3 (CTS) and Cu_2ZnSnS_4 (CZTS) was studied for reference purposes. The synthesis of Cu_2ZnSnS_4 (CZTS) was performed by annealing a stacked $Mo/Cu_2SnS_3/ZnS$ precursor on a glass substrate. Annealing of the precursor stack resulted in formation kesterite and could be monitored in-situ by its main A-mode at 338 cm^{-1}. At higher temperatures this mode shifts to lower wavenumbers, is broadened and reduced in intensity. This can be attributed to combined effects of thermal expansion and anharmonic phonon coupling. The shift of the peak position is linearly proportional to the temperature. Thus, given proper calibration, fitting the peak position of the 338 cm^{-1} mode during the process yields the sample temperature. Implementation of in situ monitoring with Raman spectroscopy would be a step forward towards desired process control and monitoring during this crucial high temperature annealing step in kesterite synthesis.

3.1.2 Introduction

In recent years there has been tremendous increase of research in the field of kesterite materials, typically indicated by the chemical formula $Cu_2ZnSn(S,Se)_4$ (CZTS). CZTS is considered as a promising absorber material for solar cells, consisting of earth-abundant metals combined with sulfur, selenium or a ratio of both. With an above-bandgap absorption coefficient above 10^4 cm^{-1} and a bandgap between 1 and 1.5 eV, dependent on the Se/S ratio, CZTS has favorable properties with respect to the Schockley-Queisser limit [1]–[3].

Substantial progress has been made by using different approaches to fabricate kesterite thin films in one- [4] or two-step processes. In a two-step process, precursors such as metal stacks [5] and nanoparticles [6] are used and followed by an annealing step in order to obtain kesterite films [7]. Doping with germanium [8] and sequential etching [9] is applied in some cases. The record efficiency was set by IBM in 2013 with its hydrazine process [10]. Apart from device performance, progress in the understanding of the structural and vibrational properties of CZTS has been made by several research groups that used Raman scattering [11]–[14], neutron diffraction and X-ray diffraction/absorption [15], [16].

Even though the single phase region of CZTS is narrow, best performing solar cell devices seem to improve when the composition is slightly copper poor and zinc rich,

where the compositional ratios are approximately 0.76–0.90 for Cu/(Zn+Sn), 1.1–1.3 for Zn/Sn, and 1.8–2.0 for Cu/Sn [17-19].

Unfortunately, off-stoichiometric conditions promote the formation of secondary phases, such as ZnS, which are detrimental for device performance. Annealing steps are commonly used to incorporate sulfur or selenium in the precursor. Additional tin is supplied to compensate for the expected tin loss which occurs during decomposition of kesterite [7], [20]. Furthermore, defect related issues such as vacancies, antisites, interstitials and other complexes such as Cu/Zn antisite disorder have led to crystal impurities and result in bandgap variations that affect the electronic properties of the absorber [15], [21]–[24].

The aforementioned challenges require adequate in situ process monitoring in order to identify and control crucial process steps. Raman spectroscopy can be used for phase identification [11], [14], grain size estimation [25] and defect related analysis [24], [26]–[28]. Not only kesterite compounds but also chalcopyrite compounds have successfully been studied with Raman spectroscopy, in situ and ex situ, as reviewed by Scheer et al. [29].

The measurement technique is relatively straightforward, non-invasive, non-destructive and could be transferred to an industrial environment, depending on the process conditions.

In addition to previous results [30] this study provides an extended analysis of temperature dependent

properties of the vibrational modes of CZTS and Cu_2SnS_3 (CTS) reference films. A comparison of CZTS and CTS with regard to common secondary phases such as ZnS, CuS and Sn_xS_y has been added. In order to distinguish between CZTS and Cu_2SnS_3 (CTS) during annealing of the Mo/CTS/ZnS stack, peaks of vibrational modes suitable for in situ identification, were fitted by a Lorentzian function and correlated with temperature. This was compared with respect to literature [32,33]. Additionally, a Raman shift-temperature relation can facilitate in situ temperature control. Also, false color intensity plots are included to visualize line width and scattering intensity variation during annealing. Furthermore, an analysis before and after annealing of the thin films is presented. Supplementary material is provided to elaborate on the analysis of the CTS reference film.

3.1.3 Experimental methods

Thin film formation

CTS films were co-evaporated on a molybdenum-coated glass substrate. The substrate temperature was held at approximately 200 °C. This was done in a coevaporation system equipped with separate copper and tin effusion cells [4]. Evaporation of copper and tin was performed in sulfur atmosphere at a base pressure of 7.5 x 10^{-6} Torr. This resulted in a CTS thin film with approximate thickness of 1 micrometer.

The Mo/CTS/ZnS stack was prepared by adding a ZnS layer on top of the CTS film. The substrate temperature was held at approximately 180 °C. The ZnS was deposited using a DC pulsed magnetron sputtering system using a Zn target under H_2S flow, as previously described [34]. The resulting ZnS layer was approximately 300 nm thick. The thicknesses were verified by cross-section SEM and a profilometer.

A reference CZTS film was fabricated in order to explore the extent to which CZTS modes can be identified during annealing at high temperatures. The film was fabricated with the standard process at the UU-ASC [31]. The first step was performed by reactively sputtering copper, zinc and tin in a H_2S atmosphere. The substrate temperature was held at approximately 180 °C. A second step was executed by annealing the precursor in a tube furnace. The CZTS precursor obtained from sputtering was placed in a graphite box with additional sulfur and annealed at approximately 560 °C in a static argon background pressure of 265 Torr [23].

Characterization of films

The structural properties of the CTS film were characterized by X-ray diffraction at grazing incidence angle of 0.5° (see supplementary material). This angle was chosen in order to avoid the strong signal from the Molybdenum film. Also, the Raman scattered light originates from a similar depth regime and thus holds information about a similar volume. A Renishaw inVia system was used for the Raman

measurements. A grating with 1800 lines/mm was used and the laser spot was focused using a microscope camera image of the sample surface. Using this image, a laser spot size of approximately 5 µm in diameter was estimated. Excitation was performed with a 532nm diode laser. This excitation wavelength was found to deliver the best signal to noise ratio for the material specific vibrational modes of CTS and CZTS. The system was calibrated with an internal Silicon crystal. A laser power study was performed to prevent thermal effects and damage by the laser. A laser power of approximately 300 µW was found to be suitable, measured with a handheld laser power meter.

In situ annealing

A Linkam heating stage (THMS600) was used to perform in situ Raman measurements at elevated temperatures. The heating stage has a 2 cm diameter window and the approximate distance from the NUV x15 objective to the surface of the film was 5 mm. All in situ experiments were performed under nitrogen atmosphere in order to prevent oxidation. An acquisition time of 100 seconds was used. It was found that Raman spectra at 50 °C are almost indistinguishable from room temperature spectra. Therefore, the spectrum at 50 °C was taken as a reference in order to reduce cooling time in between annealing steps in the case of the reference measurements of CTS and CZTS. After annealing of the Mo/CTS/ZnS stack, surface morphology was analyzed with a GEMINI electron

microscope at 7 kV beam voltage. Compositional information was obtained by an energy dispersive x-ray measurement in the same microscope.

3.1.4 Results and discussion

Comparison of secondary phases

As part of this study, a comparison of the Raman spectra between Sn_xS_y, CuS, ZnS, CTS and kesterite was made as depicted in Fig. 1.

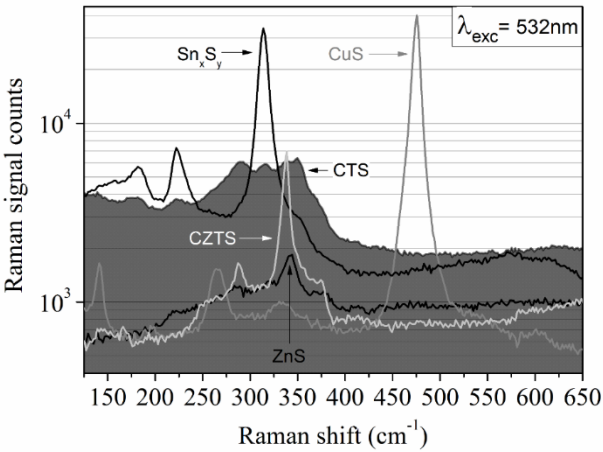

Fig. 1. Reference Raman spectra of different thin films: CuS, Sn_xS_y, CTS, CZTS and ZnS. The spectrum that belongs to the specific film is indicated with an arrow and the name of phase/film. The spectra were acquired with the same setup configuration. The excitation wavelength is 532 nm and laser power is approximately 300 μW. The laser spotsize is approximately 5 micrometer.

All films were prepared as described before. The tin-sulfide film was found to have a mixture of Sn-S phases and is therefore announced as Sn_xS_y. It was found that the

scattering intensity from CuS and Sn_xS_y is much stronger in comparision to CTS, CZTS and ZnS for the specific setup configuration. The absolute counts of the Raman signal are shown in Table I.

Table 1.
Raman shift peak position (left column, in cm^{-1}) and Raman signal absolute counts (right) for each phase as in Fig.1. The peak positions for CTS were obtained from deconvolution as indicated in the supplementary material (Figure S2 topleft graph). The four CTS peaks with highest intensities are shown here.

CuS		*Cu_2SnS_3*		*CZTS*		*Sn_xS_y*		*ZnS*	
cm^{-1}	counts	cm^{-1}	counts	cm^{-1}	counts	cm^{-1}	counts	cm^{-1}	counts
140	*1652*	*291*	*6066*	*288*	*1650*	*180*	*5721*	*342*	*1819*
266	*1515*	*315*	*5916*	*338*	*6964*	*224*	*7302*		
475	*40188*	*338*	*6199*			*314*	*33918*		
		352	*6391*						

The relevant modes of CZTS and CTS are in the same intensity regime. Therefore, if only these phases coexist it should be possible to observe them simultaneously. This section elaborates on the temperature dependent behaviour of Cu_2SnS_3 (CTS). See the supplementary material for the grazing incidence XRD pattern before annealing (Fig. S1). Previous studies performed on CTS have indicated there are multiple phases possible [36-42]. The following can be stated about the XRD pattern of the unannealed CTS film. The cubic Cu_2SnS_3 phase is a high temperature polymorph (>775 °C) and thus unlikely to form [36]. A low intensity contribution at 77° indicates presence of the

tetragonal Cu_2SnS_3 phase. Minor contributions at 16° and 21° distinguish the presence of monoclinic Cu_2SnS_3.

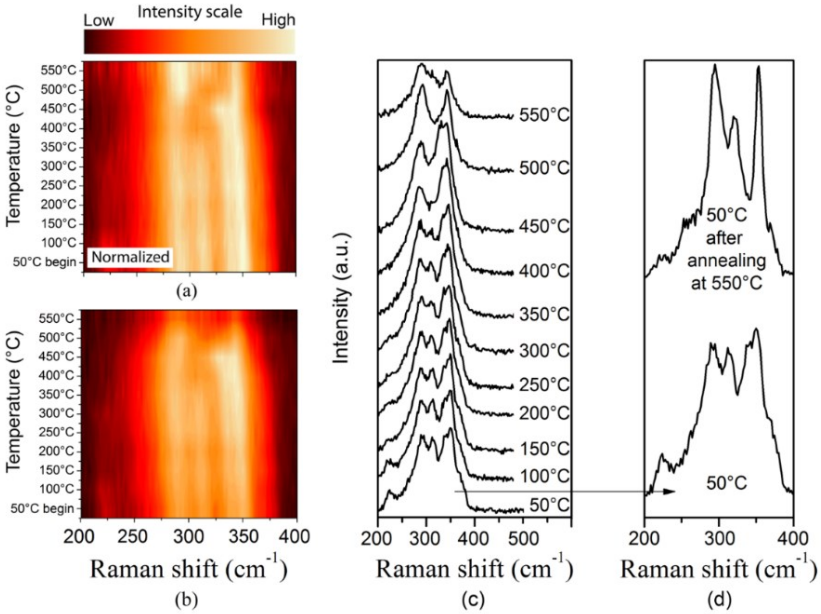

Fig. 2. (a) and (b) Intensity plots of CTS Raman spectra taken during annealing, where (a) is normalized. The bright and dark regions indicate respectively high and low Raman scattering intensity. A broadening can be observed, especially above 300 °C. There appears to be a left-shift of the modes, this can be noticed over the full temperature range. (c) CTS Raman spectra taken at stated annealing temperatures. From low to high temperature annealing, recrystallization of the material occurs. This can be concluded by the reduction of the number of vibrational modes (see SI) and increase of the linewidth of specific modes at 295 cm^{-1} and 353 cm^{-1} after annealing at 550 °C. (d) Comparison of the CTS Raman spectra before and after annealing, obtained at 50 °C. The intensity of specific modes has increased and the FWHM has decreased, indicating that the film has increased crystallinity after annealing.

The peaks at 14/15° and 34° might be related to the $Cu_4Sn_7S_{16}$ phase [38] or the $Cu_2Sn_3S_7$ monoclinic phase.

Contributions at 27° and 52° can be attributted to the Cu_3SnS_4 orthorhombic phase.

No indication was found for presence of the Cu_4SnS_6 and Cu_4SnS_4 phases. It is concluded that the initial film dominantly consists of a mixture of monoclinic and tetragonal Cu_2SnS_3 phases with some additions of other phases.

Fig. 2 shows the temperature dependent Raman spectra of CTS. Fig.2(a) and (b) show two intensity plots based on the spectra presented in the Fig. 2(c). The initial spectrum at 50 °C is broad, with contributions from seven individual Raman modes. This can be concluded from deconvolution of the spectra after each annealing step, as presented in the supplementary section (Fig. S2 and S3).

The CTS Raman spectrum taken at 50 °C resembles Raman spectra of unannealed films presented in other studies; a broad spectrum with several peaks in the 250–400 cm^{-1} range [34,39]. The peaks at 291 cm^{-1} and 352 cm^{-1} are related to the monoclinic Cu_2SnS_3 phase [36,39]. In between these modes there are two other fitted modes at approximately 315 cm^{-1} and 338 cm^{-1}. These modes fluctuate slightly in relative intensity during the course of the annealing process and a contribution from tetragonal Cu_2SnS_3 can be observed [39,42]. The cubic Cu_2SnS_3 phase is less likely because the mode at 303 cm^{-1} is not observed and due to the high temperature requirement this phase is unlikely to be present. Furthermore, a contribution to the modes at 315 cm^{-1} and 338 cm^{-1} may originate from the

Cu_3SnS_4 orthorhombic phase [41,42]. Up to 350 °C there are no significant changes in the spectrum. Above 350 °C, the distance between the modes at 315 cm^{-1} and 338 cm^{-1} becomes smaller in terms of peak position and the peak intensity at 338 cm^{-1} becomes stronger. At 500 °C there is an intensity drop in both modes, indicating a reduction of these phases. At 550 °C a phase transition occurs and both modes are converted into a single mode at 322 cm^{-1}. This is possibly related to $Cu_4Sn_7S_{16}$.

Similar to the XRD pattern presented in this study, a study by Kanai et al. observed a peak at 14–15° and assigned a Raman peak at 327 cm^{-1} to $Cu_4Sn_7S_{16}$ accordingly [38]. Alternatively, the peak at 322 cm^{-1} could be related to the orthorhombic Cu_3SnS_4 phase [41]. It remains unclear which phases attribute to the mode at 260 cm^{-1}. The lower intensity peaks at around 222 cm^{-1} and 371 cm^{-1} are possibly related to the $Cu_2Sn_3S_7$ [36, 39,40].

As described, a transition and enhancement of phases could be monitored with Raman spectroscopy during the annealing proces. Starting off with a mixture of monoclinic and tetragonal Cu_2SnS_3 phases predominantly. The contribution of the monoclinic phase enhances, while the tetragonal phase reduces and is replaced by either Cu_3SnS_4 and $Cu_4Sn_7S_{16}$ or a mixture of both. Fig. 2(d) compares Raman spectra at 50 °C before and after annealing and exhibits reduction of the line width of several vibrational modes (see Fig. S2, qualitatively). This confirms the improvement of crystallinity in monoclinic Cu_2SnS_3 phase.

In situ annealing of CZTS reference

First, temperature-dependent Raman measurements of kesterite are performed to determine suitable vibrational modes for in situ monitoring purposes. Previously, Dimitrievska et al. illustrated in a multi wavelength study on kesterite the identification of 18 out of 27 theoretically predicted vibrational modes. Besides minor contributions of vibrational modes in the below 200 cm^{-1} regime, the main A-modes at approximately 287 cm^{-1} and 338 cm^{-1} are dominant in the Raman spectrum.

Also, it can be observed that the A-mode at 338 cm^{-1} is dominant in all spectra, independent of the wavelength [11]. This mode has the highest scattering intensity and might well be suitable for in situ monitoring.

In order to verify the suitability of the Raman modes at high temperatures, a kesterite thin film was fabricated by the standard process at the UU-ASC [31], which consists of an initial reactive sputtering step in H_2S atmosphere followed by an annealing step in a tube furnace. Then the kesterite film was characterized at elevated temperatures as shown in Fig. 3.

In Fig. 3(a)–(c), when temperature is increased both A-modes at 287 and 338 cm^{-1} are shifted to lower wave numbers, broadened and reduced in intensity. This behaviour was observed before and attributed to combined effects of thermal expansion and anharmonic phonon coupling [32], [33]. At 50 °C, the Raman intensity of the A-mode at 287 cm^{-1} is approximately six times lower than the

A-mode at 338 cm^{-1}. Above 250 °C, the mode at 338 cm^{-1} can be clearly identified as indicated by the intensity plot in Fig. 3.

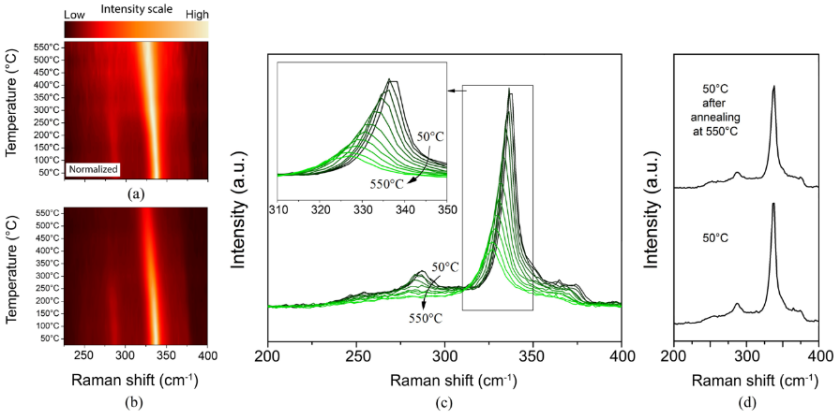

Fig. 3. (a) and (b) are intensity plots of CZTS Raman spectra recorded during annealing, (a) is normalized. The bright and dark regions indicate respectively high and low Raman scattering intensity. From the normalized intensity plot, a broadening can be observed, starting above 200 °C. There is a left-shift of the modes, this can be noticed over the full temperature range. (c) CZTS Raman spectra taken at stated annealing temperatures. From low to high temperature annealing, the A-mode at 287 cm^{-1} disappears above 250 °C while the A-mode at 338 cm^{-1} can be observed in the full temperature range. The arrow indicates the relation between temperature and spectrum (d) A comparison of the CZTS Raman spectra before and after annealing, obtained at 50 °C. There are no significant differences besides a slight overall intensity reduction.

Broadening of the 338 cm^{-1} peak is more obvious from the normalized intensity plot. Interestingly, the 338 cm^{-1} mode can even be observed at 550 °C, well within the temperature range of common practice annealing procedures in the kesterite community. The Raman spectra before and after annealing are almost identical (see Fig. 3(d)).

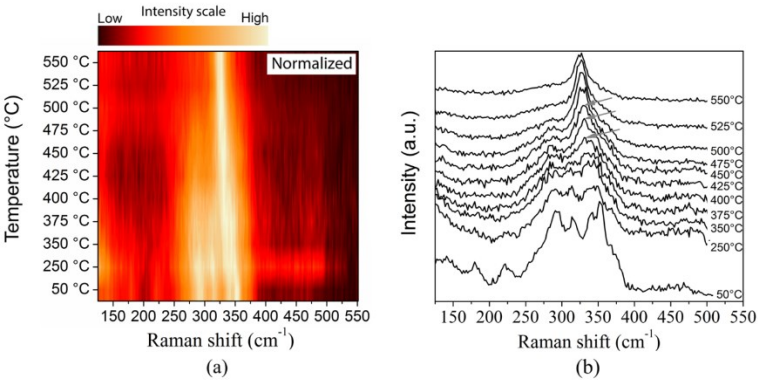

Fig. 4. (a) Normalized intensity plot that illustrates the spectral shift and evolution from the precursor stack into kesterite. (b) Raman spectra of the Mo/CTS/ZnS precursor stack during annealing from 50 °C to 550 °C. At 50 °C the spectrum of CTS can be observed. From 400 °C, the main A-mode of kesterite starts to appear. The evolution of this mode is indicated by the arrows and evolves up to 550 °C.

Kesterite synthesis from a Mo/CTS/ZnS precursor stack

The high temperature measurements discussed in the previous section will now be used as a reference for in situ monitoring of kesterite synthesis from the Mo/CTS/ZnS precursor stack and will be discussed in this section. The precursor stack prepared for the in situ monitoring of kesterite synthesis consists of approximately 1 micrometer thick CTS and a 300 nm ZnS layer.

As in the measurements discussed earlier on, an excitation wavelength of 532 nm was used. In order to obtain more information about phase transformations during the annealing process, temperature steps were decreased from 50 °C to 25 °C above 350 °C. Fig. 4 illustrates the evolution from the precursor stack to kesterite. In

Fig. 4(d) the Raman spectra are shown during the course of the annealing process. The process starts with the observation of the CTS Raman spectrum at 50 °C. The main A-mode of kesterite appears at 400 °C and gradually becomes more prominent, as indicated by the arrow (Fig. 4(b)). At 550 °C, the main A-mode solely dominates the spectrum.

As previously shown, CTS exhibits two vibrational modes in the region between 325 cm^{-1} and 360 cm^{-1} at 50 °C and the main A-mode of kesterite is present at 338 cm^{-1}. These two CTS modes overlap each other but at 50 °C they can be distinguished by deconvolution (see Fig. S2). At higher temperatures these modes overlap strongly and can be observed as one broader peak, as observed in Fig. 2. In order to distinguish CTS from CZTS, the broader CTS peak was fitted as one peak. The peak positions obtained were compared with the peak position of the main A-mode of CZTS. This enables the possibility to distinguish the main CZTS A-mode (338 cm^{-1}) from CTS.

The evolution of the peak positions is depicted in Fig. 5. Previous work [32], [33] on annealing of CZTS is also included in this figure. In these studies, the kesterite peak behaviour in a lower temperature regime from -220 to 180 °C was studied. The data from Sarswat et al. correspond to the new data obtained in this study. The data from Singh et al. illustrates a similar trend, but with a slight offset which might be explained by differences in the measurement setup. However, the CZTS 338 cm^{-1} A-mode at

coincides with several other studies found in literature [11], [14], [24]. Below 475 °C, the data for the stack-derived CZTS slightly deviates from the CZTS reference, indicating the influence of CTS. At 475 °C and higher, the stack data overlaps with the CZTS reference, confirming the presence of the kesterite phase.

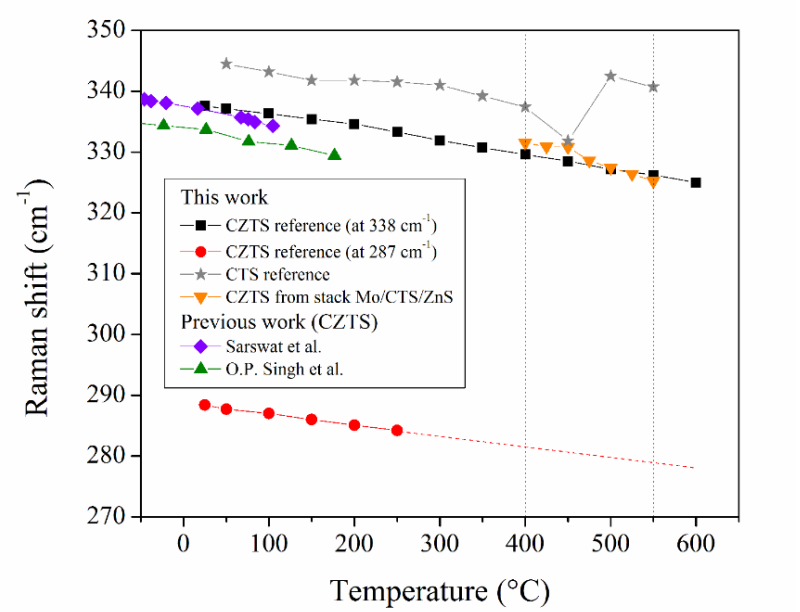

Fig. 5. Comparison of the evolution of peak positions of indicated vibrational modes of CTS, CZTS references and CZTS from CTS/ZnS precursor stack. Depicted are: fitted peak position of CTS in the 325 and 360 cm^{-1} range, the main A-modes (287 cm^{-1} and 338 cm^{-1}) of the CZTS references from this study and the fitted peak position of the CZTS main A-mode (338 cm^{-1}) synthesized from the Mo/CTS/ZnS precursor stack. Also depicted are the peak positions from the CZTS main A-mode as measured in studies from Sarswat et al. and O.P.Singh et al.

In order to further distinguish CTS from CZTS, the Raman modes of CTS found in this study and previous studies were compared with respect to temperature. The information is summarized in Tables SI and SII in the supplementary material. In previous studies, tetragonal Cu_2SnS_3 and orthorhombic Cu_3SnS_4 were observed in the range 336–338 cm^{-1} in films annealed up to 400 °C, but their intensity was relatively low [41,42]. A minor contribution is therefore expected of these CTS phases. In other studies, between 450–520 °C, tetragonal CTS was only observed at 330 cm^{-1}. In this study CTS only exhibits modes at 322 and 353 cm^{-1} at 550 °C, not at 338 cm^{-1} anymore. After the film has been cooled down, both kesterite A-modes can be observed as shown in Fig. 6.

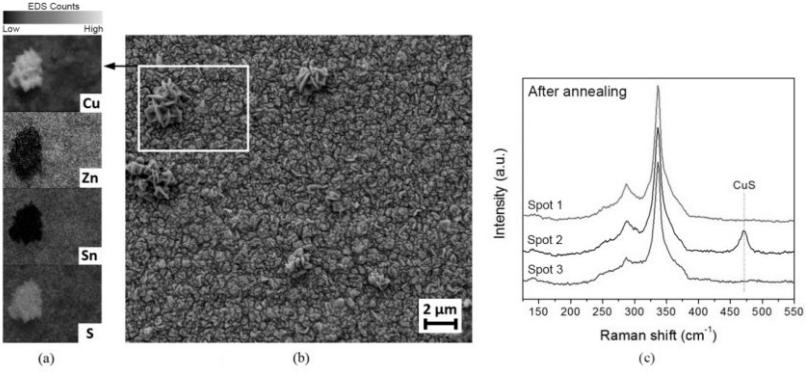

Fig. 6. (a) EDS maps of the elements copper, zinc, tin and sulfur. (b) Electron micrograph of the surface of the Mo/CTS/ZnS thin film after annealing. and some flower-like structures of CuS are present. (c) Also depicted are the Raman spectra of three different spots of the Mo/CTS/ZnS film after annealing measured at 50 °C. The main A-modes of CZTS are present and one spot also exhibits the presence of CuS as indicated by the vibrational mode at 475 cm^{-1}.

The surface of the film is homogeneous in composition after

annealing, apart from several flower-like structures as depicted in the electron micrograph (Fig. 6). Compositional analysis performed with EDS (7 kV) illustrates that these structures consist of copper sulfide. Since the structures are not uniformly distributed across the surface and the laser spot size is approximately 5 µm wide, they are only observed in the Raman spectrum if they fall within the laser excitation domain, and if the concentration is detectable. This is confirmed by Raman spectra taken at different spots which show a vibrational mode at 475 cm^{-1}, as shown in Fig. 6. Due to resonance conditions, ZnS can be easily detected with λ_{exc} = 325 nm, even when present in small concentrations [25]. ZnS could be detected, although the scattering intensity was substantially lower compared to the initial signal before annealing. The presence of secondary phases is likely since there was no background pressure of sulfur or selenium present during annealing. Also, 300 nm of ZnS is likely not enough to completely convert the CTS film into CZTS. Although, Cu_2SnS_3 is dominantly present in the film, minor contributions of other CTS phases make the formation of secondary phases, such as CuS and ZnS, also plausible.

Capabilities and limitations of Raman spectroscopy

It should be considered that Raman spectroscopy is a surface sensitive technique. Therefore, additional characterization (in situ or ex situ) is necessary to obtain full depth information of the thin film. Also, Raman spectroscopy is not able to detect the presence of small amounts of Cu_2SnS_3

(<30 %) in a CZTS film [35]. It is possible that certain modes overlap and this could make it more difficult to distinguish between e.g. tetragonal Cu_2SnS_3 and CZTS. But this depends on annealing temperature and relative intensity, as described in the previous section. Therefore, it is relevant to use reference films as illustrated in this study. Besides these drawbacks it is not likely that Cu_2SnS_3 will occur in CZTS films because of the Cu-poor and Zn-rich growing conditions.

Also, presence of other secondary phases strongly depends on the preparation method of the CZTS film. Co-evaporation or co-sputtering generally delivers more homogeneous thin films as opposed to preparation methods that utilize (metal) stacked precursors for the preparation of CZTS films.

This study illustrated the possibilities of Raman spectroscopy as a technique to monitor phase identification and phase evolution in thin films that consist of CTS, CZTS and a mixture of both. Furthermore, it can be used as a technique to obtain a temperature estimation in situ, based on the peak position of specific vibrational modes. Previous studies have shown it could also be used for fundamental material analysis to obtain information about crystallinity and underlying phonon processes. [25,33,43]

The intensity of the Raman signal does mainly depend on the material, excitation wavelength, acquisition time and working distance. The wavelength used will also determine the information depth. Resonance conditions will enhance signal intensity. Whether Raman spectroscopy can

be used in situ should be determined casewise. Within the scope of this study, but not depicted here, using an acquisition time of t_{acq} = 15 seconds resulted already in detection of the main A-mode at 338 cm^{-1} in the reference CZTS film. For consistency purposes, an acquisition time of 100 seconds was used in all experiments described here. In situ Raman spectroscopy can be used as a fast monitoring technique and might be beneficial for industrial purposes.

3.1.5 Conclusion

This work was performed to investigate the viability of Raman spectroscopy as a monitoring tool during high temperature annealing processing. CTS and CZTS films were prepared by co-evaporation and reactive sputtering with subsequent annealing, respectively. To obtain a reference measurement, both films were characterized by in situ Raman spectroscopy during high temperature annealing. It was found that vibrational modes of CTS and CZTS can be well observed at temperatures used in common practice annealing processes for kesterite synthesis.

Additionally, it was shown that a phase transition could be monitored during the annealing process of the CTS film. This was observed by analyzing the peak intensity of specific modes as well as their changing position in the course of the annealing process.

Furthermore, a Mo/CTS/ZnS precursor stack was prepared and used to demonstrate in situ monitoring of

CZTS synthesis. Above 400 °C, the appearance of the main A-mode at 338 cm^{-1} could be observed and its temperature-dependent evolution could be monitored. This is in agreement with the CZTS reference data obtained in this study and presented in other studies. The simultaneous detection of CTS and CZTS at higher temperatures shows that this method can also be used to detect unwanted phases during growth.

Also, the sample temperature can be derived in situ from fitting the CZTS main A-mode at 338 cm^{-1}. Most of the processes used to synthesize CZTS involve a high temperature annealing step in an inert gas atmosphere.

It was illustrated that Raman spectroscopy is a versatile technique that provides a simple and fast method for in situ process control and monitoring of the fabrication of CTS and CZTS thin film absorbers. Implementation of in situ Raman spectroscopy would be a step forward in controlling and monitoring crucial annealing steps during the preparation of such ternary and quaternary thin film absorbers.

Acknowledgements

We are grateful for the assistance of Lars Steinkopf with the preparation of the co-evaporated thin films. The research leading to these results has received funding from the People Program (Marie Curie Actions) of the European Union's Seventh Framework Program FP7/2007-2013/ under REA Grant Agreement No. 316488 (KESTCELLS). J.S.

would like to acknowledge the Swedish Research Council for funding.

3.1.6 References

[1] K. Ito and T. Nakazawa, “Electrical and Optical Properties of Stannite-Type Quarternary Semiconductor Thin Films,” Jpn. J. Appl. Phys., vol. 27, pp. 2094–2097, 1988.

[2] H. Katagiri, N. Ishigaki, T. Ishida, and K. Saito, “Characterization of Cu_2ZnSnS_4 Thin Films Prepared by Vapor Phase Sulfurization,” Jpn. J. Appl. Phys, vol. 40, no. 2A, pp. 500–504, 2001.

[3] S. Chen, X. G. Gong, A. Walsh, and S. H. Wei, “Defect physics of the kesterite thin-film solar cell absorber Cu_2ZnSnS_4,” Appl. Phys. Lett., vol. 96, no. 2, pp. 1–4, 2010.

[4] B. A. Schubert, B. Marsen, S. Cinque, T. Unold, R. Klenk, S. Schorr, and H. W. Schock, “Cu_2ZnSnS_4 thin film solar cells by fast coevaporation,” Prog. Photovoltaics Res. Appl., vol. 19, no. 1, pp. 93–96, 2011.

[5] S. M. Pawar, A. I. Inamdar, B. S. Pawar, K. V. Gurav, S. W. Shin, X. Yanjun, S. S. Kolekar, J. H. Lee, J. H. Kim, and H. Im, “Synthesis of Cu_2ZnSnS_4 (CZTS) absorber by rapid thermal processing (RTP) sulfurization of stacked metallic precursor films for solar cell applications,” Mater. Lett., vol. 118, pp. 76–79, 2014.

[6] C. K. Miskin, W. C. Yang, C. J. Hages, N. J. Carter, C. S. Joglekar, E. A. Stach, and R. Agrawal, “9.0% efficient $Cu_2Zn(S,Se)_4$ solar cells from selenized nanoparticle inks,” Prog. Photovoltaics Res. Appl., vol. 23, no. 5, pp. 654–659, 2015.

[7] J. J. Scragg, T. Kubart, J. T. Watjen, T. Ericson, M. K. Linnarsson, and C. Platzer-Bjorkman, “Effects of back contact instability on Cu_2ZnSnS_4 devices and processes,” Chem. Mater., vol. 25, no. 15, pp. 3162–3171, 2013.

[8] S. Giraldo, M. Neuschitzer, Y. Sanchez, H. Xie, M. Colina, M. Placidi, and P. Pistor, “Large performance improvement in $Cu_2ZnSnSe_4$ based solar cells by surface engineering with a nanometric Ge layer,” in IEEE Photovoltaic Specialist Conference (PVSC), 2015, vol. 42nd, pp. 8–12.

[9] L. Vauche, L. Risch, Y. Sánchez, M. Dimitrievska, M. Pasquinelli, T. Goislard de Monsabert, P.-P. Grand, S. Jaime-Ferrer, and E. Saucedo, “8.2% pure selenide kesterite thin-film solar cells from large-area electrodeposited precursors,” Prog. Photovoltaics Res. Appl., vol. 24, no. July 2015, p. 38, 2015.

[10] W. Wang, M. T. Winkler, O. Gunawan, T. Gokmen, T. K. Todorov, Y. Zhu, and D. B. Mitzi, “Device characteristics of CZTSSe thin-film solar cells with 12.6% efficiency,” Adv. Energy Mater., vol. 4, no. 7, pp. 1–5, 2014.

[11] M. Dimitrievska, A. Fairbrother, X. Fontané, T. Jawhari, V. Izquierdo-Roca, E. Saucedo, and A. Pérez-Rodríguez, “Multiwavelength excitation Raman scattering study of polycrystalline kesterite Cu_2ZnSnS_4 thin films,” Appl. Phys. Lett., vol. 104, no. 2, p. 21901, 2014.

[12] M. Y. Valakh, O. F. Kolomys, S. S. Ponomaryov, V. O. Yukhymchuk, I. S. Babichuk, V. Izquierdo-Roca, E. Saucedo, A. Perez-Rodriguez, J. R. Morante, S. Schorr, and I. V. Bodnar, “Raman scattering and disorder effect in Cu_2ZnSnS_4,” Phys. Status Solidi – Rapid Res. Lett., vol. 7, no. 4, pp. 258–261, 2013.

[13] X. Fontané, V. Izquierdo-Roca, E. Saucedo, S. Schorr, V. O. Yukhymchuk, M. Y. Valakh, A. Perez-Rodriguez, and J. R. Morante, “Vibrational properties of stannite and kesterite type compounds: Raman scattering analysis of $Cu_2(Fe,Zn)SnS_4$,” J. Alloys Compd., vol. 539, pp. 190–194, 2012.

[14] P. A. Fernandes, P. M. P. Salomé, and A. F. da Cunha, “Growth and Raman scattering characterization of Cu_2ZnSnS_4 thin films,” Thin Solid Films, vol. 517, no. 7, pp. 2519–2523, 2009.

[15] S. Schorr, “The crystal structure of kesterite type compounds: A neutron and X-ray diffraction study,” Sol. Energy Mater. Sol. Cells, vol. 95, no. 6, pp. 1482–1488, 2011.

[16] J. Just, D. Lützenkirchen-Hecht, R. Frahm, S. Schorr, and T. Unold, “Determination of secondary phases in kesterite Cu_2ZnSnS_4 thin films by x-ray absorption near edge structure analysis,” Appl. Phys. Lett., vol. 99, no. 2011, p. 262105, 2011.

[17] H. Katagiri, K. Jimbo, W. S. Maw, K. Oishi, M. Yamazaki, H. Araki, and A. Takeuchi, “Development of CZTS-based thin film solar cells,” Thin Solid Films, vol. 517, no. 7, pp. 2455–2460, 2009.

[18] Lafond, L. Choubrac, C. Guillot-Deudon, P. Deniard, and S. Jobic, “Crystal structures of photovoltaic chalcogenides, an intricate puzzle to solve: The cases of CIGSe and CZTS materials,” Zeitschrift fur Anorg. und Allg. Chemie, vol. 638, no. 15, pp. 2571–2577, 2012.

[19] M. Dimitrievska, A. Fairbrother, E. Saucedo, A. Pérez-Rodríguez, and Victor Izquierdo-Roca, “Secondary phase and Cu substitutional defect dynamics in kesterite $Cu_2ZnSnSe_4$ solar cells: impact on optoelectronic properties,” Sol. Energy Mater. Sol. Cells, vol. 149, pp. 304–309, 2015.

[20] Weber, R. Mainz, and H. W. Schock, “On the Sn loss from thin films of the material system Cu-Zn-Sn-S in high vacuum,” J. Appl. Phys., vol. 107, no. 1, 2010.

[21] M. Kumar, A. Dubey, N. Adhikari, S. Venkatesan, and Q. Qiao, “Strategic review of secondary phases, defects and defect-complexes in kesterite CZTS–Se solar cells,” Energy Environ. Sci., vol. 8, no. 11, pp. 3134–3159, 2015.

[22] G. Rey, A. Redinger, J. Sendler, T. P. Weiss, M. Thevenin, M. Guennou, B. El Adib, and S. Siebentritt, “The band gap of $Cu_2ZnSnSe_4$: Effect of order-disorder,” Appl. Phys. Lett., vol. 105, no. 11, pp. 2012–2016, 2014.

[23] Y. Ren, J. J. S. Scragg, C. Frisk, J. K. Larsen, S. Y. Li, and C. Platzer-Bjorkman, “Influence of the Cu_2ZnSnS_4 absorber thickness on thin film solar cells,” Phys. Status Solidi Appl. Mater. Sci., vol. 212, no. 12, pp. 2889–2896, 2015.

[24] J. J. S. Scragg, L. Choubrac, A. Lafond, T. Ericson, and C. Platzer-björkman, “A low-temperature order-disorder transition in Cu_2ZnSnS_4 thin films,” Appl. Phys. Lett., vol. 104, no. 4, pp. 2012–2016, 2014.

[25] Fairbrother, V. Izquierdo-Roca, X. Fontané, M. Ibáñez, A. Cabot, E. Saucedo, and A. Pérez-Rodríguez, “ZnS grain size effects on near-resonant Raman scattering: optical non-destructive grain size estimation,” CrystEngComm, vol. 16, no. 20, p. 4120, 2014.

[26] M. Valakh, V. Dzhagan, and I. Babichuk, “Optically induced structural transformation in disordered kesterite Cu_2ZnSnS_4,” JETP Lett., vol. 98, no. 5, pp. 292–295, 2013.

[27] R. Caballero, E. Garcia-Llamas, J. M. Merino, M. Leon, I. Babichuk, V. Dzhagan, V. Strelchuk, and M. Valakh, “Non-stoichiometry effect and disorder in Cu_2ZnSnS_4 thin films obtained by flash evaporation: Raman scattering investigation,” Acta Mater., vol. 65, pp. 412–417, 2014.

[28] M. Dimitrievska, A. Fairbrother, E. Saucedo, A. Pérez-Rodríguez, and V. Izquierdo-Roca, “Influence of compositionally induced defects on the vibrational properties of device grade $Cu_2ZnSnSe_4$ absorbers for kesterite based solar cells,” Appl. Phys. Lett., vol. 106, no. 7, 2015.

[29] R. Scheer, A. Pérez-Rodríguez, and W. K. Metzger, “Advanced diagnostic and control methods of processes and layers in CIGS solar cells and modules,” Prog. Photovoltaics Res. Appl., vol. 18, no. 6, pp. 467–480, 2010.

[30] S. van Duren, Y. Ren, J. Scragg, J. Just, and T. Unold, “Raman spectroscopy study on in-situ monitoring of Cu_2ZnSnS_4 synthesis,” in Proc. 42th IEEE Photovoltaic Spec. Conf, 2015, pp. 1–3.

[31] J. J. Scragg, T. Ericson, X. Fontané, V. Izquierdo-Roca, A. Pérez-Rodríguez, T. Kubart, M. Edoff, and C. Platzer-Björkman, “Rapid annealing of reactively sputtered precursors for Cu_2ZnSnS_4 solar cells,” Prog. Photovoltaics Res. Appl., vol. 22, no. 1, pp. 10–17, 2014.

[32] P. K. Sarswat, M. L. Free, and A. Tiwari, “Temperature-dependent study of the Raman A mode of Cu_2ZnSnS_4 thin films,” Phys. Status Solidi Basic Res., vol. 248, no. 9, pp. 2170–2174, 2011.

[33] O. P. Singh, N. Muhunthan, V. N. Singh, K. Samanta, and N. Dilawar, “Effect of temperature on thermal expansion and anharmonicity in Cu_2ZnSnS_4 thin films grown by co-sputtering and sulfurization,” Mater. Chem. Phys., vol. 146, no. 3, pp. 2–5, 2014.

[34] Y. Ren, J. J. Scragg, T. Ericson, T. Kubart, and C. Platzer Björkman, “Reactively sputtered films in the CuxS–ZnS–SnSy system: From metastability to equilibrium,” Thin Solid Films, vol. 582, pp. 208–214, 2015.

[35] D. M. Berg, M. Arasimowicz, R. Djemour, L. Gütay, S. Siebentritt, S. Schorr, X. Fontané, V. Izquierdo-roca, A. Pérez-rodriguez, and P. J. Dale, “Discrimination and detection limits of secondary phases in Cu_2ZnSnS_4 using X-ray diffraction and Raman spectroscopy,” Thin Solid Films, vol. 569, pp. 113–123, 2014.

[36] D. M. Berg, R. Djemour, L. Gütay, S. Siebentritt, P. J. Dale, X. Fontane, A. Pérez-rodriguez, D. M. Berg, R. Djemour, L. Gu, X. Fontane, V. Izquierdo-roca, and A. Pe, "Raman analysis of monoclinic Cu_2SnS_3 thin films Raman analysis of monoclinic Cu_2SnS_3 thin films," vol. 192103, no. 2012, 2016.

[37] S. Fiechter, M. Martinez, G. Schmidt, W. Henrion, and Y. Tomm, "Phase relations and optical properties of semiconducting ternary sulfides in the system Cu – Sn – S," J. Phys. Chem. Solids, vol. 64, pp. 1859–1862, 2003.

[38] A. Kanai, H. Araki, A. Takeuchi, H. Katagiri, I. Recently, E. The, and T. Cts, "Annealing temperature dependence of photovoltaic properties of solar cells containing Cu_2SnS_3 thin," vol. 1243, no. 6, pp. 1239–1243, 2015.

[39] L. L. Baranowski, K. Mclaughlin, P. Zawadzki, S. Lany, A. Norman, H. Hempel, R. Eichberger, T. Unold, E. S. Toberer, and A. Zakutayev, "Effects of Disorder on Carrier Transport in Cu_2SnS_3," vol. 44017, pp. 1–9, 2015.

[40] A. Cheng, "Imaging and phase identification of Cu_2ZnSnS_4 thin films using confocal Raman spectroscopy Imaging and phase identification of Cu_2ZnSnS_4 thin films using confocal Raman spectroscopy," vol. 51203, no. 2011, 2014.

[41] J. A. Marquez, S. Levcenko, J. Just, H. Hampel, I. Forbes, N. M. Pearsall, and T. Unold, “Earth abundant thin fi lm solar cells from co-evaporated Cu_2SnS_3 absorber layers,” J. Alloys Compd., vol. 689, pp. 182–186, 2016.

[42] P. A. Fernandes, P. M. P. Salomé, and A. F. da Cunha, “A study of ternary Cu_2SnS_3 and Cu_3SnS_4 thin films prepared by sulfurizing stacked metal precursors,” J. Phys. D. Appl. Phys., vol. 43, no. 21, p. 215403, 2010.

[43] M. Dimitrievska, A. Fairbrother, A. Perez-Rodriguez, E. Saucedo, and V. Izquierdo-Roca, “Raman scattering crystalline assessment of polycrystalline Cu_2ZnSnS_4 thin films for sustainable photovoltaic technologies: Phonon confinement model,” Acta Mater., vol. 70, pp. 272–280, 2014.

3.1.7 Supplementary information

Structural properties of CTS

The Gibbs phase triangle of the Cu-Sn-S system illustrates a substantial number of different phases, but from the pseudo-binary diagram of Cu_2S and SnS_2 the phases occuring below 600 °C are Cu_2SnS_3, Cu_4SnS_4, $Cu_2Sn_3S_7$ [1]. Depending on process conditions it might differ for a thin film prepared with co-evaporation, since this method does not necessarily guarantee thermal equilibrium during growth. Other work demonstrated a variety of phases and films characterized with Raman and XRD [2]–[5].

The co-evaporated CTS film was characterized with x-ray diffractometry in grazing incidence geometry at an angle of 0.5°. This angle was used in order to analyze the surface layer and to be able to correlate with the spectra obtained by Raman spectroscopy. The XRD penetration depth at this angle is approximately 130 nm. This was calculated by using the Lambert Beer law in combination with a compound attenuation length for Cu_2SnS_3 [6], [7] and an assumed XRD geometry [8]. The XRD pattern was compared with ICSD reference patterns as shown in Figure S1 and it matches with Cu_2SnS_3 predominantly.

Figure S2 illustrates CTS Raman spectra taken at 50 °C after each annealing step. Each spectrum is composed of the superposition of individual vibrational modes. In order to identify each mode, a deconvolution algorithm was applied to the spectrum and resulted in the separate contribution of

the individual modes. The spectrum was fitted based on the expected CTS vibrational modes as found in previous studies that were presented in literature [2]–[5].

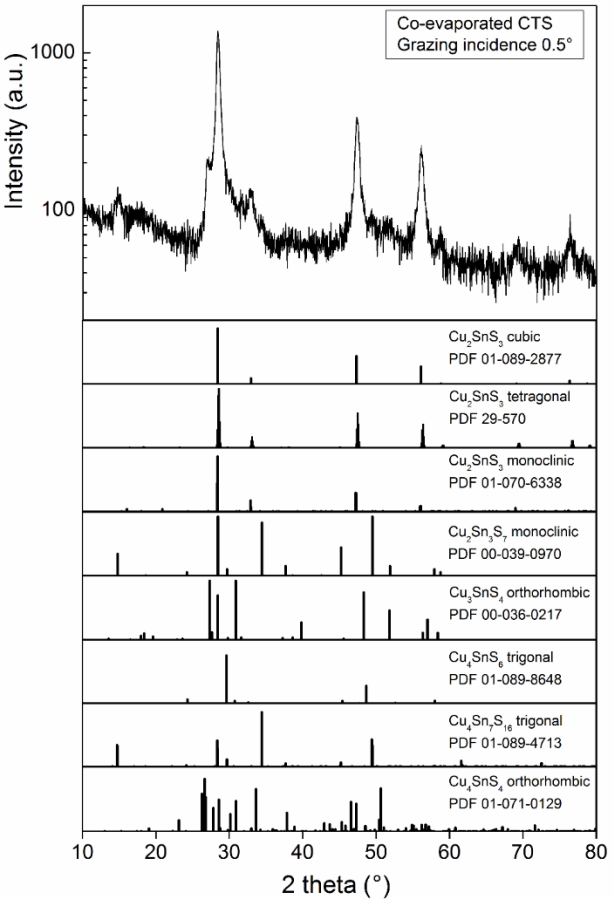

FIG. S1 GIXRD pattern of the co-evaporated CTS film at an incident angle of 0.5°. The dominant phase present is Cu_2SnS_3.

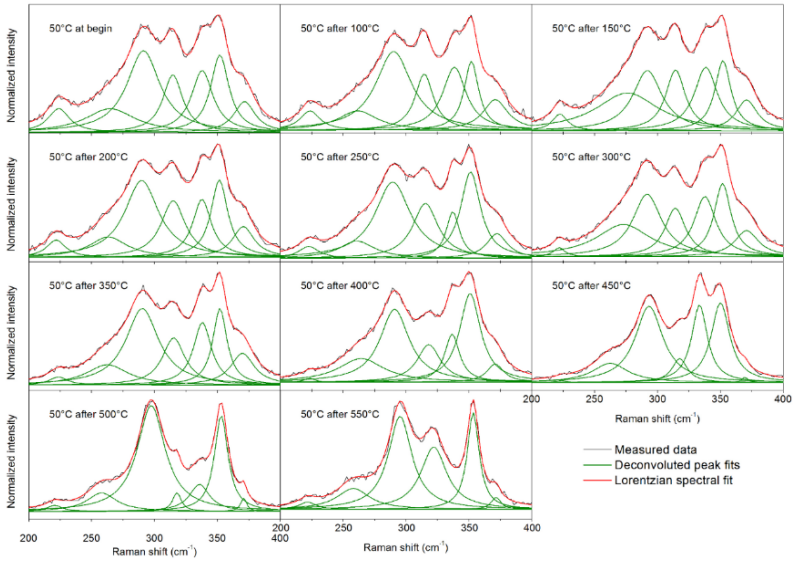

FIG. S2 CTS Raman spectra taken at 50 °C after annealing at indicated temperatures. Deconvolution of the Raman spectra was performed by applying a Lorentzian fit. The individual peak fits can be observed below the measured data. The spectral fit is a smooth curve fit and overlaps the measured data.

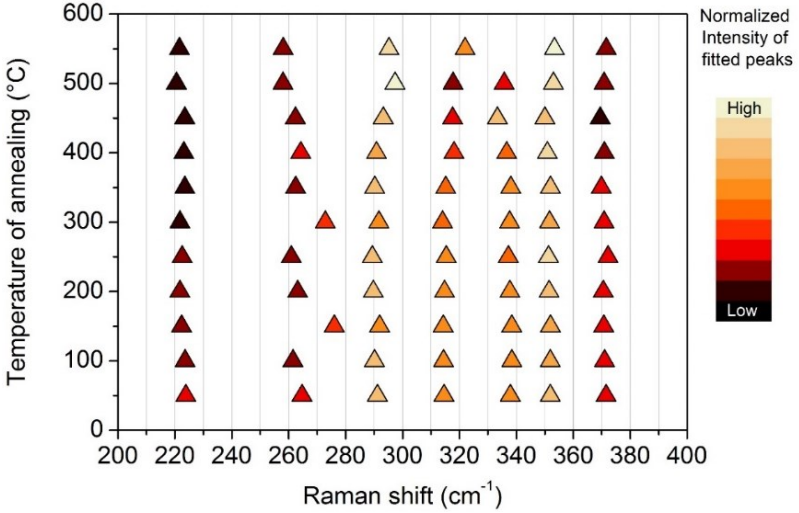

FIG. S3 CTS: Normalized peak intensity (color scale) of fitted peak positions (x-axis) after cooling down to 50 °C versus annealing temperature (y-axis). The fitted peak positions are obtained from the deconvoluted spectra in Figure S2.

Table SI.

Tabular respresentation of fig. S3. Raman shift peak positions at 50 °C after annealing at indicated temperature.

T/°C	Peak position (in cm^{-1})						
550	222	258	295	322	-	353	372
500	221	258	297	318	336	353	371
450	223	262	293	318	333	350	369
400	223	264	291	318	337	351	371
350	224	262	290	315	338	352	370
300	222	273	292	314	338	352	371
250	223	261	289	315	337	351	372
200	222	263	290	315	338	352	371
150	222	276	292	314	338	352	371
100	224	262	290	314	338	352	371
50	224	265	291	315	338	352	372

Table SII.

Raman shift peak positions (in cm^{-1}) found in literature assigned to cts phases prepared or annealed at the indicated temperature. References are indicated in between brackets and are stated at the bottom of the table.

	275-325 °C	**350-360 °C**	**400 °C**	**450 °C**	**500-520 °C**	**540-560 °C**
Cu_2SnS_3 (Cubic)	*299* [11] *303* [15] *352* [11] *354* [15]		*298* [12] *303* [13,14] *355* [14] *356* [12] *359* [13] *374* [13]			
Cu_2SnS_3 (Monoclinic)	*290* [10] *352* [10]	*287* [3] *354* [3]	*287* [3] *346* [3]	*287* [3] *348* [3]	*290* [3,10] *348* [3] *352* [10]	*290* [9,10,11] *351* [11] *352* [9,10]
Cu_2SnS_3 (Tetragonal)	*317* [11] *338* [11]	*336-337* [14] *338* [3] *351* [14]		*330* [3]	*330* [3]	
$Cu_2Sn_3S_7$					*315* [11] *371* [11]	*218* [9] *316* [9] *375* [9]
Cu_3SnS_4 (Orthorhombic)			*319* [13] *337-346* [13]		*295* [14] *318* [14] *348* [14]	*316* [9] *315-318* [15]
Cu_4SnS_4					*283* [12] *318* [12] *377* [12]	
$Cu_4Sn_7S_{16}$	*327* [10]					

[3] Chalapathi et al. 2013

[9] Berg et al. 2012

[10] Kanai et al. 2015

[11] Baranowski et al. 2015

[12] Cheng et al. 2011

[13] Marquez et al. 2016

[14] Fernandes et al. 2010

[15] Baranowski et al. 2014

References of supplementary information

[1] S. Fiechter, M. Martinez, G. Schmidt, W. Henrion, and Y. Tomm, “Phase relations and optical properties of semiconducting ternary sulfides in the system Cu – Sn – S,” J. Phys. Chem. Solids, vol. 64, pp. 1859–1862, 2003.

[2] N. Aihara, A. Kanai, K. Kimura, M. Yamada, K. Toyonaga, H. Araki, A. Takeuchi, and H. Katagiri, “Sulfurization temperature dependences of photovoltaic properties in Cu_2SnS_3 -based thin-film solar cells,” Jpn. J. Appl. Phys., vol. 53, no. 5S1, p. 05FW13, 2014.

[3] U. Chalapathi, Y. Jayasree, S. Uthanna, and V. Sundara Raja, “Effect of annealing temperature on the properties of spray deposited Cu_2SnS_3 thin films,” Phys. Status Solidi Appl. Mater. Sci., vol. 210, no. 11, pp. 2384–2390, 2013.

[4] P. A. Fernandes, P. M. P. Salomé, and A. F. da Cunha, “A study of ternary Cu_2SnS_3 and Cu_3SnS_4 thin films prepared by sulfurizing stacked metal precursors,” J. Phys. D. Appl. Phys., vol. 43, no. 21, p. 215403, 2010.

[5] H. Guan, H. Shen, C. Gao, and X. He, “Structural and optical properties of Cu_2SnS_3 and Cu_3SnS_4 thin films by successive ionic layer adsorption and reaction,” J. Mater. Sci. Mater. Electron., vol. 24, no. 5, pp. 1490–1494, 2013.

[6] X-Ray Mass Attenuation Coefficients, “X-Ray Mass Attenuation Coefficients”,http://physics.nist.gov/PhysRefData/XrayMassCoef/tab3.html. [Online].

[7] O. Madelung, U. Rössler, and M. Schulz, Eds., Ternary Compounds, Organic Semiconductors. Berlin, Heidelberg: Springer Berlin Heidelberg, 2000.

[8] M. Dimitrievska, A. Fairbrother, R. Gunder, G. Gurieva, H. Xie, E. Saucedo, A. Pérez-Rodríguez, V. Izquierdo-Roca, and S. Schorr, “Role of S and Se atoms on the microstructural properties of kesterite $Cu_2ZnSn(S_xSe_{1-x})_4$ thin film solar cells,” Phys. Chem. Chem. Phys., vol. 18, no. 12, pp. 8692–8700, 2016.

[9] D. M. Berg, R. Djemour, L. Gütay, S. Siebentritt, P. J. Dale, X. Fontane, A. Pérez-rodriguez, D. M. Berg, R. Djemour, L. Gu, X. Fontane, V. Izquierdo-roca, and A. Pe, “Raman analysis of monoclinic Cu_2SnS_3 thin films Raman analysis of monoclinic Cu_2SnS_3 thin films,” vol. 192103, no. 2012.

[10] A. Kanai, H. Araki, A. Takeuchi, H. Katagiri, I. Recently, E. The, and T. Cts, “Annealing temperature dependence of photovoltaic properties of solar cells containing Cu_2SnS_3 thin,” vol. 1243, no. 6, pp. 1239–1243, 2015.

[11] L. L. Baranowski, K. Mclaughlin, P. Zawadzki, S. Lany, A. Norman, H. Hempel, R. Eichberger, T. Unold, E. S. Toberer, and A. Zakutayev, “Effects of Disorder on Carrier Transport in Cu_2SnS_3 ,” vol. 44017, pp. 1–9, 2015.

[12] A. Cheng, “Imaging and phase identification of Cu_2ZnSnS_4 thin films using confocal Raman spectroscopy Imaging and phase identification of Cu_2ZnSnS_4 thin films using confocal Raman spectroscopy,” vol. 51203, no. 2011.

[13] J. A. Marquez, S. Levcenko, J. Just, H. Hampel, I. Forbes, N. M. Pearsall, and T. Unold, “Earth abundant thin fi lm solar cells from co-evaporated Cu_2SnS_3 absorber layers,” J. Alloys Compd., vol. 689, pp. 182–186, 2016.

[14] P. A. Fernandes, P. M. P. Salomé, and A. F. da Cunha, “A study of ternary Cu_2SnS_3 and Cu_3SnS_4 thin films prepared by sulfurizing stacked metal precursors,” J. Phys. D. Appl. Phys., vol. 43, no. 21, p. 215403, 2010.

[15] L. L. Baranowski, P. Zawadzki, S. Christensen, D. Nordlund, S. Lany, A. C. Tamboli, L. Gedvilas, D. S. Ginley, W. Tumas, E. S. Toberer, and A. Zakutayev, “Control of doping in Cu_2SnS_3 through defects and alloying,” Chem. Mater., vol. 26, no. 17, pp. 4951–4959, 2014.

3.2 Manuscript II – Pre-annealing of metal stack precursors and its beneficial effect on kesterite absorber properties and device performance

In a multistep process to fabricate kesterite films, metal multilayer (stack) precursor films can be sulfurized. A precursor pre-annealing step can be included to facilitate intermixing in the metallic precursor. The reason for a specific temperature and its influence on absorber properties is often unknown. This study follows a structural approach where alloying of the metallic precurors is performed at temperatures between 150 and 450 °C. The influence on material properties is investigated and correlated to the absorber films and solar device efficiency.

It is found that temperature influences presence of Sn and Cu-Sn alloys in the precursor and its formation can be monitored by in situ XRD. The presence of elemental Sn in the precursor increases SnS_2 in the bulk and on the surface of the absorbers. Consequently, device efficiency can be negatively correlated to the presence of SnS_2. This study shows that temperature is an important parameter in the precursor pre-annealing phase. An optimum temperature can be found to avoid Sn and SnS_2 in the precursor and absorber, respectively, in order to improve device efficiency.

Publication notification

Title: Pre-annealing of metal stack precursors and its beneficial effect on kesterite absorber properties and device performance.

Keywords*:* CZTS, Kesterite, Pre-annealing, Phase formation, Phase evolution, Thin film solar cells, In situ process control

Authors: Stephan van Duren[1], Diouldé Sylla[2], Andrew Fairbrother[2], Yudania Sánchez[2], Simón López-Marino[2], José A. Márquez Prieto[1], Victor Izquierdo-Roca[2], Edgardo Saucedo[2], Thomas Unold[1]

[1] Department Structure and Dynamics of Energy Materials, Helmholtz-Zentrum Berlin, Hahn-Meitner-Platz 1, 14109 Berlin, Germany.

[2] IREC, Catalonia Institute for Energy Research, Jardins de les Dones de Negre 1, Sant Adria de Besos, 08930 Barcelona, Spain

Journal: Solar Energy Materials and Solar Cells, Volume 185, October 2018, Pages 226-232, ISSN 0927-0248.
DOI: 10.1016/j.solmat.2018.04.022

My contribution:

Development and design of the in situ experiments. Performing the annealing experiments and characterization by XRF, Raman, SEM, IV, and XRD. All data analysis and writing of the manuscript.

3.2.1 Abstract

A variety of approaches is being used to fabricate kesterite absorbers, such as sputtering, co-evaporation and solution based techniques. Annealing at high temperatures is a common processing step to stimulate elemental mixing and grain growth. This study investigates the effect of pre-annealing of metal stack precursors at 150 °C, 200 °C, 300 °C and 450 °C on kesterite absorber and solar cell properties. Structural, morphological and vibrational properties of the thin films were investigated.

It was found that pre-annealing at 450 °C exhibited a structural mixture distinct from precursors annealed at lower temperatures. The absorber showed improved thickness uniformity, compositional surface homogeneity and absence of Sn-S phases. Lower temperatures resulted in Sn-S compounds in the absorber. In situ XRD is used to monitor phase transitions during pre-annealing. It is shown that implementing a pre-annealing step can improve the absorber properties and the device efficiency. The best performing solar cell had a 4.02 % efficiency and was achieved by pre-annealing the precursor layer at 450 °C.

3.2.2 Introduction

Kesterite, or Cu_2ZnSnS_4 (CZTS), has been proposed as a sustainable alternative to CIGS, since it consists of earth abundant and non-toxic materials. Additionally, it has a

direct optical bandgap between 1–1.5 eV and an absorption coefficient above 10^4 cm^{-1}. Kesterite thin films are typically aimed to be in the compositional region of 0.76–0.90 for Cu/(Zn+Sn) and 1.1–1.3 for Zn/Sn. It was shown before that off-stoichiometric films result in devices with better electronical properties as opposed to stoichiometric films [1]. Because of the narrow stoichiometric region of CZTS, off stoichiometric films are more likely to have secondary phases. Secondary phases have a detrimental effect on device performance. This was found for example with the presence of SnSe in CZTSe selenium based films [2]. Etching methods aim to remove phases such as CuS/Se, ZnS/Se and SnS/Se. However, they introduce an additional processing step which is less favorable for industrial use[3]–[6]. A variety of chemical and physical deposition techniques can be used to obtain films in this compositional range; sputtering[7], co-evaporation[6], spray-pyrolysis[8] and solution based spin coating[9]. Most of the processing methods involve a high temperature annealing step in order to stimulate elemental mixing and grain growth.

Several research groups are using metal stacks as a precursor for CZTS films in which the metal stack is ordered in different ways, e.g. Mo/Sn/Cu/Zn [10], [11], Mo/Zn/Sn/Cu [12], Mo/Zn/Cu-Sn [13] or Mo/CZT [14]–[16]. To prevent Sn loss this element is usually deposited as the bottom layer [17]. Cu can easily diffuse in both Zn and Sn when it is in the middle. Zn is a volatile compound and is sometimes placed at the bottom to prevent evaporation

during the process. Co-deposition of the metals is another approach and may improve homogeneity because of the readily mixed compound [18].

As part of a processing strategy, several groups have incorporated a soft annealing or pre-annealing step, which occurs with or without adding sulfur or selenium. This pre-annealing is implemented to stimulate diffusion and intermixing of the metals, such that reaction pathways for CZTS become dominant and compositional homogeneity of the film is promoted. An overview of studies that include a pre-annealing method is given in Table 1.

Table 1 Overview of studies where a similar pre-annealing of metal precursors was performed before commencing the sulfurization/selenization process.

Stacking order	Deposition technique	Atmosphere (Gas/P)	Time (min.)	Pre-annealing Temperature (°C)	PCE	S/ Se	Ref.
Mo/CZT	Electro co-deposition	Ar/H_2 (95/5 %)	30	350	-	Se	[19]
Mo/CZT	Electro co-deposition	Ar	10	350	2.64 %	Se	[14]
Mo/CZT	Electro co-deposition	Ar	-	450	3.74 %	S	[15]
Mo/CZT	Electro co-deposition	Ar	60	250/300/350	-	S	[16]
Mo/Cu/Sn/Zn	Electrodeposition	Inert gas/1000 Pa	30	300	8.2 %	Se	[20]
Mo/Cu-Sn/Zn	Electrodeposition	N_2	20	350	-	S	[21]
Mo/Cu/Sn/Cu/Zn	Electrodeposition	N_2	3	270	-	S	[17]
Mo/Zn/Cu-Sn	DC sputtering	Ar/10^5 Pa	60	350	4.4 %	S	[13]
Mo/Sn/Cu/Zn	DC sputtering	N_2	30	240	2.81 %	S	[22]
Mo/Sn/Cu/Zn	DC Sputtering	Ar/10^5 Pa	10	150/200/ 300/450	4.02 %	S	*This work*

In this study, a pre-annealing strategy is being implemented with regard to the metal precursor with Cu/(Zn/Sn) = 0.8 and Zn/Sn = 1.2. Separate precursors are pre-annealed at 150 °C,

200 °C, 300 °C and 450 °C. The effect of alloy formation on the structural and morphological properties of sulfurized films is investigated.

In particular, the relation between Cu-Sn and Sn in the precursors and Sn-S compounds in the absorber is investigated. The effect of Sn-S compounds on device performance of pure sulfide CZTS is also studied. Finally, XRD was explored as an in situ tool during pre-annealing to monitor the occurence of Sn-S compounds.

3.2.3 Experimental methods

Pre-annealing and absorber formation

The metallic stacks were prepared by DC magnetron sputtering using the deposition ordering glass/Mo/Sn/Cu/Zn. This sequence was chosen assuming that Cu diffuses easily into Sn and Zn and prevents Sn loss. Precursor films with compositional ratios of Cu/(Zn+Sn) = 0.8 and Zn/Sn = 1.2 were prepared.

Additional results of copper stoichiometric films (Cu/(Zn+Sn) = 1.0) can be found in the supplementary information. Pre-annealing was performed by placing the sample in a quartz crucible in a three zone tube furnace. A background pressure of 1 bar Ar was used. A ramping rate of 20 °C/min was used and the samples were naturally cooled down. The annealing temperature was held steady for 10 minutes. The time of ramping and natural cooling down is not included in the 10 minutes.

The sulfurization process took place in the same type of furnace. Separate tubes were used for pre-annealing and sulfurization in order to avoid preliminary inclusion of sulfur into the metal stack. In both annealing processes the tubes were flushed with Argon twice before starting. Samples were placed in a graphite box alongside 50 mg of finely ground sulfur powder (Alfa Aesar, 99.995 %). A ramping rate of 20 °C/min and a background pressure of 1 bar of Ar was used. The sulfurization was performed at 550 °C for 30 minutes and the samples were cooled down naturally.

Thin film characterization and solar cells

The compositional, structural, morphological and vibrational properties were studied respectively with x-ray fluorescence spectroscopy calibrated with ICP-OES (XRF, Fisherscope XVD), x-ray diffraction (XRD, Siemens D500 diffractometer) in θ-2θ configuration, scanning electron microscopy (SEM, ZEISS Series Auriga) using 5 kV and Raman spectroscopy with λ_{exc} = 633 nm. The Raman spectra were corrected with a Si reference line at 520 cm^{-1}. For the XRF measurement, 16 different points were taken on each sample. The average values were used to calculate the compositional ratios. The standard deviation of the ratio was approximately 0.05.

The absorbers were treated with an HCl etching method [4] in order to remove ZnS from the surface. Subsequently, 50 nm of CdS was deposited by a chemical bath deposition, followed by sputtering of 50nm undoped ZnO and 250 nm of ITO with 90 % of In_2O_3 and 10 % of SnO_2

(CT100 Sputtering System, Alliance Concepts). No additional heating is used during sputtering, temperatures will be approximately 100–150 °C. The solar cells were scribed in 3x3 mm^2 sections. Solar device characteristics were studied with a solar simulator (Abet 3000) under one sun illumination.

3.2.4 Results and discussion

Composition of alloyed precursor thin films

The compositional ratios of the pre-annealed precursors are depicted in Figure 1. The Zn/Sn ratio follows a decreasing trend at elevated pre-annealing temperatures. Some zinc loss is expected due to its high volatility and for being the top layer of the metal precursor stack.

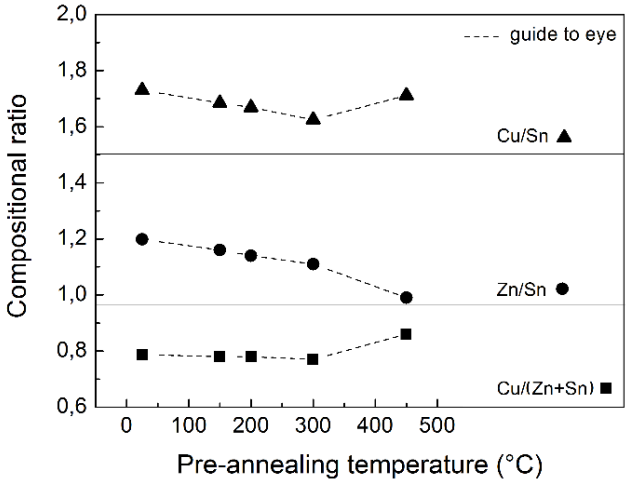

Figure 1 Comparison of compositional ratios of copper poor precursors with respect to pre-annealing temperatures. The dashed trend line serves as a guide to the eye.

Structural properties of precursors and absorbers

XRD patterns of the annealed films are depicted in Figure 2 as false-color intensity plots. Figure 2A and B show patterns of the pre-annealed precursors and absorbers, respectively. Elemental Sn is present up to 450 °C (arrow 1) in the precursors. The intensity evolution of elemental Sn (arrow 1) is in accordance with the evolution of the Sn peaks at 44–46°. In stoichiometric films, elemental Sn is only present up to 150 °C (see SI Fig.S5). The persistence of elemental Sn is expected in copper poor films, because there is higher competition between Zn and Sn to alloy with Cu than in stoichiometric films.

There is a broad contribution of Cu-Sn and Cu-Zn alloys in the 43° region (arrow 2). For higher temperatures, these peaks become more pronounced and narrow, indicating further crystallization of the alloys after pre-annealing at 200 °C and 300 °C. Note that above the melting point of Sn (230 °C), liquid Sn might facilitate intermixing.

Between 300 °C and 450 °C significant structural changes occur in the precursor film which is visible across the whole pattern. From the Cu-Sn phase diagram it can be seen that above 408 °C a transition from Cu_6Sn_5 → Sn(l) + Cu_3Sn takes place [23]. The Cu_3Sn reflection is observed at 42° (arrow 3). Because Cu_6Sn_5 dissolves, it is plausible that Cu_5Zn_8 becomes dominant in the 43° region. However, the reverse reaction takes place when cooling down. Therefore, it is likely that reflections from both Cu_6Sn_5 and Cu_5Zn_8 remain in this region where peaks nearly overlap. Also,

multiple reflections from Cu_6Sn_5 can still be found in the 27–39° region.

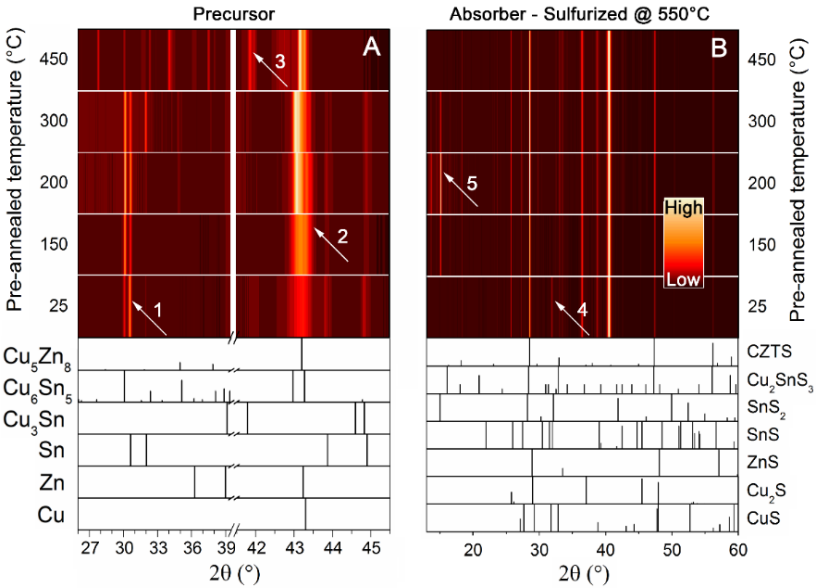

Figure 2 XRD patterns of copper poor precursors and absorbers. (A) Pre-annealed precursor films: arrow 1 indicates evolution of Cu_6Sn_5 and elemental Sn. Arrow 2 indicates Cu-Sn and Cu-Zn phases and arrow 3 shows presence of Cu_3Sn after pre-annealing at 450 °C. (B) Absorber films based on the pre-annealed precursors. Arrow 4 is related to SnS and arrow 5 indicates SnS_2. The regions indicated by arrows 1, 4 and 5 are presented in Figure 3 with more detail.

These are less present in the stoichiometric films at 450 °C pre-annealing (see SI, Fig.S5). Figure2B shows XRD patterns of the CZTS films obtained form sulfurization of the preannealed precursor stacks. The sample pre-annealed at 25 °C showed the presence of SnS in the absorber layer (arrow 4).

For the absorbers pre-annealed at 150, 200 and 300 °C SnS_2 was detected (arrow 5). No Sn-S binary phases

were detected in the absorber formed after pre-annealing the precursor at 450 °C. Figure 3 illustrates the correlation between the peak intensities of Sn in the precursor and Sn-S phases in the absorber (regions indicated by the arrows 1, 4 and 5 from Figure 2).

In Figure 3A, Cu poor precursors show a contribution of Sn up to 300 °C. Initially, the intensity of the Sn peak is higher than the Cu_6Sn_5 phase. Due to this presence of elemental Sn, SnS is easily formed in the absorber and shows a contribution at 32° (arrow 4, Figure2B). The intensity of elemental Sn between 150 °C and 300 °C fluctuates and remains below the intensity of the Cu_6Sn_5 phase. A similar trend can be observed for the SnS_2 phase in the absorbers. This is visually depicted in Figure3C, where dashed lines indicate resemblance between the intensity trend of the SnS_2 and Sn peaks in the absorbers and precursors respectively. This finding suggests that a higher content of elemental Sn in the precursor translates to a higher content of SnS_2 in the absorber. Diffraction peaks at 13° and 14.5° could not unambiguously be assigned to a precursor phase. However, it is plausible that these peaks are related to SnS_2 or Sn_2S_3 [24]. The intensity trend exactly resembles with SnS_2 at 15°.

Another indicator for this assumption is the absence of these peaks in the Cu-stoichiometric absorbers and the absence of the Sn peak (32°) in the stoichiometric precursors, pre-annealed above 200 °C.

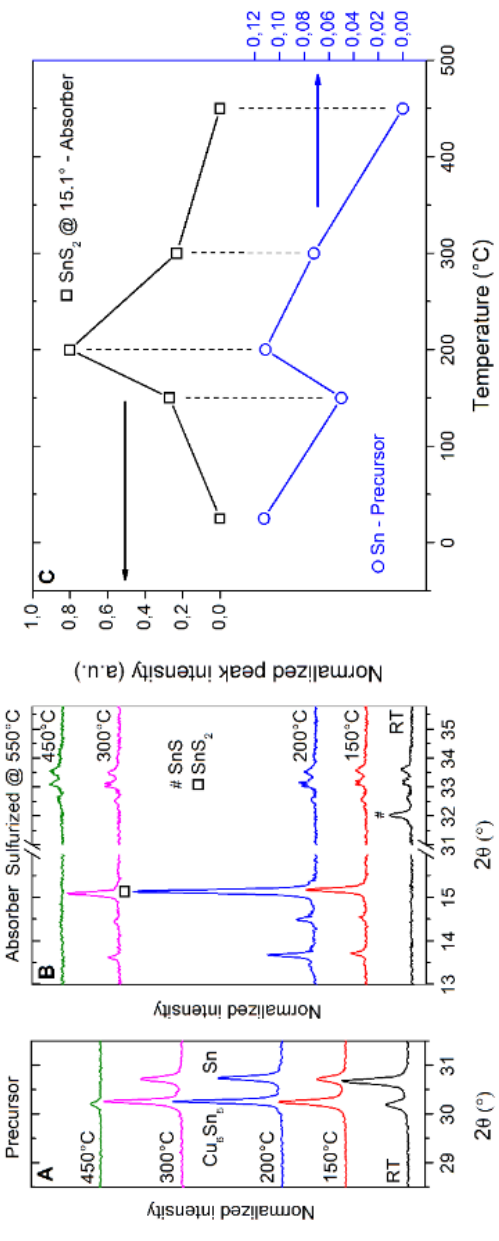

Figure 3 Magnified regions of the XRD patterns from Figure 2. Figure (A) depicts pre-annealed precursors and (B) absorbers. Figure (C) shows the intensity trend correlation between elemental Sn and SnS_2 peaks in precursors and absorbers, respectively.

The XRD patterns of the stoichiometric absorbers do not show the Sn-S compounds and appear therefore very similar between pre-annealing temperatures (See SI, Fig.S5). It was found that presence of elemental Sn in the precursor has led to the presence of Sn-S phases in the Cu poor absorbers. Other phases such as Cu-S are unlikely in Cu-poor films and Mo-S was not observed with SEM.

Morphological properties of absorbers

Figure 4 shows scanning electron micrographs (SEM) of the copper poor films. Figure 4a depicts the as-deposited precursor film or metal stack. The films appear to have a surface with pillar-like structures and channels in between. The upper surface layer consists of a fine granular structure (see SI, Fig.S1 for more detail). SEM energy-dispersive x-ray spectroscopy (EDX) measurements revealed there is less copper and tin present in the areas between the pillar structures. The smaller grains on top consist of Cu-Zn with Cu-Sn below, in line with the stacking order. The channels in between the pillars provide an additional pathway for sulfur to get into the film during sulfurization. All pre-annealed precursors show a similar morphology. There are several differences to be observed in the surface morphology of the absorbers (Figure 4b-f).

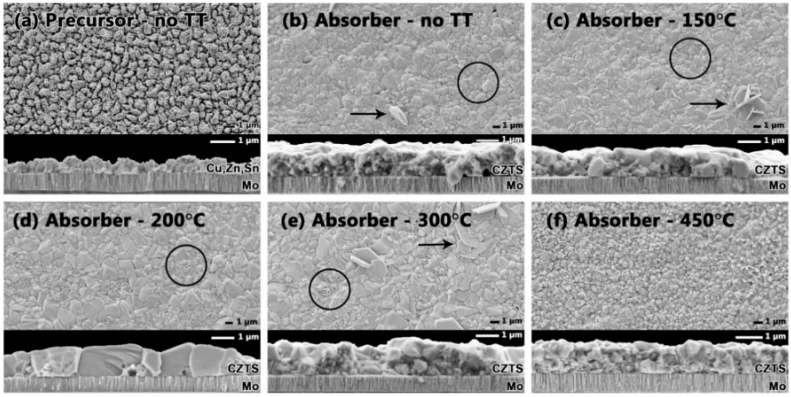

Figure 4 Top view and cross sectional electron micrographs of copper poor films (a) as-deposited precursor stack and (b-f) absorber films sulfurized at 550 °C. Indicated is the pre-annealing temperature. The arrows indicate presence of Sn-S platelike structures and the circles indicate a fine-grain structure that consists mainly of Zn-S.

The black arrows indicate Sn-S platelike structures and are distributed across surface areas 10-100 µm wide. These structures have been observed in other studies before [25]–[27]. Black circles indicate finer grains that consist of Zn-S. Some of these areas clearly follow the morphology of the precursors and have lower film thickness. This was concluded from careful analysis of the cross sections. In case of absorber (e), the Zn-S grains are mainly present on top of bigger grains. Furthermore, absorber (d), pre-annealed at 200 °C, has much bigger grain sizes and no presence of Sn-S structures on the surface. The absorber originated from the pre-annealed precursors at 450 °C (f) shows no Sn-S platelike structures on the surface and has a smaller grain size. As opposed to absorbers (b-e) there are no distinct areas with

obvious secondary phases, the grains are less densely packed and thickness variation is reduced.

Vibrational properties of absorbers

To understand more about the vibrational properties of the absorbers Raman spectroscopy was performed. The spectra were obtained after removal of ZnS by HCl etching and are shown in Figure 5. Different spots were taken on each film in order to account for the inhomogeneous distribution of the Sn-S surface structures. The vibrational modes at 263, 287, 337 and 366 cm^{-1} can be assigned to CZTS in the kesterite type structure[28].

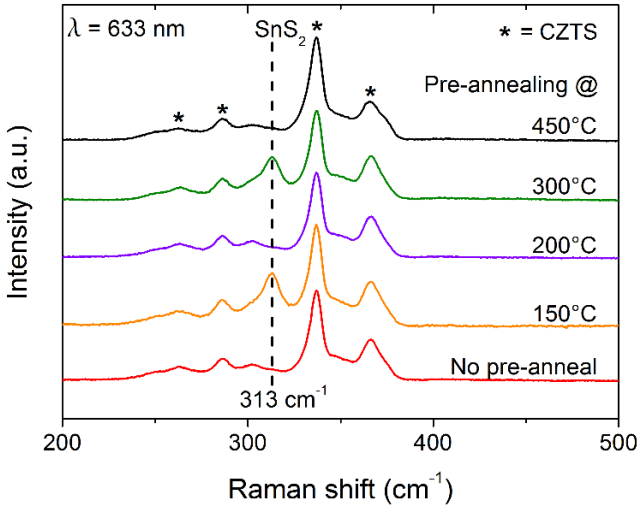

Figure 5 Raman spectra of copper poor absorbers after etching with HCl. Several vibrational modes of kesterite can be observed. At 313 cm^{-1} there is a contribution from SnS_2.

The mode at 313 cm^{-1} is related to SnS_2 and is assigned to the platelike structures on the surface [24], [27]. Several spots on the same sample were taken but the mode at 313 cm^{-1} was not always observed for absorbers pre-annealed at 150 °C and 300 °C. This aligns with observations from SEM that SnS_2 platelike structures are inhomogeneously distributed on a 10–100 µm scale.

Since Raman is a surface sensitive technique, it is concluded that SnS_2 detected by XRD in the 200 °C absorber originates from deeper regions in the film. This was also the case in a study by Ren et al., where SnS_2 was detected by XRD after 1 and 2 min annealing. However, in the form of surface structures it was only observed after 13 min annealing [24].

Device properties of copper poor solar cells.

Each absorber was divided into 3x3 mm^2 sections and resulted in >15 solar cells for each pre-annealing temperature. The results are depicted in Figure 6A with the boxplot method.

Absorbers pre-annealed at 450 °C resulted in cells that were significantly higher in PCE than cells from pre-annealing at 300 °C and lower, where PCEs are below 0.5 %. The performance of the 450 °C solar cells lie between 3.29 % and 4.02 %. The JV-curves of the mean, and maximum efficiency of the solar cells pre-annealed at 450 °C are depicted in Figure 6B, together with their device parameters.

The shunt resistance of cell 1 (96 Ω cm^2) is lower compared to cell 2 (211 Ω cm^2) causing a lower fill factor. The series resistances of the solar cells 1 and 2 are respectively 2.3 and 6.6 Ω cm^2. Shunts might be caused for example by local inhomogeneities, voids or pinholes. The remarkable result from this set of solar cells is the inverse proportionality between the XRD intensity of SnS_2 peaks (Figure 2B) and the PCEs of the corresponding absorbers that were pre-annealed at 150 °C, 200 °C, 300 °C. XRD patterns (Figure 3) show the highest intensity of the SnS_2 phases for the 200 °C pre-annealed absorber, yet the lowest PCEs.

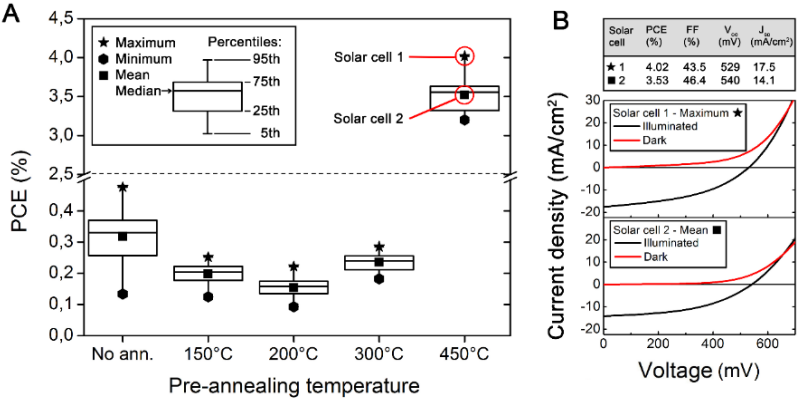

Figure 6 (A) Statistical boxplot representation of photo-conversion efficiencies (PCEs) of copper poor solar cells with respect to their pre-annealing treatment. Each boxplot presents > 15 solar cells on the same sample, for each pre-annealing temperature. The distribution of the PCEs is indicated by the percentiles as depicted in the legend. The minimum (hexagon), maximum (star), mean (square) and median PCEs are also indicated. For pre-annealing at 450 °C, cell 1 is the maximum value 4.02 %, cell 2 is the mean value that equals to 3.53 %. (B) JV-curves and device parameters are depicted for cell 1 and 2. The dark and illuminated (AM1.5) curves are both shown.

This suggest that tin phases within the bulk of the absorber are contributing negatively in addition to the Sn-S surface structures. The presence of these phases causes unwanted recombination centers. On the surface/interface they may act as a shunt pass [13]. This may explain why absorbers that were pre-annealed at 150 °C, 200 °C, 300 °C show almost no photovoltaic activity and PCEs < 0.5 %.

Pre-annealing at 450 °C has led to changes in structural properties and composition. These combined effects contributed to a distinct morphology and has led to the absence of SnS_2 on the surface. This resulted in better device performance as opposed to lower pre-annealing temperatures.

The precursor composition is slightly altered by the pre-annealing process (Figure 1). However, the composition remains in the Cu-poor and Zn-rich regime. The relatively lower Zn-rich nature can reduce formation of Zn-S phases. This might explain the absence of Zn-S surface clusters on the surface of the 450 °C absorber. Together with the absence of Sn-S platelikes, this resulted in a more homogeneous compositional surface distribution.

Also, pre-annealing at 450 °C results in a distinct XRD pattern (Figure 2A) with a variety of crystal structures of Cu_6Sn_5 and Cu_3Sn. Cu_3Sn was not observed below 450 °C. The Cu-Sn phase diagram shows that annealing above 408 °C facilitates formation of Cu_3Sn [23]. Since conversion of Cu_3Sn to Cu_6Sn_5 is an intermediate step in the formation of CZTS [29], [30], pre-annealing above 408 °C might accelerate the

formation of CTS, and thus CZTS, while Cu_3Sn is already present:

$$Cu_6Sn_5 \rightarrow 2\ Cu_3Sn + 3\ Sn \quad (1)$$

$$2\ Cu_3Sn + Sn + 9\ S \rightarrow 3\ Cu_2SnS_3 \quad (2)$$

$$Cu_2SnS_3 + ZnS \rightarrow Cu_2ZnSnS_4 \quad (3)$$

In situ monitoring of precursor annealing

Due to the relevance of the structural transitions in the pre-annealing stage, process monitoring and control is investigated with in situ XRD. The in situ measurements were obtained by using a heating stage together with the XRD setup described before.

Additional temperature steps were added at 75 °C, 175 °C, 225 °C, 375 °C, 400 °C and 425 °C to gain more information in ranges where transitions are expected based on the phase diagram. It should be noted that the measurement process was performed in one run. This means that the total heat exposure time is extended with respect to a single pre-annealing in a tube furnace. Also the volume of the heating stage is smaller. The inert gas and pressure are unchanged (Argon at 1 bar).

The in situ results can be found in Figure 7. A shift to smaller diffraction angles can be observed due to thermal expansion. In accordance with ex situ data, elemental Sn (30.5°) is observed at lower temperatures. Also, a broad contribution of Cu-Sn and Cu-Zn alloys can be observed at

43°. Above 225 °C, peak intensities of the alloys increase and line widths narrow, indicating better crystallinity.

Above 400 °C, as expected from the Cu-Sn phase diagram, a transition occurs related to Cu-Sn alloys.
The 2 2 -1 and 1 3 2 peaks of Cu_6Sn_5 at resp. 30.1° and 43°

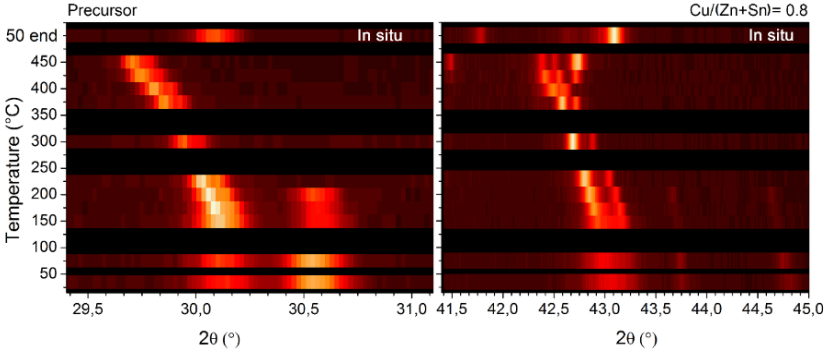

Figure 7 In situ XRD patterns obtained during pre-annealing of copper poor precursors. For the black areas there is no recorded data. After cooling down from 450 °C a pattern was acquired at 50 °C, this is indicated as '50 end'.

and the 3 3 0 peak of Cu_5Zn_8 at 43.2° are transformed into a 4 2 -2 peak of Cu_6Sn_5 at 43.3° , a 3 3 0 peak of Cu_5Zn_8 at 43.2° and a 0 0 2 peak of Cu_3Sn at 41.8° at 450 °C. A similar observation was made in the ex situ data (Figure 2). Although elemental Cu and Zn have reference peaks in the 42–45° range, it is unlikely that highly mixed films show a strong contribution from these elements.

In general, the in situ measurement resembles the ex situ measurements. With this relatively straightforward method it is possible to monitor phase transitions during high temperature pre-annealing to obtain a precursor with

desired structural properties for further absorber processing.

Perspective on Sn-S phases

Pre-annealing was found to stimulate the formation of different alloy phases and transitions between them in a Cu-Zn-Sn metal precursor stack. Free elemental Sn remains present up to 450 °C and promotes SnS and SnS_2 growth in the sulfurized absorbers. Sn-S platelike structures are observed on the surface and SnS_2 was found to be present in the bulk of the film.

The highest peak intensity of Sn and Cu_6Sn_5 was observed (Figure 3A) after pre-annealing at 200 °C and resulted in bigger grains in the absorber. A study by Chen et al. integrated SnS in the precursor and found a similar result. The stacking order glass/Mo/SnS/Cu/Sn/Zn was used [31]. This SnS layer facilitated formation of CTS. Reaction with a ZnS top layer formed CZTS and resulted in a densely packed film with bigger grains and no voids at the back. In another study, a CZTS layer was created from a Mo/CTS/ZnS stack. A similar result with respect to grain formation was observed [32].

In our study, it is plausible that the strong contribution from Sn and Cu-Sn facilitates formation of SnS and CTS at the back. Especially due to its presence in the deeper regions of the film where sulfur can access via the channels around the pillar-like structure. When Sn becomes liquid at 230 °C the process might be accelerated, resulting

in larger grains [33], [34]. Neuschitzer et al. observed enhanced grain growth by using a Ge nano-toplayer and tuning the Ge/Sn+Ge ratio [35]. Higher Ge content led to bigger grains but above 11 % it deteriorated device performance. Bigger grain growth was attributed to the presence of $SnSe_2$ phases during growth. Also, SnSe platelike structures on the surface were observed due to the substitution of Sn by Ge.

Even though bigger grains were observed in our study, a positive correlation with device performance was not observed. Devices with strong contribution of SnS_2 showed almost no PCE (Figure 6). Etching with $(NH_4)_2S$ can improve device performance between 20 to 65 % as found by Xie et al. [5]. However, although Sn-S on the surface can be etched away, the Sn-S present in the bulk would remain or etching might induce voids.

While etching is a method to remove Sn-S on the surface, it introduces an additional process step. An alternative approach would be to integrate SnS in the precursor as proposed by Chen et al. who discussed SnS as a passivating layer with several benefits; suppressed backside decomposition of CZTS, improved crystallinity and homogeneity [31]. It resulted in a void free absorber with densely packed grains and showed better PCE than a reference film without passivating layer. Kumar et al. modelled a device with SnS as a passivating layer and SnS_2 as a buffer layer [36]. The SCAPS model of Mo/p-SnS/p-CZTS/n- SnS_2/ZnO showed an improved Voc, Jsc and FF with

respect to other cell configurations without SnS. Integration of SnS could lead to more sustainable kesterite films. Succesful experimental integration as a buffer layer in CIGSe was previously demonstrated [37].

Alternatively to etching or integrating Sn-S phases, controlling process parameters might help prevent these phases to occur. A possible reduction of SnS on the surface might be achieved by controlling the partial pressure of sulfur. A recent study by Alvarez et al. on CZTS showed that partial pressures $P_S > 0.34$ bar caused SnS_2 flakes to form on the surface. There was no Sn loss observed but rather a displacement. SnS_2 structures were confirmed by XRD (15°) and Raman (314 cm^{-1}) [27]. A quasi in situ method was used by Ren et al. to monitor the sulfur partial pressures by means of a Sn-S reference film [24]. Presence of SnS_2 and absence of SnS/Sn_2S_3 generally meant that the P_S and annealing time were sufficient. SnS platelets were only observed after 13 min annealing, while SnS_2 was already observed by XRD after 1-2 minutes annealing. Alvarez found that the cooling rate had little effect on the surface morphology and presence of SnS flakes [27]. They concluded that SnS flakes are a consequence of gaseous Sulfur that keeps reacting with Sn on the surface layers.

3.2.5 Conclusion

This study investigated the effect of pre-annealing of Mo/Sn/Cu/Zn stacks on structural, morphological and

vibrational absorber properties in relation to solar cell performance. The XRD peak intensities of Cu_6Sn_5 and Sn could be correlated to SnS_2 in the absorber. Also, presence of SnS_2 was negatively correlated to device performance. Pre-annealing at 200 °C resulted in the biggest grain sizes and highest XRD peak intensity of SnS_2. Surface presence of ZnS and SnS_2 was observed with resp. SEM and Raman, except for the 450 °C pre-annealed absorber. Only pre-annealing at 450 °C resulted in an absorber with a homogeneous surface distribution of the elements. This absorber showed absence of SnS_2 and the highest PCE of 4.02 %. Furthermore, it was shown that in situ XRD can be used to monitor the pre-annealing process. This provides the possibility to obtain a precursor with certain structures and compounds favorable to absorber properties. This study paves the way to create an optimal precursor leading to a CZTS absorber with beneficial properties to device performance.

Acknowledgements
The research leading to these results has received funding from the People Program (Marie Curie Actions) of the European Union's Seventh Framework Program FP7/2007-2013/ under REA Grant Agreement No. 316488 (KESTCELLS).

3.2.6 References

[1] K. Ito, *Copper Zinc Tin Sulfide-Based Thin-Film Solar Cells*. 2015.

[2] S. Temgoua, R. Bodeux, N. Naghavi, and S. Delbos, "Effects of SnSe2 secondary phases on the efficiency of $Cu_2ZnSn(S_x,Se_{1-x})_4$ based solar cells," *Thin Solid Films*, vol. 582, pp. 215–219, 2015.

[3] I. D. Olekseyuk, I. V. Dudchak, and L. V. Piskach, "Phase equilibria in the Cu_2S-ZnS-SnS_2 system," *J. Alloys Compd.*, vol. 368, no. 1–2, pp. 135–143, 2004.

[4] A. Fairbrother, E. García-Hemme, V. Izquierdo-Roca, X. Fontané, F. A. Pulgarín-Agudelo, O. Vigil-Galán, A. Pérez-Rodríguez, and E. Saucedo, "Development of a Selective Chemical Etch To Improve the Conversion Efficiency of Zn-Rich Cu_2ZnSnS_4 Solar Cells," *J. Am. Chem. Soc.*, vol. 134, no. 19, pp. 8018–8021, 2012.

[5] H. Xie, Y. Sánchez, S. López-Marino, M. Espíndola-Rodríguez, M. Neuschitzer, D. Sylla, A. Fairbrother, V. Izquierdo-Roca, A. Pérez-Rodríguez, and E. Saucedo, "Impact of Sn (S, Se) Secondary Phases in $Cu_2ZnSn(S,Se)_4$ Solar Cells: a Chemical Route for Their Selective Removal and Absorber Surface Passivation," *ACS Appl. Mater. Interfaces*, vol. 6, no. 15, pp. 12744–12751, 2014.

[6] B. A. Schubert, B. Marsen, S. Cinque, T. Unold, R. Klenk, S. Schorr, and H. W. Schock, "Cu_2ZnSnS_4 thin film solar cells by fast coevaporation," *Prog. Photovoltaics Res. Appl.*, vol. 19, no. 1, pp. 93–96, 2011.

[7] Y. Ren, J. J. Scragg, T. Ericson, T. Kubart, and C. Platzer Björkman, "Reactively sputtered films in the Cu_xS–ZnS–SnS_y system: From metastability to equilibrium," *Thin Solid Films*, vol. 582, pp. 208–214, 2015.

[8] M. Espindola-Rodríguez, J. López-García, D. Sylla, X. Fontané, Y. Sánchez, S. López-Marino, V. Izquierdo-Roca, W. Riedel, W. Ohm, S. Gledhill, O. Vigil-Galán, and E. Saucedo, "Cu_2ZnSnS_4 absorber layers deposited by spray pyrolysis for advanced photovoltaic technology," *Phys. Status Solidi Appl. Mater. Sci.*, vol. 212, no. 1, pp. 126–134, 2015.

[9] S. G. Haass, M. Diethelm, M. Werner, B. Bissig, Y. E. Romanyuk, and A. N. Tiwari, "11.2% Efficient Solution Processed Kesterite Solar Cell with a Low Voltage Deficit," *Adv. Energy Mater.*, vol. 5, no. 18, pp. 1–7, 2015.

[10] A. Fairbrother, X. Fontané, V. Izquierdo-Roca, M. Espíndola-Rodríguez, S. López-Marino, M. Placidi, L. Calvo-Barrio, A. Pérez-Rodríguez, and E. Saucedo, "On the formation mechanisms of Zn-rich Cu_2ZnSnS_4 films prepared by sulfurization of metallic stacks," *Sol. Energy Mater. Sol. Cells*, vol. 112, pp. 97–105, 2013.

[11] K. M. Kim, S. Kim, H. Tampo, H. Shibata, K. Matsubara, and S. Niki, "Effect of pre-annealing on $Cu_2ZnSnSe_4$ thin-film solar cells prepared from stacked Zn/Cu/Sn metal precursors," *Mater. Lett.*, vol. 176, pp. 78–82, 2016.

[12] S. M. Pawar, A. I. Inamdar, B. S. Pawar, K. V. Gurav, S. W. Shin, X. Yanjun, S. S. Kolekar, J. H. Lee, J. H. Kim, and H. Im, "Synthesis of Cu_2ZnSnS_4 (CZTS) absorber by rapid thermal processing (RTP) sulfurization of stacked metallic precursor films for solar cell applications," *Mater. Lett.*, vol. 118, pp. 76–79, 2014.

[13] J. H. Lee, H. J. Choi, W. M. Kim, J. H. Jeong, and J. K. Park, "Effect of pre-annealing on the phase formation and efficiency of CZTS solar cell prepared by sulfurization of Zn/(Cu,Sn) precursor with H_2S gas," *Sol. Energy*, vol. 136, pp. 499–504, 2016.

[14] R. Kondrotas, R. Juškenas, A. Naujokaitis, G. Niaura, Z. Mockus, S. Kanapeckait, B. Čechavičius, K. Juškevičius, E. Saucedo, and Y. Sánchez, "Investigation of selenization process of electrodeposited Cu-Zn-Sn precursor for $Cu_2ZnSnSe_4$ thin-film solar cells," *Thin Solid Films*, vol. 589, no. August, pp. 165–172, 2015.

[15] Y. Li, T. Yuan, L. Jiang, F. Liu, Y. Liu, and Y. Lai, "Cu_2ZnSnS_4 thin film solar cell fabricated by co-electrodeposited metallic precursor," *J. Mater. Sci. Mater. Electron.*, vol. 26, no. 1, pp. 204–210, 2014.

[16] K. V. Gurav, S. M. Pawar, S. W. Shin, M. P. Suryawanshi, G. L. Agawane, P. S. Patil, J. H. Moon, J. H. Yun, and J. H. Kim, “Electrosynthesis of CZTS films by sulfurization of CZT precursor: Effect of soft annealing treatment,” *Appl. Surf. Sci.*, vol. 283, pp. 74–80, 2013.

[17] J. J. Scragg, T. Ericson, T. Kubart, M. Edoff, and C. Platzer-Björkman, “Chemical Insights into the Instability of Cu_2ZnSnS_4 Films during Annealing,” *Chem. Mater.*, vol. 23, no. 20, pp. 4625–4633, 2011.

[18] C. Andres, S. G. Haass, Y. E. Romanyuk, and A. N. Tiwari, “9.4% efficient $Cu_2ZnSnSe_4$ solar cells from co-sputtered elemental metal precursor and rapid thermal annealing,” *Thin Solid Films*, vol. 633, pp. 141–145, 2017.

[19] R. Juškenas, G. Niaura, Z. Mockus, S. Kanapeckaite, R. Giraitis, R. Kondrotas, A. Naujokaitis, G. Stalnionis, V. Pakštas, and V. Karpavičiene, “XRD studies of an electrochemically co-deposited Cu-Zn-Sn precursor and formation of a $Cu_2ZnSnSe_4$ absorber for thin-film solar cells,” *J. Alloys Compd.*, vol. 655, pp. 281–289, 2016.

[20] L. Yao, J. Ao, M. J. Jeng, J. Bi, S. Gao, G. Sun, Q. He, Z. Zhou, Y. Sun, and L. B. Chang, “A CZTSe solar cell with 8.2% power conversion efficiency fabricated using electrodeposited Cu/Sn/Zn precursor and a three-step selenization process at low Se pressure,” *Sol. Energy Mater. Sol. Cells*, vol. 159, pp. 318–324, 2017.

[21] M. I. Khalil, O. Atici, A. Lucotti, S. Binetti, A. Le Donne, and L. Magagnin, "CZTS absorber layer for thin film solar cells from electrodeposited metallic stacked precursors (Zn/Cu-Sn)," *Appl. Surf. Sci.*, vol. 379, pp. 91–97, 2016.

[22] Z. Jiang, S. Wang, Z. Li, M. Yang, S. Liu, Y. Lu, Q. Zhao, and R. Hao, "Influence of sulfurization conditions on properties of Cu_2ZnSnS_4 films and cells," *Thin Solid Films*, vol. 616, pp. 780–785, 2016.

[23] S. Fürtauer, D. Li, D. Cupid, and H. Flandorfer, "The Cu-Sn phase diagram, Part I: New experimental results," *Intermetallics*, vol. 34, pp. 142–147, 2013.

[24] Y. Ren, N. Ross, J. K. Larsen, K. Rudisch, J. J. S. Scragg, and C. Platzer-Björkman, "Evolution of Cu_2ZnSnS_4 during Non-Equilibrium Annealing with Quasi-in Situ Monitoring of Sulfur Partial Pressure," *Chem. Mater.*, vol. 29, no. 8, pp. 3713–3722, 2017.

[25] Y. B. Yang, J. K. Dash, A. J. Littlejohn, Y. Xiang, Y. Wang, J. Shi, L. H. Zhang, K. Kisslinger, T. M. Lu, and G. C. Wang, "Large Single Crystal SnS_2 Flakes Synthesized from Coevaporation of Sn and S," *Cryst. Growth Des.*, vol. 16, no. 2, pp. 961–973, 2016.

[26] Y. Ren, M. Richter, J. Keller, A. Redinger, T. Unold, O. Donzel-Gargand, J. J. S. Scragg, and C. Platzer Björkman, "Investigation of the SnS/ Cu_2ZnSnS_4 Interfaces in Kesterite Thin-Film Solar Cells," *ACS Energy Lett.*, vol. 2, no. 5, pp. 976–981, 2017.

[27] A. Alvarez, S. Exarhos, and L. Mangolini, “Tin disulfide segregation on CZTS films sulfurized at high pressure,” *Mater. Lett.*, vol. 165, no. November, pp. 41–44, 2016.

[28] M. Dimitrievska, A. Fairbrother, X. Fontané, T. Jawhari, V. Izquierdo-Roca, E. Saucedo, and A. Pérez-Rodríguez, “Multiwavelength excitation Raman scattering study of polycrystalline kesterite Cu_2ZnSnS_4 thin films,” *Appl. Phys. Lett.*, vol. 104, no. 2, p. 021901, 2014.

[29] R. Schurr, A. Hölzing, S. Jost, R. Hock, T. Voß, J. Schulze, A. Kirbs, A. Ennaoui, M. Lux-Steiner, A. Weber, I. Kötschau, and H. W. Schock, “The crystallisation of Cu_2ZnSnS_4 thin film solar cell absorbers from co-electroplated Cu-Zn-Sn precursors,” *Thin Solid Films*, vol. 517, no. 7, pp. 2465–2468, 2009.

[30] J. J. Scragg, “Studies of Cu_2ZnSnS_4 films prepared by sulfurisation of electrodeposited precursors,” *Thesis*, p. 262, 2010.

[31] H. J. Chen, S. W. Fu, S. H. Wu, T. C. Tsai, H. T. Wu, and C. F. Shih, “Impact of SnS Buffer Layer at Mo/ Cu_2ZnSnS_4 Interface,” *J. Am. Ceram. Soc.*, vol. 99, no. 5, pp. 1808–1814, 2016.

[32] J. Just, “Korrelationen struktureller und elektronischer Eigenschaften in Kesterit-Dünnschichten , Nanokristallen und -Solarzellen,” 2015.

[33] S. Giraldo, M. Neuschitzer, Y. Sanchez, H. Xie, M. Colina, M. Placidi, and P. Pistor, “Large performance improvement in $Cu_2ZnSnSe_4$ based solar cells by surface engineering with a nanometric Ge layer,” in *IEEE Photovoltaic Specialist Conference (PVSC)*, 2015, vol. 42nd, pp. 8–12.

[34] M. Neuschitzer, S. Giraldo, J. Marquez, M. Dimitrievska, M. Placidi, I. Forbes, V. Izquierdo-Roca, A. Perez-Rodriguez, and E. Saucedo, “Enhancing grain growth and boosting Voc in CZTSe absorber layers - Is Ge doping the answer?,” *Conf. Rec. IEEE Photovolt. Spec. Conf.*, vol. 2016–Novem, no. June, pp. 183–187, 2016.

[35] M. Neuschitzer, J. Marquez, S. Giraldo, M. Dimitrievska, M. Placidi, I. Forbes, V. Izquierdo-Roca, A. Pérez-Rodriguez, and E. Saucedo, “Voc Boosting and Grain Growth Enhancing Ge-Doping Strategy for $Cu_2ZnSnSe_4$ Photovoltaic Absorbers,” *J. Phys. Chem. C*, vol. 120, no. 18, pp. 9661–9670, 2016.

[36] A. Kumar and A. D. Thakur, “Analysis Of SnS_2 Buffer Layer And SnS Back Surface Layer Based CZTS Solar Cells Using SCAPS,” pp. 1–5.

[37] J. H. Kim, D. H. Shin, H. S. Kwon, and B. T. Ahn, “Growth of $Sn(O,S)_2$ buffer layers and its application to $Cu(In,Ga)Se_2$ solar cells,” *Curr. Appl. Phys.*, vol. 14, no. 12, pp. 1803–1808, 2014.

3.2.7 Supplementary information

The supplementary information (SI) provides additional information on copper poor films and includes data of copper stoichiometric films.

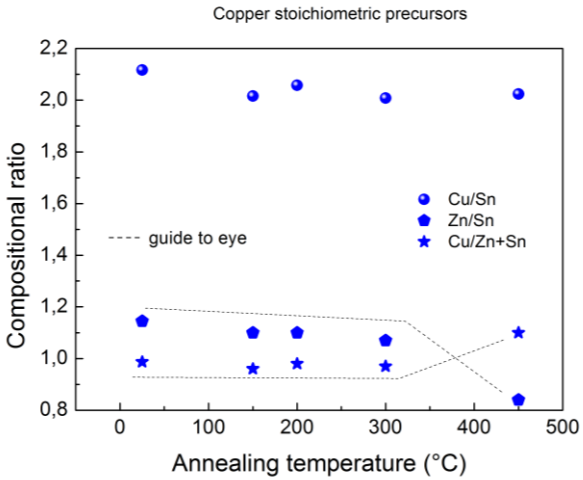

Figure S1 Compositional ratios of pre-annealed copper stoichiometric precursors.

Figure S2 shows a typical top view image of the precursor. Whether the precursor is pre-annealed, cu poor or stoichiometric does not change the appearance significantly. The channels in between the pillar-like structures are low in Cu and Sn, but have Zn present. Annealed stoichiometric precursors are shown in Figure S3. Growth of dense grains occur scarcely in the stoichiometric films as opposed to the copper poor films.

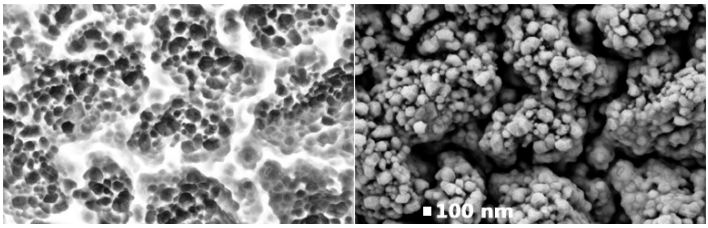

Figure S2 Close-up of precursor with small Zn rich grains on top. Regions between the grainy structures have a lower density of copper and tin. Left: a negative image to emphasize the channels around the pillar-like structures.

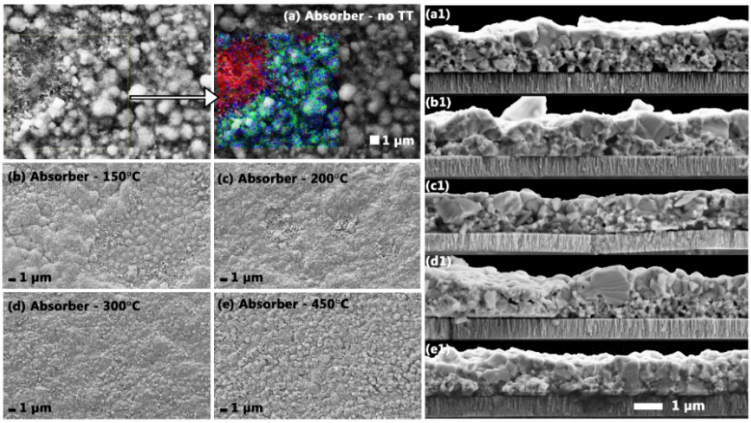

Figure S3 Topview (a,b,..) and crossectional (a1,b1,..) scanning electron micrographs of copper stoichiometric absorbers of which precursors were pre-annealed at stated temperatures. (a) topview: precursor with no temperature treatment (no TT). SEM EDX analysis shows the red area is Zn rich and deficient in Cu and Sn, indicating presence of ZnS.

Pre-annealed at 150 °C has a similar surface morphology as the unannealed based absorber. The pillar-like surface has transformed into a cauliflower structure. Lateral inhomogeneity is present and regions with smaller grains are Zn-rich and Cu- and Sn-poor. Similar to the copper poor

films. The cross sectional images look similar and appear to have a bi-layer structure with a smaller and porous grains closer to the bottom. As opposed to the copper poor films, there are no Sn-S platelike surface structures. This is expected in copper stoichiometric films, where CTS and CZTS are much more likely to occur than binary phases due to the abundance of copper.

Both absorbers (poor/stoichiometric) pre-annealed at 450 °C have a similar surface morphology. CTS was observed with Raman spectroscopy (Figure S4) on the surface layers of copper stoichiometric absorbers. Figure S5 shows false-color plots of the ex situ XRD patterns of the copper poor and stoichiometric films compared. The patterns were obtained after pre-annealing and sulfurization. Four parts with each five xrd patterns are shown with indicated temperature. The copper poor films have already been discussed in the main text but are included in the figure for comparison purposes.

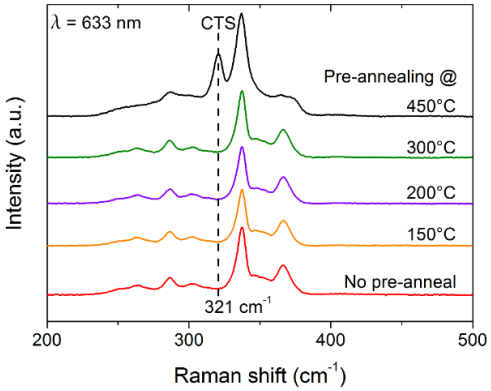

Figure S4 Raman spectra of copper stoichiometric films

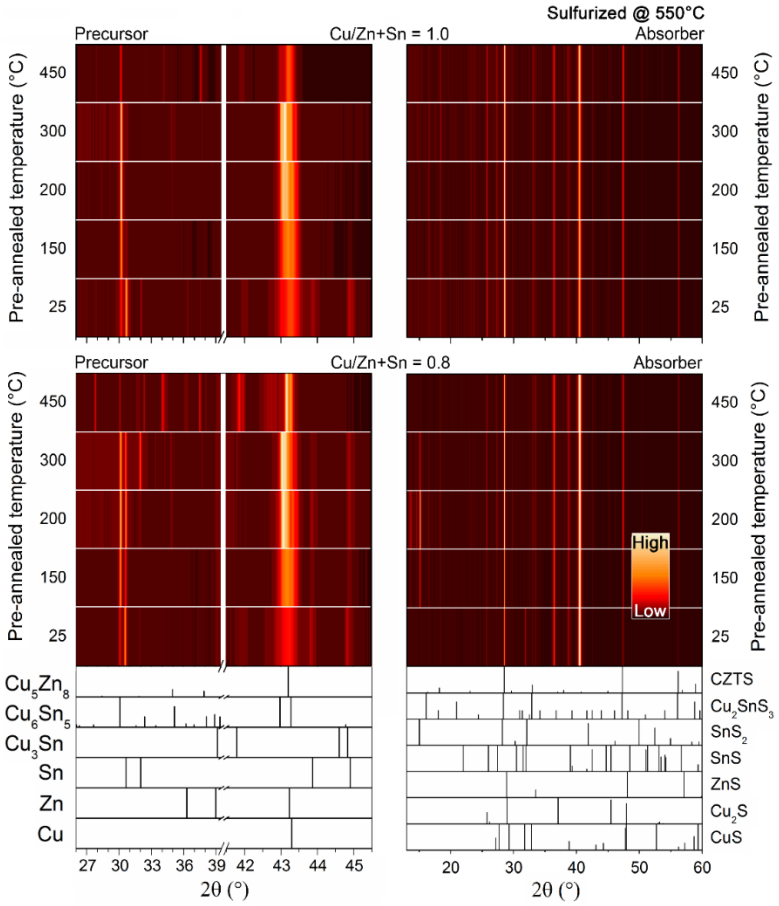

Figure S5 Comparison of XRD patterns of copper poor and stoichiometric precursors and absorbers.

In the copper stoichiometric films, contributions of elemental Sn and Cu_3Sn disappear and Cu_6Sn_5 increases with pre-annealing at 150 °C. Pre-annealing at 200 °C and 300 °C gives similar XRD patterns, peak intensities of Cu-Zn/-Sn alloys increase further, indicating interdiffusion of the

elements. Above the melting point of Sn (230 °C), liquid Sn might help with this diffusion process. At 450 °C, contribution of both Cu-Sn and Cu-Zn alloys in the 42–43° region have reduced intensity and Cu_3Sn re-appears at 42°. In the Cu-Sn phase diagram can be seen that above 408 °C and dependent on the relative composition, Cu_6S_5 is converted into liquid Sn and Cu_3Sn.

With respect to Cu poor films, Sn contributions are only present up to 150 °C. The persistent presence of elemental Sn is expected in copper poor films, because there is higher competition between Sn and Zn to alloy with Cu than in copper stoichiometric films. At 450 °C there are several Cu-Sn peaks in the 27–39° region present which are not present in the stoichiometric films. The peak intensities are higher in the copper poor films.

The XRD patterns of the Cu stoichiometric absorbers are similar. With respect to the Cu poor films, there are no contributions of SnS_2 observed, and a relatively low intensity of SnS. Higher copper content makes it more likely to grow CTS or CZTS phases. Less secondary phases are expected due to its stoichiometric nature of the films.

3.3 Manuscript III – Investigation of reflectometry for *in situ* process monitoring and characterization of co-evaporated and stacked Cu-Zn-Sn-S based thin films

Vacuum deposition techniques can be used to fabricate Cu-Zn-Sn-S based thin films. Unwanted Cu-S and Zn-S phases likely occur due to a preferred Cu-poor composition and a narrow stoichiometric region of Cu_2ZnSnS_4 (kesterite). Reflectometry can be used to determine material properties, such as thickness and band gap. This study investigates whether reflectometry can be employed in situ to monitor presence of unwanted phases such as Cu-S and Zn-S during physical vapour deposition (PVD). A reflectometry setup was designed and integrated with a PVD system to monitor reflection during deposition. The onset of ZnS deposition could be monitored for a Mo/CTS/ZnS multilayer film. Also, it was found that CuS leaves a characteristic dip in ex situ reflection spectra. But this dip could not unambiguously be identified in situ due to the presence of interference fringes during film growth. However, the onset of interference fringes is related to the growth rate and band gap. Therefore, this could be used as a novel in situ fingerprinting method for the deposition of Cu-Zn-Sn-S based thin films.

Publication notification

Title: Investigation of reflectometry for in situ process monitoring and characterization of co-evaporated and stacked Cu-Zn-Sn-S based thin films

Keywords: Kesterite, Phase evolution, Process control, Raman spectroscopy, *in situ* Reflectometry

Authors: Stephan van Duren[1,] , Sergei Levcenco[1], Steffen Kretzschmar[1], Justus Just[1], Thomas Unold[1]
[1]Department Structure and Dynamics of Energy Materials, Helmholtz-Zentrum Berlin, Hahn-Meitner-Platz 1, 14109 Berlin, Germany

Journal: Journal of Alloys and Compounds, Volume 779, 30 March 2019, Pages 870-878
DOI: 10.1016/j.jallcom.2018.11.337

My contribution:
Design, development and integration of the reflectometry setup in a PVD system. Design of the in situ experiments. Performing all in situ and ex situ characterization experiments. All data analysis, majority of simulations and writing of the manuscript.

3.3.1 Abstract

During preparation of compound semiconductor thin films undesired secondary phases and inhomogeneities may occur. Therefore, process control and monitoring are important aspects towards thin film optimization. In this study, white light reflectometry (WLR) was investigated as an in situ non-destructive optical technique to monitor thin films during thermal vacuum evaporation (PVD) of kesterite-type Cu-Zn-Sn-S thin films. The impact of composition on optical properties was studied ex situ by Raman spectroscopy and reflectometry to identify possibilities for in situ detection of secondary phases. A WLR setup was designed and integrated with the PVD system. Four Cu-Zn-Sn-S films were prepared by evaporation and direct reflection was monitored in situ. Reflection spectra were analyzed to identify the influence of process parameters and phases such as CuS and ZnS. Transfer matrix simulations were performed to further explain experimental observations. It is shown that the occurrence of different phases, growth rate/thickness are well related to reflection spectra. Time-dependent reflection spectra reveal specific properties that could serve as characteristic footprints for process control and monitoring. Therefore, this study extends the possibilities for reflectometry as a straightforward, low cost method for in situ process control of Cu-Zn-Sn-S based films.

3.3.2 Introduction

Kesterite, Cu_2ZnSnS_4 or short CZTS, is an interesting material for energy conversion applications due to its non–toxic and earth abundant constituents. Various methods are employed to fabricate kesterite thin films. The most common method is precursor deposition followed by a high temperature annealing step [1–3]. However, decomposition of CZTS and loss of volatile compounds cause inconvenient compositional changes during the process, as well as the formation of secondary phases such as CuS, ZnS and CTS [4,5]. Methods have been developed to remove the superficial occurrence of CuS and ZnS compounds with respectively KCN and HCl etching. This has proven to be beneficial for the solar cell performance[6,7]. However, prevention of secondary phases would be optimal and would contribute to process simplification.

Methods for process control and monitoring can be implemented in order to increase reproducibility and obtain information of thin film properties during the process. In situ XRD has been demonstrated to be able to monitor structural properties [8,9]. Unfortunately, this is a rather complex method when synchrotron radiation is used. Alternatively, optical methods such as Raman spectroscopy and spectral reflectometry might be used as straightforward in situ non-destructive techniques to monitor thin film properties during deposition [10–12]. Thin film properties such as thickness, roughness can be extracted from single

wavelength reflection spectra [10,13,14]. White light reflectometry (WLR) is a method where a broad reflection spectrum as a function of wavelength is recorded. With this method absorber fundamental properties such as band gap and Urbach energy can be extracted [11]. Raman spectroscopy can be used to identify phases and detect and monitor phase transitions in the surface regions. This was demonstrated during high temperature annealing and deposition processes in previous studies [12,15].

In this study, the impact of composition on optical properties and morphology was experimentally investigated for six Cu-Zn-Sn-S absorbers by correlating the compositional ratios to reflection and Raman scattering.

Furthermore, a white light reflection (WLR) setup was integrated in a physical evaporation system (PVD) to provide a method for in situ monitoring and control during the deposition process. Two co-evaporated Cu-Zn-Sn-S films and two multilayer film stacks (Mo/CuS/SnS/CuS/ZnS and Mo/Cu-Sn-S/ZnS) were prepared and WLR was recorded during deposition. For the two Cu-Zn-Sn-S films the Cu-evaporation rate was varied. For the stacked films the effect of sequential deposition on reflection spectra was studied. Optical simulations were performed to investigate and validate the observations in the reflection spectra.

Morphological, structural and vibrational properties of the thin films were investigated by respectively scanning electron microscopy (SEM), X-Ray diffraction (XRD) and Raman spectroscopy (Raman) to support analysis of the

reflection spectra and related optical simulations. Finally, an overall conclusion is formulated on the benefit of using white light reflectometry as an in situ method for process monitoring and control of Cu-Zn-Sn-S based films.

3.3.3 Experimental methods

A physical vapor deposition (PVD) system equipped with copper, zinc and tin effusion cells and a sulfur cracker was used for the preparation of thin films. The PVD setup is schematically shown in Figure 1. The six CZTS films used in the investigation prior to the in situ monitoring experiment were fabricated by co-evaporating Cu-Zn-Sn in a sulfur atmosphere of 1 x 10^{-6} mbar. The substrate heating was set to approximately 550 °C and substrate rotation was used to obtain a uniform film. The composition of the films was obtained by X-ray fluorescence using K-lines of copper and zinc and the tin L-line. Calibration was performed with CZTS films of known composition [16].

An optical WLR setup was designed to monitor reflection during the deposition of thin films. A tungsten-halogen lamp (type SLS201L) was fiber coupled to a dichroic mirror directed towards the center of the substrate. The angle of incidence is $\theta = 37°$. The reflected light was collected in a similar way and transmitted to fiber-coupled spectrometers. To process the full UV-VIS-NIR spectrum an Avantes AvaSpec UVVIS and a NIRQUEST512 from OceanOptics were used. Acquisition time has been kept on

the order of 10–100 ms. The acquired spectra were averaged every eight seconds, one substrate rotation, to reduce systematic intensity fluctuations due to substrate non-idealities. Reflection intensity was calibrated with the molybdenum substrate. The substrate temperature was approximately 200 °C during deposition of these additional four in situ monitored films. Two films were co-evaporated as Cu-Zn-Sn-S (labelled C1 and C2) and two films were deposited as stacks; Mo/CuS/SnS/CuS/ZnS and Mo/Cu-Sn-S/ZnS labelled as S1 and S2 respectively.

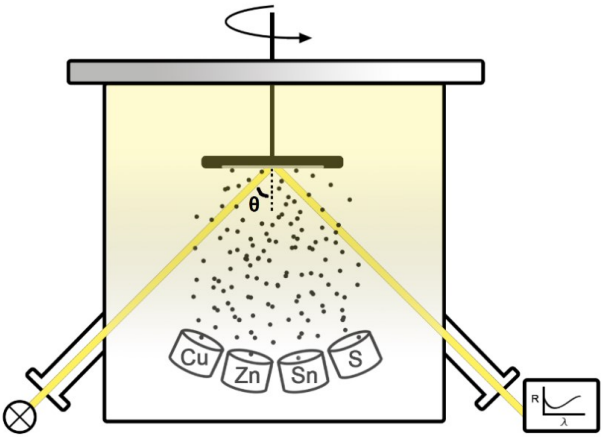

Figure 1 Schematic of the physical vapor deposition system with light source and detector for WLR in situ monitoring. The angle of incidence is equal to θ = 37°.

The structural, vibrational, optical and morphological properties of the films are characterized by X-ray diffraction (XRD) and fluorescence (XRF), Raman spectroscopy, spectrophotometry and scanning electron microscopy (SEM), respectively. The XRD measurement was conducted with a PANalytical X'Pert PRO MRD diffractometer at 2°

grazing incidence geometry, vibrational properties were measured with a Renishaw Raman setup equipped with λ_{exc} = 325 nm, 532 nm and 633 nm lasers, surface morphology was analyzed with a GEMINI electron microscope at 7 kV beam voltage and ex situ reflection spectra were measured with a Perkin Elmer LAMBDA 950 spectrophotometer. Optical simulations were performed with OptiSim [17–25].

3.3.4 Results and discussion

Relation between optical properties, composition and morphology in CZTS absorber films

Prior to the in situ experiments, six absorbers were fabricated and the relation between composition, secondary phases and reflection were analysed.

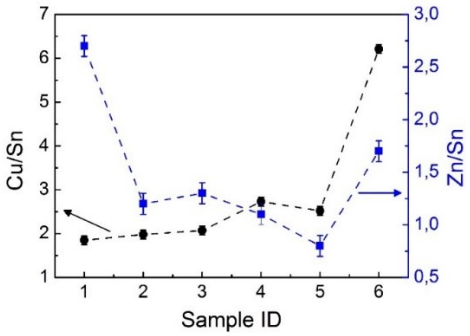

Figure 2 Compositional ratios of six co-evaporated absorbers measured by XRF and are error bars.

Figure 2 gives an overview of the elemental compositions of the samples as obtained by XRF. Since some of the samples

exhibit Cu/ Sn ratios > 2 and Zn/Sn ratios > 1 the presence of CuS and ZnS secondary phases are expected [16].

Figure 3A and B show Raman spectra of the six absorbers excited with λ = 532 nm and 325 nm. The presence of ZnS and CuS can be clearly identified on some of the samples. Interestingly, the Raman peak intensity ratio of CuS/CZTS (475 cm^{-1} /337 cm^{-1}) correlates with Cu/Sn ratio (Figure 3C). At higher Cu/Sn ratios the Cu concentration has increased.

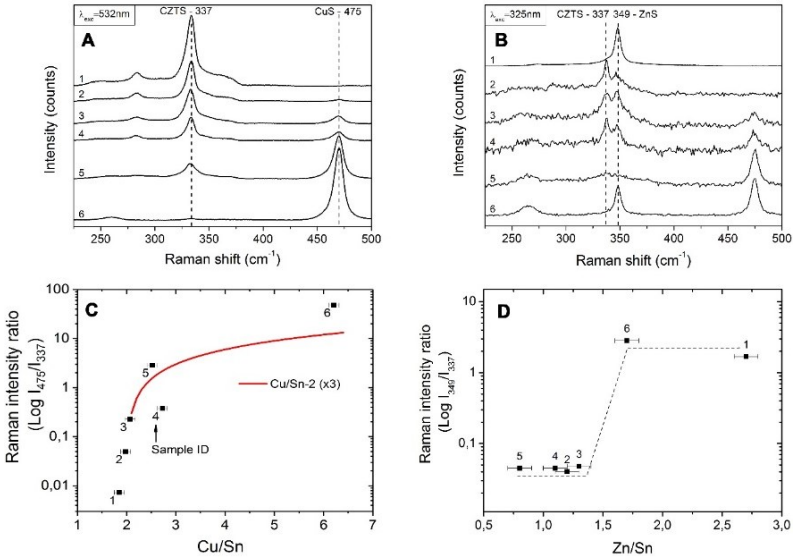

Figure 3 A and B, Raman spectra obtained by using, respectively, λ_{exc} = 532 and 325 nm. (C) Proportionality between the ratio of Raman CuS peak (475 cm^{-1}) and CZTS peak (337 cm^{-1}) intensities is depicted with respect to the Cu/Sn ratio based on (A). (D) Relation between ZnS and CZTS peak ratio I_{349}/I_{337} and Zn/Sn based on (B). The dashed line is a guide to the eye.

Previous results showed that copper rich films, Cu/Sn > 2, will exhibit CuS segregation due to the condition of Cu/Sn ≤ 2 within the CZTS phase [16]. This can be observed in Figure 3C, where the Raman measurement follows a Cu/Sn-2 proportionality.

Figure 3D indicates the relation between the presence of ZnS (349 cm^{-1}), expressed in peak intensity ratio ZnS/CZTS, and compositional ratio Zn/Sn. Changes in the peak ratio occurs more abrupt as opposed to CuS. There seems to be a threshold value where the ZnS signal increases rapidly. The Raman signal intensity related to ZnS is affected by the influence of the resonance condition and is also strongly surface sensitive, because the short penetration depth of the 325 nm laser of 50 nm in CZTS. Thus the absolute magnitude of the Raman signal is mainly affected when there are changes in the ZnS surface segregation. A segregation of ZnS for Zn/Sn ratios > 1 in CZTS was previously determined for thin films by X-ray absorption[16]. Since the Raman measurement is surface-sensitive rather than volume-sensitive and given the error bars, the result of Figure 3D is in good agreement with these previous findings.

Figure 4A shows reflection spectra of the films with different composition as depicted in Figure 2. Absorbers 4 and 4a originate from the same process, except that the latter is etched with KCN to remove CuS. Reflection of a pure CuS reference film is added for comparison. A reflection dip can be observed around λ = 600 nm. The magnitude of this dip strongly depends on the Cu/Sn ratio as follows from the

comparison between the unetched/etched absorbers (sample 4 versus 4a).

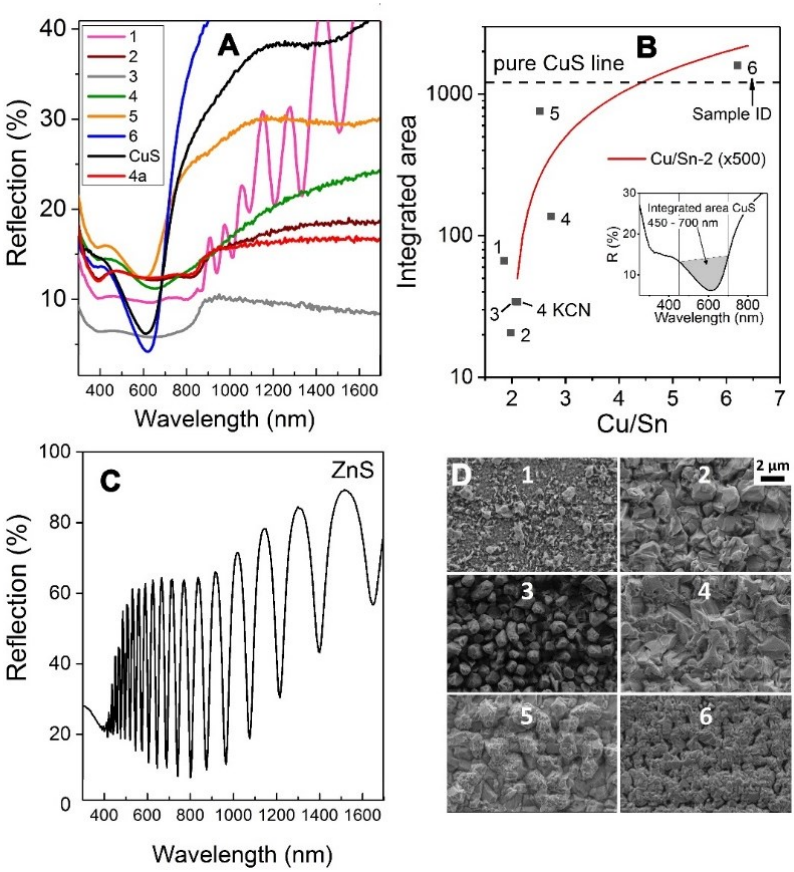

Figure 4 (A) Total reflection spectra of CZTS absorbers with different Cu/Sn ratios compared to a pure CuS film. Sample 4a is the KCN etched sample 4. (B) Integration method applied to absorbers from (A). (C) Reference spectrum of ZnS. (D) SEM surface images of unetched absorbers.

The dip has disappeared in the spectrum of the etched absorber. These results clearly show that a variation in

copper content influences the reflection intensity, in particular in the λ = 450–700 nm regime.

To quantify the presence of the CuS related reflection dip, the area between a straight baseline and the reflection minimum is integrated from λ = 450 nm to 700 nm. The result of such an integration for the films with different Cu/Sn ratios is shown in Figure 4B. It can be seen that the integration value increases strongly with increasing Cu/Sn ratio, proportional to Cu/Sn-2, similarly to the Raman measurement. Figure 4C shows the reflection of a 2µm ZnS reference film. High crystallinity and smooth surface morphology in ZnS films contribute to an interference pattern. Figure 4D depicts the surface morphology of unetched films.

Absorber 1 has a high Zn/Sn ratio and appears to have a smoother surface as opposed to other absorbers. This promotes the occurence of interference. The films 2 to 6 have higher copper content and a grainier surface, reducing the probability of interference. It was found that reflection from films 2 to 5 is almost totally diffuse. Films with higher Zn/Sn ratios, 1 and 6, have increased portions of direct reflection, starting in the infrared region at approximately λ = 800 nm.

Ex situ characterization of in situ monitored co-evaporated and stacked absorber films

The previous section illustrated influences on reflection spectra due to compositional changes and presence of

secondary phases in CZTS films. This section presents ex situ characterization of four different films (CZTS based and stacked films) that were monitored in situ with white light reflection during deposition.

Two co-evaporated films with Cu-Zn-Sn-S (C1 and C2) and two stacks configured as Mo/CuS/SnS/CuS/ZnS (S1) and Mo/Cu-Sn-S/ZnS (S2) were prepared. The total deposition time for C1, C2 and S2 was 45 minutes, with S1 the process time was 15 minutes. Figure 5 shows the XRD patterns and Raman spectra of the four different films. C1 shows reflexes related to SnS and Sn_2S_3 around 30° and a broad contribution at 73°. Additionally, two reflexes at 47.5° and 56.3° are related to CZTS, CTS and ZnS.

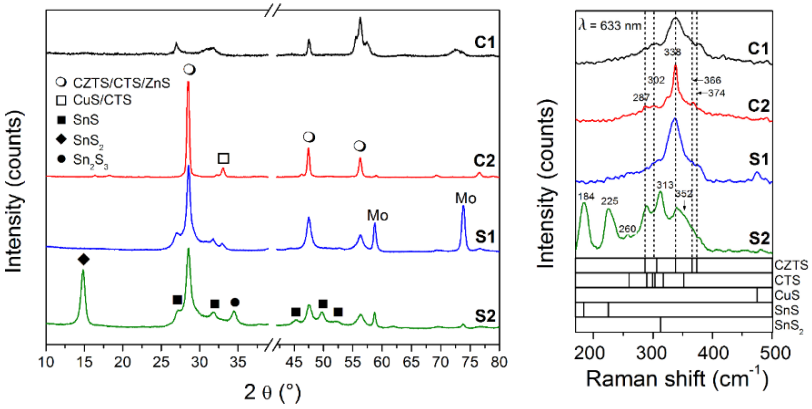

Figure 5 Grazing incidence XRD (2°) patterns and Raman spectra of the evaporated films C1, C2, S1 and S2. A break is inserted in the XRD patterns at the main peak position of Molybdenum at 40.5°. The dashed lines in the Raman spectra indicate CZTS modes.

Note that the XRD pattern of C1 measured in Bragg – Brentano (BB) geometry shows a major 47.5° reflex

associated with 220/204 kesterite planes, which is related to the columnar film structure (see supplementary information for SEM and XRD-BB,Figure 13 and 14). A broad Raman spectrum occurs in the region 300–375 cm^{-1} which confirms presence of CZTS and CTS. Even though the C1 film is Cu/Sn = 0.89 and Sn-S reflexes are observed in the XRD pattern, there is no SnS observed in the surface regions with Raman.

Absorber C2 was deposited with a higher copper evaporation rate and copper rich phases are likely to be present due to the Cu/Sn = 2.67 of this film. Reflexes at 28.5°, 47.5° and 56.3° indicate presence of CTS, CZTS and ZnS. Although this cannot be unambiguously be assigned to one phase due to overlapping patterns. The peak at 32° can be related to CuS or CTS, CZTS and ZnS. CuS is not detected with Raman spectroscopy (475 cm^{-1}) but CZTS is found. The vibrational modes at 287, 302, 338, 366 and 374 cm^{-1} are attributed to kesterite and indicated by dashed lines [26]. The line width of the main CZTS peak at 338 cm^{-1} for C2 is much smaller than for C1 and indicates better crystallinity.

The stacked film S1, Mo/CuS/SnS/CuS/ZnS, shows similarities with absorber C2 in both XRD and Raman spectra. The three main peaks in the XRD pattern are related to CTS, CZTS and ZnS are present and a low intensity reflex from CuS at 32.9°. The vibrational mode of CuS is observed at 475 cm^{-1} which is likely due to unreacted CuS from the stack. The broadening around the 28° peak is caused by several SnS peaks present in this region. Due to a shorter

process time of 15 minutes, the films are thinner than C1, C2 and S2, causing additional molybdenum peaks at 58.7° and 73.8° to be detected. In the Raman spectrum there is a broader peak observed as opposed to film C2. This is likely caused by the simultaneous presence of CTS and CZTS, because CTS has several modes in the region overlapping with CZTS. For example, cubic Cu_2SnS_3 has modes at 299, 303, 352 cm^{-1}, monoclinic Cu_2SnS_3 at 290 and 352 cm^{-1} and tetragonal Cu_2SnS_3 at 317 cm^{-1} [27–29].

The XRD pattern of the Mo/CTS/ZnS film S2 resembles S1. Furthermore, Sn-S phases can be identified. An additional peak is observed at 14.8° and is assigned to SnS_2. As before, the broadening around the 28° peak is caused by the presence of several reflexes of SnS in this region. SnS reflexes occur additionally at 45.3° and 49.8°. The reflex at 34.5° is assigned to Sn_2S_3. The Raman spectrum is a broad spectrum in comparison to the other films. This is caused by a superposition of modes from SnS, SnS_2, CTS and CZTS phases. The modes at 184 and 225 cm^{-1} are related to SnS and the peak at 313 cm^{-1} is related to the main mode of SnS_2 cm^{-1} [30,31]. CTS has several modes in this range overlapping with Sn-S and CZTS. A contribution from different CTS structures occurs between 260 to 352 cm^{-1} and a contribution from CZTS is expected since the interface between CTS and ZnS is close to the surface and ZnS is transparent for λ_{exc} = 633 nm. It is obvious that ZnS is present on the surface being the deposited top layer.

Although Raman measurements show presence of CZTS phase the line-width and number of modes varies in the grown films. For C1 and C2, this corresponds to the compositional variation in the copper content. Also, line broadening is expected because the substrate temperature was around 200 °C and films were not annealed at high temperature (> 450 °C) [28]. Therefore, stimulated elemental diffusion and further crystallisation has not occured. This causes the S1 film to have a single broad CZTS peak and a contribution from CuS. For the S2 film, this results in a variety of contributions from Sn-S, CTS and CZTS phases.

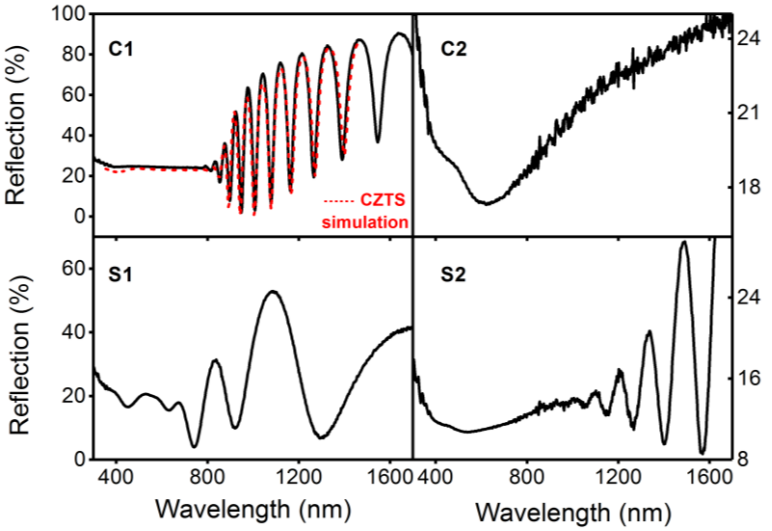

Figure 6 reflection spectra of the four different absorbers at the end of the deposition process. The dashed red line indicates a simulated CZTS spectrum.

Figure 6 shows the total reflection spectra of the four absorbers at the end of the deposition process measured with a Perkin Elmer spectrophotometer. Between C1 and C2,

only the copper evaporation rate was varied and, prior to the process, chosen to be C2 > C1. This resulted in Cu/Sn =0.89 and 2.67 for C1 and C2, respectively, as measured by SEM Energy-dispersive X-ray spectroscopy (EDX). The Zn and Sn evaporation rates were kept the same.

The higher copper evaporation rate during the C2 process resulted in a thicker film than C1, approximately 3 µm and 2 µm, respectively (see supplementary information for SEM). The spectrum of C2 shows a reflection dip around λ = 600 nm (Figure 6). This dip was also observed in the copper rich absorbers and a pure CuS film (Figure 4) and is assigned to the higher copper content.

A simulated spectrum (dashed red line) of a glass/Mo/CZTS film in comparison to C1 is included in Figure 6, with n, k values from literature [32]. The n, k values were shifted by 0.1 eV to lower energy to account for the smaller band gap of the C1 film compared to the reference sample.The thickness for the simulation was based on the SEM image of C1 (Figure 13). An absorber thickness of 2.4 µm and a Molybdenum thickness of 835 nm was used. Since these spectra were taken ex situ, the angle of incidence is normal to the surface. The CZTS simulation matches the C1 spectrum. The spectrum of C1 can be dvided into two sections, up to λ = 700–800 nm the reflection is constant and dominated by specular reflected light. After 800 nm, an interference pattern arises due to the interaction between incident light reflected from the surface and light reflected from the Molybdenum substrate.

The onset of the interference pattern can be used for the estimation of the band gap by drawing an envelope as indicated in Figure 7 [33]. The absorption coefficient is proportional to $\ln[(R(E)-R_{min})^{-1}]$. Here, R(E) represents the mean reflection of the envelope extrema and R_{min} the minimum reflection in the considered spectral range. Figure 7 shows the application of this method and the band gap of the C1 absorber is estimated to be 1.52 eV. Even though the film has a low copper content it corresponds the band gap of a typical CZTS film.

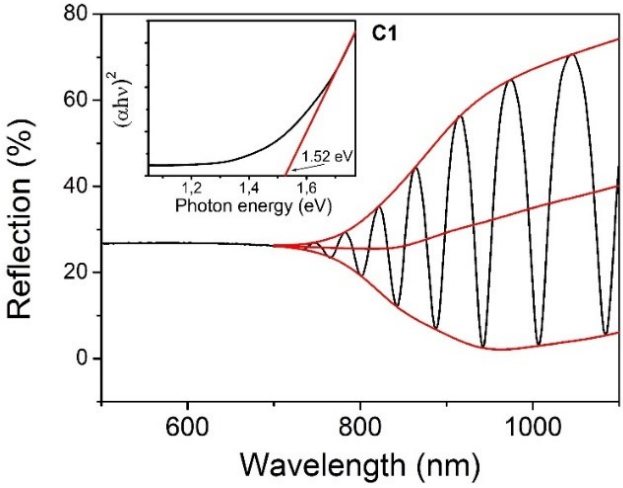

Figure 7 Bandgap estimation based on the envelope drawn around the interference fringes. The inset shows the Tauc plot and indicates the band gap.

Analysis of in situ monitored thin film deposition

During deposition of the four films white light reflection spectra were in situ monitored and are depicted in Figure 8. Accumulation of the reflection spectra are shown as false-

color plots, where the reflection intensity is represented by color. The characteristic pattern of lines, with changing reflection intensities, is caused by the presence of interference fringes in the individual reflection spectra. The onset of the interference fringes changes with increased film thickness.

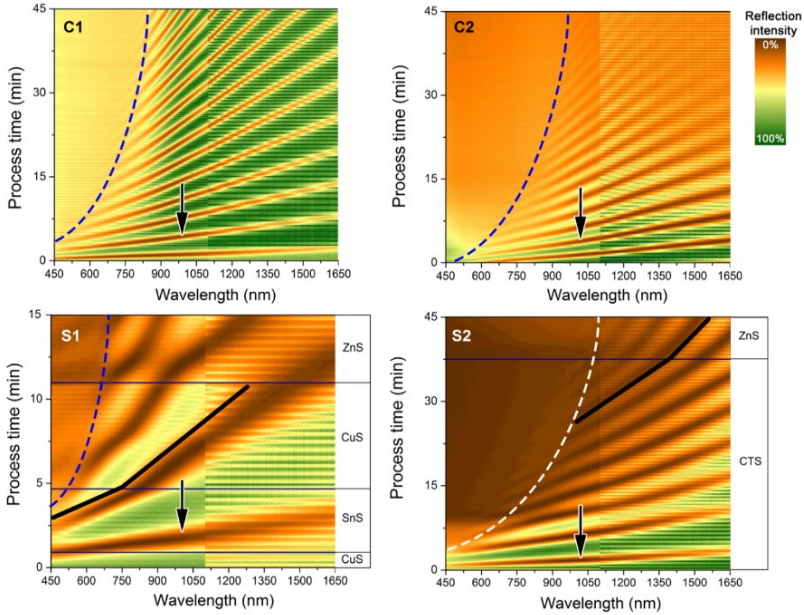

Figure 8 False color plots of white light reflection spectra. C1 and C2 are CZTS films with a difference in the evaporation rate of copper (C2 > C1). While S1 and S2 are deposited as Mo/CuS/SnS/CuS/ZnS and Mo/Cu-Sn-S/ZnS stacks, respectively. The interference fringes, phase deposition changes and inflection point are indicated by arrows, black solid lines and dashed lines, respectively.

The evolution of this inflection point, interference fringes and phase deposition changes are indicated by dashed lines, arrows and black solid lines, respectively. The stacked film

S1 has a final thickness of approximately 600 nm (See SI). The relatively thin film causes interference patterns to occur across the measured spectrum range. The change of the spectrum (Figure 6, S1) is caused by the different refractive indices, layer thicknesses and bandgaps of each material in the Mo/CuS/SnS/CuS/ZnS stack. The refractive index for SnS is between 3 and 4 in the wavelength region 400 to 1700 nm [22]. While Covellite (CuS) varies between 1.2 and 1.5 in the region 400 to 1050 nm [19]. Together with the changing growth rate, this causes the interference minima/maxima to shift at deposition transitions from CuS to SnS and from SnS to ZnS, as indicated by the changing slope of the black lines in Figure 8 for S1.

Inflection point analysis

The dashed lines in Figure 8 indicate the evolution of the interference fringes onset which is related to the thickness/growth rate and band gap of the material. During all processes there is an evolution of this, so called, inflection point. It can be found by drawing an upper and lower envelope function around the reflection curve and taking the difference of the envelopes at each wavelength. The wavelength where the onset occurs can be found when the difference starts to diverge.

The evolution of the inflection point during the process is depicted for all four films in Figure 9 as energy versus process time. It shows that the inflection point is redshifted from C1 to C2 and from C2 to S2. This is explained

by the higher copper content of C2 and a faster growth rate, leading to a thicker film and by S2 being a film consisting of mostly CTS. Reference points can be found by adding the inflection points of simulated spectra at 300 K of CTS and CZTS with different film thicknesses, indicated by the crossed circle and star, respectively. The relative difference between the C1, C2 and S2 films corresponds to the position of these reference values.

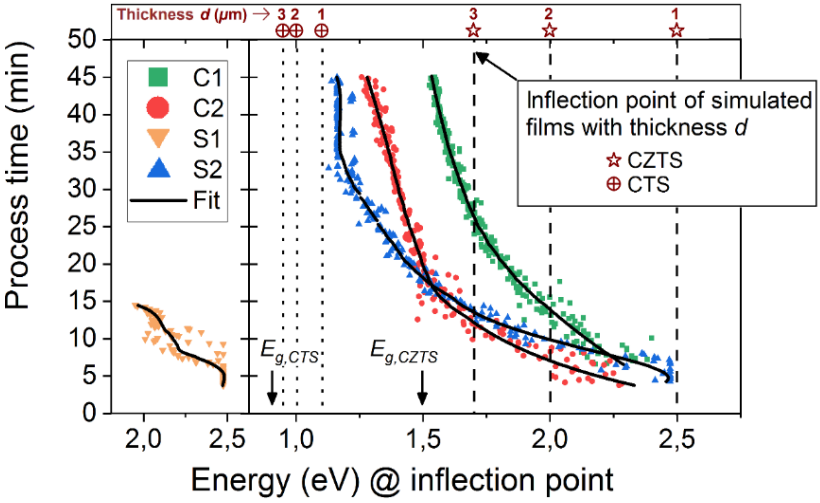

Figure 9 Evolution of the inflection point for all four absorber films C1, C2, S1 and S2. A polynomial function was used for fitting. Inflection points of simulated CTS and CZTS films with different thicknesses are indicated above the graph. The band gaps of monoclinic CTS and CZTS are indicated.

For the films C1, C2 and S2 the evolution is much more defined due to longer process times and, in case of S2, single phase deposition for the first 35 minutes of the process, while S1 consists of sequential deposition of four different

phases within just 15 minutes. Differences between C1, C2 and reference CZTS (star) can be attributed to the elevated growth temperature and difference in composition. For instance, the band gap of CZTS is at ≈1.34 eV at 400 K, which is significantly lower than 1.5 eV at 300 K [34]. The CTS references (crossed circle) lie close to the S2 film, there are several differences between experiment and simulation. The simulation is based on monoclinic CTS and even though S2 exhibits monoclinic CTS (Raman), there are additional phases present. Also, ZnS is deposited after 35 minutes.

These results show that monitoring the inflection point during the deposition process could be used as an in situ fingerprinting method.

Analysis of CuS detection

Despite the presence of the CZTS layer, CuS imposes a strong effect on the reflection spectra, as observed in absorbers with different Cu/Sn ratios (Figure 4). Quantification of this reflection dip is performed with the integration method indicated in Figure 4B. The integration method is applied to the four processes and is depicted in Figure 10. When the formation of CuS occurs it would be noticeable as an increase such as in Figure 4.

The fluctuation at the beginning of the processes is related to the evolution of the interference fringes in the reflection curve as shown in the supplementary part in Figure 15, where modelling of the dependency on the integrated area on different CuS-phases thickness is

performed [19,24,25]. Although presence of CuS at the beginning of the processes is likely, in particular for S2, it cannot unambiguously be determined due to the contribution from interference fringes.

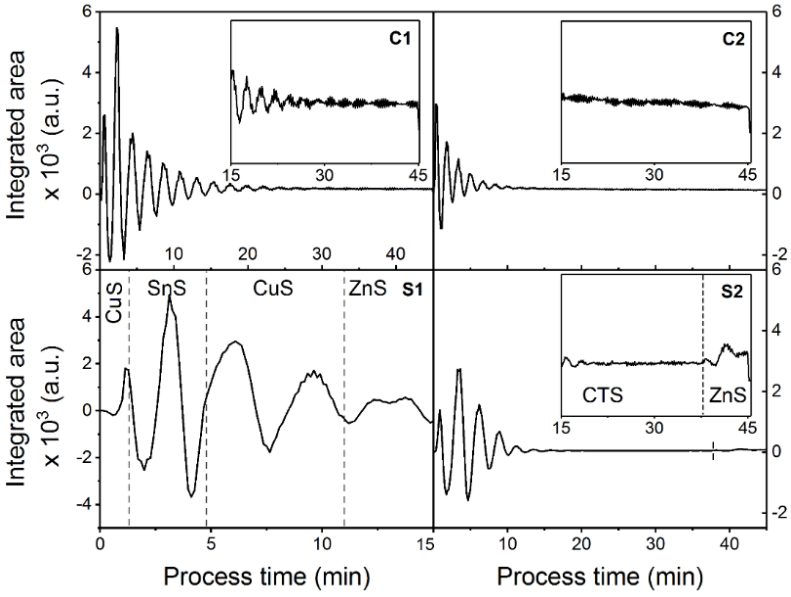

Figure 10 Integrated area below the reflection curve in the λ = 450-700 nm range (as described in section 3.1) for the four processes that were monitored in situ. For S1 and S2, the deposited material is indicated besides the dashed lines.

If CuS precipates later in the process it should be visible by a clear increase in the integrated area. this could also not be observed in the plots of these specific processes. Even though CuS is observed in the XRD measurement (Figure 5, C2, open square icon), Raman measurements do not show superficial presence of CuS (475 cm^{-1}) in the C1, C2 and S2 films. Therefore, it is possibly not detected with this

integration method, when the CuS is located deeper in the film depth. An increase can be observed in the S2 film, however, this is related to the ZnS deposition as will be discussed in the following section.

Even though CuS leaves a dip in the reflection spectra, the integration method did not result in identification of CuS for these specific processes due to the dominant presence of interference fringes and the absence of CuS in some films.

Analysis for detection of ZnS precipitation

Besides the aim to detect CuS it can be seen that the onset of ZnS deposition can be observed in both S1 and S2 (see inset S2, Figure 10) processes by an increase in the integrated area. To further provide insight, the full area below the reflection curve (baseline R = 0) has been integrated for the processes S1 and S2. Note, this is different method than for the CuS reflection dip.

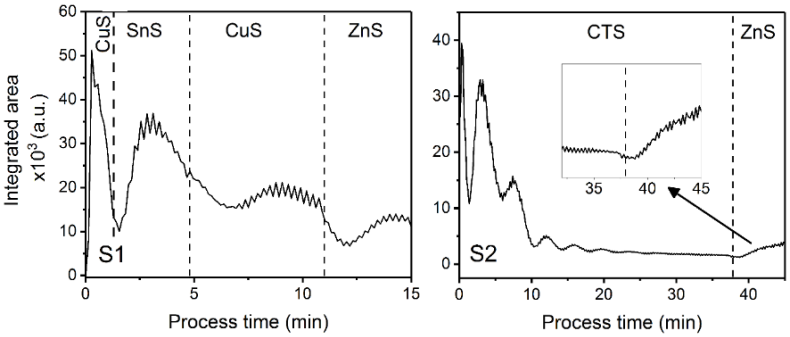

Figure 11 Reflection spectra during the course of the process of absorbers S1 and S2. The area below the reflection curve between 450 and 1100 nm has been integrated, taking R = 0 as baseline. For S2, when the deposition of ZnS begins, the reflection intensity increases, as indicated by the inset.

Figure 11, shows the integrated area between 450 and 1100 nm during the course of the deposition process. When ZnS deposition commences in S2, reflection intensity increases slightly in the visible range. This can also be observed in the false-color plot (Figure 8, S2) where intensity changes accordingly, i.e. becomes brighter. For S1, there is also an increase to be observed.

However, a contribution from the development of interference fringes is more likely here due to the lower thickness and shorter process time.

A possible explanation for the reflection increase observed on commencing ZnS deposition in the S2 absorber, is the smoothening of the surface roughness by ZnS as indicated by a schematic representation shown in Figure 12A. In order to test this hypothesis, simulations were performed with varied roughness of a pure CTS film (Figure 12B) and a Mo/CTS/ZnS stack with different roughness ratios. To assume ZnS smoothening, a roughness ratio CTS/ZnS > 1 was used.

The stacked film S2, Mo/CTS/ZnS, consists of a thick layer of CTS and a thin film of ZnS on top. The total absorber thickness is approximately 2.3 µm (See S.I.). The thickness of the CTS film was estimated to be 2.1 µm and the ZnS thickness 200 nm. The band gap of ZnS is about 3.7 eV, mostly transparent for light above λ = 335 nm. The refractive indices of ZnS and CTS are similar in the considered wavelength range, between 2 and 2.5 [18,20].

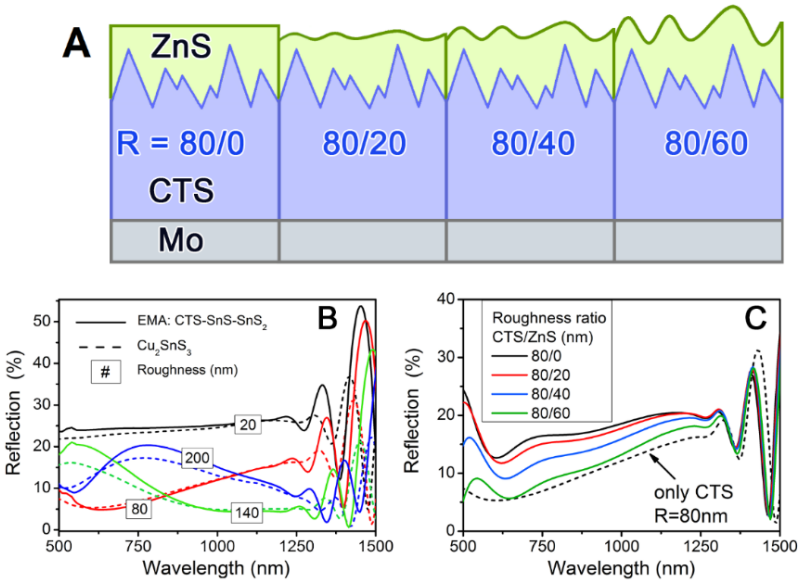

Figure 12 (A) Schematic illustration of cross section of the CTS/ZnS stack. It shows the assumed smoothening by the ZnS film based on the SEM image (Figure 13 SI). (B) Simulation of reflection spectra of a Cu_2SnS_3 film (dashed line) and a film with an EMA refractive index calculated from the mean indices of CTS, SnS and SnS_2 (solid line). The values in de boxes indicate the surface roughness used in the model. (C) shows the simulation of the CTS/ZnS with different roughness ratios (solid lines). The dashed line is the same as red dashed line in (B) and corresponds to CTS with 80 nm roughness, without ZnS.

Since the CTS/ZnS stack is deposited at around 200 °C, other phases such as SnS, SnS_2 are present in the CTS layer as indicated by Raman and XRD (Figure 5). In order to simulate the CTS layer properly, a comparison was made between a pure CTS layer and a layer with an effective medium approximated (EMA) refractive index of SnS, SnS_2 and CTS (Figure 12B). No significant difference was found between different EMA models (mean, Bruggeman and Maxwell-

Garnett) for this particular multilayer stack. Therefore, the mean refractive index was used to calculate the EMA refractive index.

The complex refractive indices in the 400–1700 nm regime for SnS, SnS_2 and CTS are very similar [20,22,23]. For monoclinic CTS, formed at low temperature [35], and SnS the value lies around n = 3 and for SnS_2 between n = 3 and 4. The extinction coefficient k lies for these materials between 0 and 0.8 for all phases. The refractive index of ZnS lies between 2 and 3 in the wavelength regime and k is below 0.02 [18]. Figure 12B shows simulated reflection spectra with varied roughness for the CTS layer. The solid line shows the EMA based CTS layer and the pure CTS is represented by dashed lines. The surface roughness is stated in the boxes. There is a significant difference to be observed between the spectra with different roughness values. The reflection intensity between λ = 500 and 1200 nm fluctuates but decreases with increased roughness from 20 to 200 nm. The onset of the interference pattern starts around λ = 1200 nm for the EMA based film and at λ = 1300 nm for the pure CTS film (dashed). However, there is no substantial difference in reflection between the EMA based and pure CTS layers for a specific roughness value.

In order to estimate the effect of ZnS deposition, a CTS film with 80 nm roughness is taken as a base and a ZnS layer is added with different roughness values. As mentioned, a roughness ratio CTS/ZnS > 1 was used. The simulations are shown in Figure 12C. The simulated spectra

reveal that the increased reflection intensity as a result of ZnS deposition is likely caused by the smoothening of the surface. Detection of ZnS surface precipitation during the annealing/sulfurization of CZTS films [36] would be preferable since ZnS acts as an inactive insulator phase [37]. This *in situ* method could be a first step in the investigation towards detection of ZnS surface precipitation.

3.3.5 Conclusion

This study shows correlations between composition and optical properties by Raman spectroscopy and reflectometry of Cu-Zn-Sn-S based absorbers. It was found that CuS leaves a characteristic reflection dip in the λ = 600 nm regime which can be integrated and was found to be proportional to Cu/Sn-2.

An in situ reflectometry setup coupled to a PVD chamber was designed to investigate this method for in situ process control. CuS could not unambiguously be detected with the integration method in the monitored absorbers, due to the presence of strong interference fringes.

Increased reflection was observed after the deposition of ZnS in Mo/CTS/ZnS stacked films. With simulations this was explained with surface smoothening leading to reduced light scattering and therefore increased direct reflection caused by the ZnS deposition.

Furthermore, the in situ reflection spectra showed a clear evolution of the interference fringes onset, which is

related to the thickness/growth rate and band gap of the films which can be used as an in situ fingerprinting method.

Acknowledgements

The research leading to these results has received funding from the People Program (Marie Curie Actions) of the European Union's Seventh Framework Program FP7/2007-2013/ under REA Grant Agreement No. 316488 (KESTCELLS). The authors wish to thank Dr. J. Scragg at Uppsala University for providing the opportunity to utilize their Raman spectroscopy equipment.

3.3.6 References

[1] S. G. Haass, M. Diethelm, M. Werner, B. Bissig, Y. E. Romanyuk, and A. N. Tiwari, "11.2% Efficient Solution Processed Kesterite Solar Cell with a Low Voltage Deficit," *Adv. Energy Mater.*, vol. 5, no. 18, pp. 1–7, 2015.

[2] R. Juškenas, G. Niaura, Z. Mockus, S. Kanapeckaite, R. Giraitis, R. Kondrotas, A. Naujokaitis, G. Stalnionis, V. Pakštas, and V. Karpavičiene, "XRD studies of an electrochemically co-deposited Cu-Zn-Sn precursor and formation of a $Cu_2ZnSnSe_4$ absorber for thin-film solar cells," *J. Alloys Compd.*, vol. 655, pp. 281–289, 2016.

[3] Y. Ren, J. J. Scragg, T. Ericson, T. Kubart, and C. Platzer Björkman, "Reactively sputtered films in the Cu_xS–ZnS–SnS_y system: From metastability to equilibrium," *Thin Solid Films*, vol. 582, pp. 208–214, 2015.

[4] A. Weber, R. Mainz, and H. W. Schock, "On the Sn loss from thin films of the material system Cu-Zn-Sn-S in high vacuum," *J. Appl. Phys.*, vol. 107, no. 1, 2010.

[5] J. J. Scragg, "Studies of Cu_2ZnSnS_4 films prepared by sulfurisation of electrodeposited precursors," *Thesis*, p. 262, 2010.

[6] H. Xie, Y. Sánchez, S. López-Marino, M. Espíndola-Rodríguez, M. Neuschitzer, D. Sylla, A. Fairbrother, V. Izquierdo-Roca, A. Pérez-Rodríguez, and E. Saucedo, "Impact of Sn (S, Se) Secondary Phases in $Cu_2ZnSn(S, Se)_4$ Solar Cells: a Chemical Route for Their Selective Removal and Absorber Surface Passivation," *ACS Appl. Mater. Interfaces*, vol. 6, no. 15, pp. 12744–12751, 2014.

[7] A. Fairbrother, E. García-Hemme, V. Izquierdo-Roca, X. Fontané, F. A. Pulgarín-Agudelo, O. Vigil-Galán, A. Pérez-Rodríguez, and E. Saucedo, "Development of a Selective Chemical Etch To Improve the Conversion Efficiency of Zn-Rich Cu_2ZnSnS_4 Solar Cells," *J. Am. Chem. Soc.*, vol. 134, no. 19, pp. 8018–8021, 2012.

[8] P. Pistor, R. Mainz, M. D. Heinemann, T. Unold, and R. Scheer, "In Situ Real-Time Characterization of Thin-Film Growth," in *Advanced Characterization Techniques for Thin Film Solar Cells*, Wiley-VCH Verlag GmbH & Co. KGaA, 2016, pp. 441–467.

[9] S. Hartnauer, L. a. Wägele, F. Syrowatka, G. Kaune, and R. Scheer, "Co-evaporation process study of $Cu_2ZnSnSe_4$ thin films by in situ light scattering and in situ X-ray diffraction," *Phys. Status Solidi*, vol. 8, no. 2, p. n/a-n/a, 2014.

[10] R. Scheer, A. Neisser, K. Sakurai, P. Fons, and S. Niki, "$Cu(In_{1-x}Ga_x)Se_2$ growth studies by in situ spectroscopic light scattering," *Appl. Phys. Lett.*, vol. 82, no. 13, p. 2091, 2003.

[11] M. D. Heinemann, R. Mainz, F. Österle, H. Rodriguez-Alvarez, D. Greiner, C. A. Kaufmann, and T. Unold, "Evolution of opto-electronic properties during film formation of complex semiconductors," *Sci. Rep.*, vol. 7, no. April, p. 45463, 2017.

[12] E. Rudigier, B. Barcones., I. Luck, T. Jawhari-Colin, A. Pérez-Rodríguez, and R. Scheer, "Quasi real-time Raman studies on the growth of Cu-In-S thin films," *J. Appl. Phys.*, vol. 95, no. 9, pp. 5153–5158, 2004.

[13] K. Sakurai, R. Hunger, R. Scheer, C. a. Kaufmann, a. Yamada, T. Baba, Y. Kimura, K. Matsubara, P. Fons, H. Nakanishi, and S. Niki, "In situ diagnostic methods for thin-film fabrication: utilization of heat radiation and light scattering," *Prog. Photovoltaics*, vol. 12, no. 2–3, pp. 219–234, 2004.

[14] M. Bär, S. Nishiwaki, L. Weinhardt, S. Pookpanratana, O. Fuchs, M. Blum, W. Yang, J. D. Denlinger, W. N. Shafarman, and C. Heske, "Depth-resolved band gap in Cu (In,Ga) $(S,Se)_2$ thin films," *Appl. Phys. Lett.*, vol. 93, no. 24, 2008.

[15] S. van Duren, Y. Ren, J. Scragg, J. Just, and T. Unold, "In Situ Monitoring of Cu_2ZnSnS_4 Absorber Formation With Raman Spectroscopy During Mo/Cu_2SnS_3/ZnS Thin-Film Stack Annealing," *IEEE J. PHOTOVOLTAICS*, vol. 7, no. 3, pp. 906–912, 2017.

[16] J. Just, C. M. Sutter-Fella, D. Lützenkirchen-Hecht, R. Frahm, S. Schorr, and T. Unold, "Secondary phases and their influence on the composition of the kesterite phase in CZTS and CZTSe thin films," *Phys. Chem. Chem. Phys.*, vol. 18, no. 23, pp. 15988–15994, 2016.

[17] M. Richter, M. S. Hammer, T. Sonnet, and J. Parisi, "Bandgap extraction from quantum efficiency spectra of Cu(In,Ga)Se_2 solar cells with varied grading profile and diffusion length," *Thin Solid Films*, vol. 633, pp. 213–217, 2017.

[18] M. Querry, "Optical constants of minerals and other materials from the millimeter to the ultraviolet." 1987.

[19] S. H. Chaki, M. P. Deshpande, and J. P. Tailor, "Characterization of CuS nanocrystalline thin films synthesized by chemical bath deposition and dip coating techniques," *Thin Solid Films*, vol. 550, no. January, pp. 291–297, 2014.

[20] A. Crovetto, R. Chen, R. B. Ettlinger, A. C. Cazzaniga, J. Schou, C. Persson, and O. Hansen, "Dielectric function and double absorption onset of monoclinic Cu_2SnS_3: Origin of experimental features explained by first-principles calculations," *Sol. Energy Mater. Sol. Cells*, vol. 154, pp. 121–129, 2016.

[21] H. Zhao and C. Persson, "Optical properties of Cu(In,Ga)Se_2 and Cu2ZnSn(S,Se)$_4$," *Thin Solid Films*, vol. 519, no. 21, pp. 7508–7512, 2011.

[22] A. Abou Shama and H. M. Zeyada, "Electronic dielectric constants of thermally evaporated SnS thin films," *Opt. Mater. (Amst).*, vol. 24, no. 3, pp. 555–561, 2003.

[23] C. Raisin, Y. Bertrand, and J. Robin, "Comparison of optical properties and band structures of $SnSe_2$ and SnS_2," *Solid State Commun.*, vol. 24, no. 4, pp. 353–356, 1977.

[24] B. J. Mulder, "Optical Properties of an Unusual Form of," *Phys. Status Solidi*, vol. 15, pp. 409–413, 1973.

[25] B. J. Mulder, "Optical Properties of Crystals of Cuprous Sulfieds (Chalcosite, Djurleite, CuS and Digenite," *Phys. Status Solidi*, vol. 13, pp. 79–88, 1972.

[26] M. Dimitrievska, A. Fairbrother, X. Fontané, T. Jawhari, V. Izquierdo-Roca, E. Saucedo, and A. Pérez-Rodríguez, "Multiwavelength excitation Raman scattering study of polycrystalline kesterite Cu_2ZnSnS_4 thin films," *Appl. Phys. Lett.*, vol. 104, no. 2, p. 021901, 2014.

[27] P. A. Fernandes and P. M. P. Salom, "A study of ternary Cu_2SnS_3 and Cu_3SnS_4 thin films prepared by sulfurizing stacked," vol. 215403.

[28] S. van Duren, Y. Ren, J. Scragg, J. Just, and T. Unold, "In Situ Monitoring of Cu_2ZnSnS_4 Absorber Formation With Raman Spectroscopy During," vol. 3, no. 3, pp. 1–7, 2017.

[29] D. M. Berg, R. Djemour, L. Gütay, S. Siebentritt, P. J. Dale, X. Fontane, A. Pérez-rodriguez, "Raman analysis of monoclinic Cu_2SnS_3 thin films Raman analysis of monoclinic Cu_2SnS_3 thin films," vol. 192103, no. 2012, 2016.

[30] Y. Ren, N. Ross, J. K. Larsen, K. Rudisch, J. J. S. Scragg, and C. Platzer-Björkman, "Evolution of Cu_2ZnSnS_4 during Non-Equilibrium Annealing with Quasi-in Situ Monitoring of Sulfur Partial Pressure," *Chem. Mater.*, vol. 29, no. 8, pp. 3713–3722, 2017.

[31] A. Alvarez, S. Exarhos, and L. Mangolini, "Tin disulfide segregation on CZTS films sulfurized at high pressure," *Mater. Lett.*, vol. 165, no. November, pp. 41–44, 2016.

[32] S. Levcenko, E. Hajdeu-Chicarosh, E. Garcia-Llamas, R. Caballero, R. Serna, I. V. Bodnar, I. A. Victorov, M. Guc, J. M. Merino, A. Pérez-Rodriguez, E. Arushanov, and M. León, "Spectroscopic ellipsometry study of Cu_2ZnSnS_4 bulk poly-crystals," *Appl. Phys. Lett.*, vol. 112, no. 16, p. 161901, Apr. 2018.

[33] V. Kumar, S. Kr, T. P. Sharma, and V. Singh, "Band gap determination in thick fims from reflectance measurements," vol. 12, pp. 115–119, 1999.

[34] P. K. Sarswat and M. L. Free, "A study of energy band gap versus temperature for Cu_2ZnSnS_4 thin films," *Phys. B Condens. Matter*, vol. 407, no. 1, pp. 108–111, 2012.

[35] N. R. Mathews, J. Tamy Benítez, F. Paraguay-Delgado, M. Pal, and L. Huerta, "Formation of Cu_2SnS_3 thin film by the heat treatment of electrodeposited SnS-Cu layers," *J. Mater. Sci. Mater. Electron.*, vol. 24, no. 10, pp. 4060–4067, 2013.

[36] W. Li, J. Chen, C. Yan, and X. Hao, "The effect of ZnS segregation on Zn-rich CZTS thin film solar cells," *J. Alloys Compd.*, vol. 632, pp. 178–184, 2015.

[37] A. Nagoya, R. Asahi, and G. Kresse, "First-principles study of Cu_2ZnSnS_4 and the related band offsets for photovoltaic applications," *J. Phys. Condens. Matter*, vol. 23, no. 40, 2011.

3.3.7 Supplementary information

Morphology

Figure 13 shows SEM images of the four films. The C1 absorber exhibits a columnar structure, while absorber C2 is thicker due to the increased copper evaporation rate and has a different grain morphology. The difference in process time between S1 and S2 clearly effects the film thickness. For S1, the contrast changes from halfway and upwards of the film and might indicate transition between phases. This area is indicated by the light blue shaded area. The S2 film has a clear bi-layer structure, the CTS part shows a closely packed thorn-like structure with a thin layer of ZnS on top.

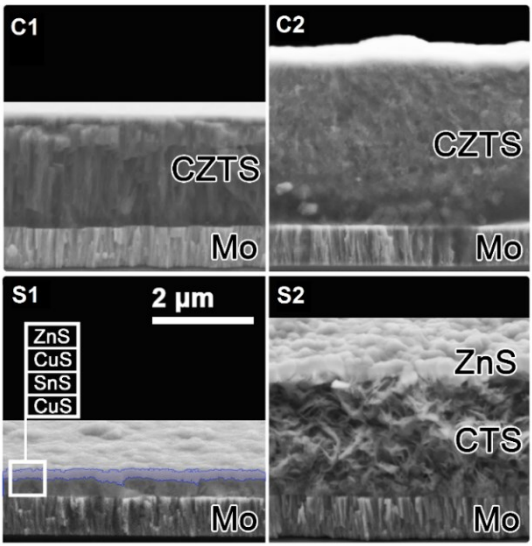

Figure 13 SEM images of the in situ WLR monitored thin films. Note that SEM images S1 and S2 are slightly viewed at an angle, C1 and C2 are depicted from the side.

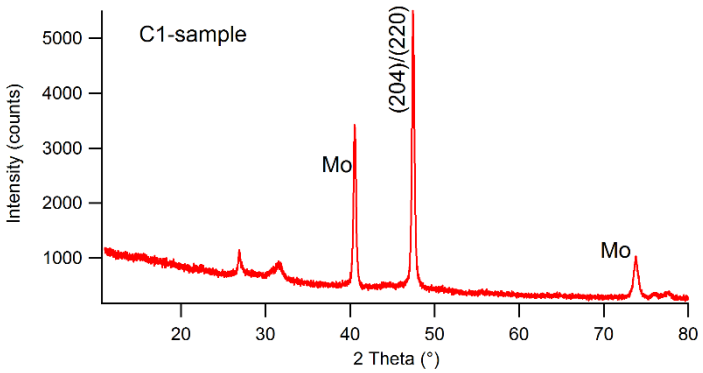

Figure 14 XRD pattern in Bragg Brentano geometry of the evaporated C1-film. Indicated are Mo and CZTS reflex of 204/220

Figure 14 shows the XRD pattern of sample C1. Figure 15 depicts the integration method applied to thickness simulations of different CuS phases

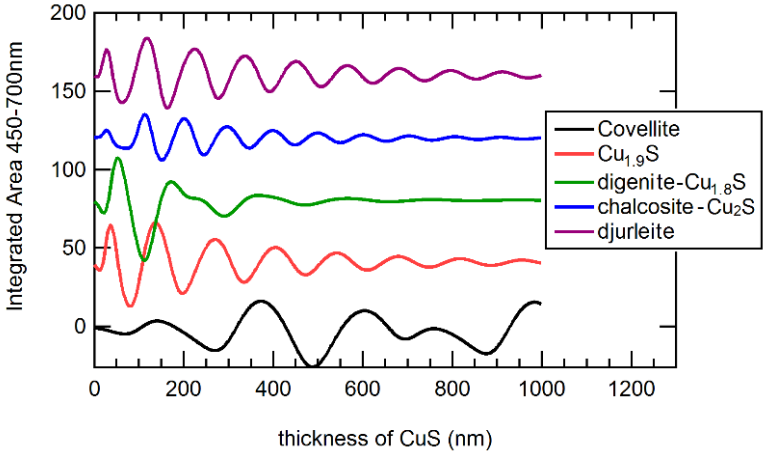

Figure 15 Simulation of the reflection dip area in the 450-700nm range for the different thickness of the CuS layer on the Mo (835 nm) coated glass

4 Conclusions and outlook

In the past decade, research on CZTS has become attractive due to its potential as a sustainable, non-toxic alternative for CIGS. Even though tremendous progress has been made on processing and fundamental knowledge of CZTS films, IBM's record of a 12.6 % CZTSSe solar cell has not yet been broken. Most characterization and analysis occurs on the finished thin films and devices. As such, in situ monitoring and control could possibly lead to optimization of processing steps for Cu-Sn-Zn-S based thin films.

This work investigated Raman spectroscopy, XRD and reflectometry for their potential to in situ monitor and control important deposition and annealing processing steps in Cu-Zn-Sn-S based thin films. These methods were chosen since they were found as common ex situ characterization methods for thin film properties investigations.

With in situ Raman spectroscopy, vibrational modes of both CTS and CZTS can be observed during high temperature (up to 550 °C) annealing. A remarkable result is the observation of CZTS formation from a Mo/CTS/ZnS multi-layer film. Research groups that report their processing method for CZTS show little information on the time point of CZTS formation. In Cu-poor CZTS films, secondary phases, reproducibility and homogeneity are often challenges, dependent on the processing method. However, the amount of secondary phases can possibly be

reduced by resolving the optimum annealing time such that decomposition of CZTS is reduced. Raman spectroscopy could provide a method to obtain this information.

Dependent on the deposition system or annealing strategy, temperature measurement can be inaccurate. Thermocouples are often used in vacuum deposition or annealing systems but not integrated in the substrate heater. Therefore, the position of the thermocouple influences the temperature measurement. The thermocouple in the Raman heating stage was integrated in the substrate heater providing an accurate temperature control. It was found that the main vibrational mode of CZTS is linearly proportional to temperature in the range of 50–550 °C. This could be used as a calibration method to indirectly monitor temperature during annealing and growth processes.

Future work on in situ Raman spectroscopy could be focused on the integration of in situ Raman spectroscopy during annealing in real processing environments such as a regular tube furnace or a vacuum deposition chamber. The latter was demonstrated before in $CuInSe_2$. Practical challenges are related to a.o. working distance, signal-to-noise ratio and a gaseous atmosphere. The latter might contaminate the optical objective, unless heated appropriately. For sulfurization in a tube furnace a proper graphite box should be designed such that the sample can be monitored. Visible access to the sample can possibly be obtained through fiber optics.

Some research groups apply post annealing treatments in air and Raman could be helpful in understanding possible phase transitions at the surface during air annealing. The approach in this thesis was done with a single wavelength (532 nm laser). It would be interesting to develop a multiwavelength setup because some phases are more sensitive to certain wavelengths. For example, a laser with λ_{exc}= 325 nm enhances vibrational modes of ZnS due to resonance effects. It should be mentioned that Raman spectroscopy is typically a localized measurement on the area of few μm^2. A mapping setup could serve to monitor spatial inhomogenieties and a multi-laser setup would support detection of secondary phases and CZTS simultaneously. Dependent on the Raman scattering intensity of the material, the acquisition times may differ from real time to seconds or minutes.

Several groups incorporate pre-annealing of metal precursors. Usually it is not stated why a specific temperature is employed. In this study, a temperature range was used to pre-anneal metal precursors. It was found that Cu-Sn alloys and elemental Sn in Cu-poor precursor films are key factors that determine the formation of SnS_2 in the absorber which is detrimental for solar cell efficiency. The best cell did not exhibit SnS_2 phases in the absorber and resulted in 4 % efficiency. Since several groups reported presence of SnS phases, it would be beneficial to investigate in situ XRD and determine the optimum temperature in their respective precursor annealing regime. Finding the optimum

annealing temperature could reduce or avoid elemental Sn and Cu-Sn in the precursor. Additionally, when fabricating the absorber, in situ Raman could be used to obtain the point of formation of SnS_2 and other secondary phases on the surface.

Reflectometry was investigated as a third method for process control. Reflection was found to strongly depend on the copper content in CZTS films. CuS leaves a characteristic dip at about 600 nm in the reflection spectrum. This can be correlated to the Cu/Sn ratio by using an integration method. An in situ reflectometry setup was designed and integrated in a PVD system. The CuS dip could not be observed due to the occurrence of interference fringes. The deposition of thin films with different layers and compositions resulted in characteristic time dependent reflection spectra. The inflection point where interference fringes commence, can be monitored during the deposition process. Since this inflection point is related to the band gap and thickness of the deposited film, it can be used as a characteristic fingerprinting method for thin films. Furthermore, the onset of ZnS deposition in a CTS/ZnS multilayer film could be observed due to reduced surface roughness caused by ZnS deposition.

Currently, four processes were carried out with in situ reflectometry. It was found that these four films leave characteristic fingerprints. The monitoring of different materials can lead to a range of fingerprints serving as a reference database. Extending with CZTS thin films of a wide

compositional range would also further improve the validity of the method. In this setup only direct reflection was measured. In order to measure scattered reflection, one could upgrade the system with a second detector to measure reflection at oblique angle.

With respect to time resolution, reflectometry can be performed in a matter of milliseconds. While time resolution for Raman and XRD depend on the material properties. For typical setups used in this study, it is in the range of seconds to minutes. The low Raman scattering intensity imposes a trade off between time and spectral resolution. With XRD, time resolution also imposes constraints on the pattern range and resolution. Therefore, the pattern range of interest should be chosen wisely to reduce acquisition time and increase suitability for in situ monitoring. For in situ reflectometry, direct reflected light is reduced in rough films that scatter light strongly and may impose restrictions on signal intensity. With respect to working distance, reflectometry and XRD can be used from a relatively long distance (meter) as opposed to Raman spectroscopy (centimeter/millimeter). Unlike XRD or reflectometry, with Raman spectroscopy a laser power study should always be done prior to a measurement in order to prevent thermal effects from the laser.

Three characterization methods were investigated for in situ monitoring during annealing and vacuum deposition of Cu-Sn-Zn-S based thin films with respect to structural properties, secondary phases, temperature, thickness and

band gap. The methods operate at different temporal and spatial resolution and can be used complementary. The results of this thesis can lead to optimization and improved reproducibility of crucial processing steps and possibly break the current 12.6 % solar efficiency barrier for CZTS films.

5 References

[1] United Nations, “World Population Prospects: Main Results,” Popul. Facts, no. 2, pp. 1–4, 2011.

[2] Stocker and V. B. and P. M. M. (eds. . T.F., D. Qin, G.-K. Plattner, M. Tignor, S.K. Allen, J. Boschung, A. Nauels, Y. Xia, “Summary for Policymakers. In: Climate Change 2013: The Physical Science Basis. Contribution of Working Group I to the Fifth Assessment Report of the Intergovernmental Panel on Climate Change,” CEUR Workshop Proc., vol. 1542, pp. 33–36, 2015.

[3] I. E. A. (IEA), “Energy Statistics,” 2017.

[4] A. Polman, M. Knight, E. C. Garnett, B. Ehrler, and W. C. Sinke, “Photovoltaic materials: Present efficiencies and future challenges,” Science (80-.)., vol. 352, no. 6283, 2016.

[5] A. Nagoya, R. Asahi, R. Wahl, and G. Kresse, “Defect formation and phase stability of Cu_2ZnSnS_4 photovoltaic material,” Phys. Rev. B - Condens. Matter Mater. Phys., vol. 81, no. 11, pp. 1–4, 2010.

[6] I. D. Olekseyuk, I. V. Dudchak, and L. V. Piskach, “Phase equilibria in the Cu_2S-ZnS-SnS_2 system,” J. Alloys Compd., vol. 368, no. 1–2, pp. 135–143, 2004.

[7] A. Nagoya, R. Asahi, and G. Kresse, “First-principles study of Cu_2ZnSnS_4 and the related band offsets for photovoltaic applications,” J. Phys. Condens. Matter, vol. 23, no. 40, 2011.

[8] H. Katagiri, K. Jimbo, M. Tahara, H. Araki, and K. Oishi, “The influence of the composition ratio on CZTS-based thin film solar cells” Mater. Res. Soc. Symp. Proc. Vol. 1165, vol. 1165, pp. 1165-M04-01, 2009.

[9] S. G. Haass, M. Diethelm, M. Werner, B. Bissig, Y. E. Romanyuk, and A. N. Tiwari, “11.2% Efficient Solution Processed Kesterite Solar Cell with a Low Voltage Deficit,” Adv. Energy Mater., vol. 5, no. 18, pp. 1–7, 2015.

[10] W. Wang, M. T. Winkler, O. Gunawan, T. Gokmen, T. K. Todorov, Y. Zhu, and D. B. Mitzi, “Device characteristics of CZTSSe thin-film solar cells with 12.6% efficiency,” Adv. Energy Mater., vol. 4, no. 7, pp. 1–5, 2014.

[11] S. Chen, A. Walsh, X. G. Gong, and S. H. Wei, “Classification of lattice defects in the kesterite Cu_2ZnSnS_4 and $Cu_2ZnSnSe_4$ earth-abundant solar cell absorbers,” Adv. Mater., vol. 25, no. 11, pp. 1522–1539, 2013.

[12] A. Weber, R. Mainz, and H. W. Schock, “On the Sn loss from thin films of the material system Cu-Zn-Sn-S in high vacuum,” J. Appl. Phys., vol. 107, no. 1, 2010.

[13] J. J. Scragg, T. Ericson, T. Kubart, M. Edoff, and C. Platzer-Björkman, “Chemical Insights into the Instability of Cu_2ZnSnS_4 Films during Annealing,” Chem. Mater., vol. 23, no. 20, pp. 4625–4633, 2011.

[14] J. Scragg, J. Wätjen, and M. Edoff, “A detrimental reaction at the molybdenum back contact in $Cu_2ZnSn(S, Se)_4$ thin-film solar cells,” Journal of the American Chemical Society, vol. 134, no. 47, pp. 19330–3, 2012.

[15] A. Fairbrother, X. Fontané, V. Izquierdo-Roca, M. Espíndola-Rodríguez, S. López-Marino, M. Placidi, L. Calvo-Barrio, A. Pérez-Rodríguez, and E. Saucedo, “On the formation mechanisms of Zn-rich Cu_2ZnSnS_4 films prepared by sulfurization of metallic stacks,” Sol. Energy Mater. Sol. Cells, vol. 112, pp. 97–105, 2013.

[16] H. Xie, Y. Sánchez, S. López-Marino, M. Espíndola-Rodríguez, M. Neuschitzer, D. Sylla, A. Fairbrother, V. Izquierdo-Roca, A. Pérez-Rodríguez, and E. Saucedo, “Impact of Sn (S, Se) Secondary Phases in $Cu_2ZnSn(S, Se)_4$ Solar Cells: a Chemical Route for Their Selective Removal and Absorber Surface Passivation,” ACS Appl. Mater. Interfaces, vol. 6, no. 15, pp. 12744–12751, 2014.

[17] Y. Ren, M. Richter, J. Keller, A. Redinger, T. Unold, O. Donzel-Gargand, J. J. S. Scragg, and C. Platzer Björkman, “Investigation of the SnS/Cu_2ZnSnS_4 Interfaces in Kesterite Thin-Film Solar Cells,” ACS Energy Lett., vol. 2, no. 5, pp. 976–981, 2017.

[18] A. Fairbrother, E. García-Hemme, V. Izquierdo-Roca, X. Fontané, F. A. Pulgarín-Agudelo, O. Vigil-Galán, A. Pérez-Rodríguez, and E. Saucedo, “Development of a Selective Chemical Etch To Improve the Conversion Efficiency of Zn-Rich Cu_2ZnSnS_4 Solar Cells,” J. Am. Chem. Soc., vol. 134, no. 19, pp. 8018–8021, 2012.

[19] B. A. Schubert, B. Marsen, S. Cinque, T. Unold, R. Klenk, S. Schorr, and H. W. Schock, “ Cu_2ZnSnS_4 thin film solar cells by fast coevaporation,” Prog. Photovoltaics Res. Appl., vol. 19, no. 1, pp. 93–96, 2011.

[20] Y. Ren, J. J. Scragg, T. Ericson, T. Kubart, and C. Platzer Björkman, “Reactively sputtered films in the Cu_xS–ZnS–SnS_y system: From metastability to equilibrium,” Thin Solid Films, vol. 582, pp. 208–214, 2015.

[21] R. Kondrotas, R. Juškenas, A. Naujokaitis, G. Niaura, Z. Mockus, S. Kanapeckait, B. Čechavičius, K. Juškevičius, E. Saucedo, and Y. Sánchez, “Investigation of selenization process of electrodeposited Cu-Zn-Sn precursor for $Cu_2ZnSnSe_4$ thin-film solar cells,” Thin Solid Films, vol. 589, no. August, pp. 165–172, 2015.

[22] L. Vauche, L. Risch, Y. Sánchez, M. Dimitrievska, M. Pasquinelli, T. Goislard de Monsabert, P.-P. Grand, S. Jaime-Ferrer, and E. Saucedo, “8.2% pure selenide kesterite thin-film solar cells from large-area electrodeposited precursors,” Prog. Photovoltaics Res. Appl., vol. 24, no. July 2015, p. 38, 2015.

[23] D. M. Berg, M. Arasimowicz, R. Djemour, L. Gütay, S. Siebentritt, S. Schorr, X. Fontané, V. Izquierdo-roca, A. Pérez-rodriguez, and P. J. Dale, “Discrimination and detection limits of secondary phases in Cu_2ZnSnS_4 using X-ray diffraction and Raman spectroscopy,” Thin Solid Films, vol. 569, pp. 113–123, 2014.

[24] M. Espindola-Rodríguez, J. López-García, D. Sylla, X. Fontané, Y. Sánchez, S. López-Marino, V. Izquierdo-Roca, W. Riedel, W. Ohm, S. Gledhill, O. Vigil-Galán, and E. Saucedo, “ Cu_2ZnSnS_4 absorber layers deposited by spray pyrolysis for advanced photovoltaic technology,” Phys. Status Solidi Appl. Mater. Sci., vol. 212, no. 1, pp. 126–134, 2015.

[25] R. Scheer, A. Pérez-Rodríguez, and W. K. Metzger, “Advanced diagnostic and control methods of processes and layers in CIGS solar cells and modules,” Prog. Photovoltaics Res. Appl., vol. 18, no. 6, pp. 467–480, 2010.

[26] K. Sakurai, R. Hunger, R. Scheer, C. a. Kaufmann, a. Yamada, T. Baba, Y. Kimura, K. Matsubara, P. Fons, H. Nakanishi, and S. Niki, “In situ diagnostic methods for thin-film fabrication: utilization of heat radiation and light scattering,” Prog. Photovoltaics, vol. 12, no. 2–3, pp. 219–234, 2004.

[27] M. D. Heinemann, R. Mainz, F. Österle, H. Rodriguez-Alvarez, D. Greiner, C. A. Kaufmann, and T. Unold, “Evolution of opto-electronic properties during film formation of complex semiconductors,” Sci. Rep., vol. 7, no. April, p. 45463, 2017.

[28] M. A. Olgar, J. Klaer, R. Mainz, S. Levcenco, J. Just, E. Bacaksiz, and T. Unold, “Effect of precursor stacking order and sulfurization temperature on compositional homogeneity of CZTS thin films,” Thin Solid Films, vol. 615, pp. 402–408, 2016.

[29] E. Rudigier, I. Luck, and R. Scheer, “Quality assessment of $CuInS_2$-based solar cells by Raman scattering,” Appl. Phys. Lett., vol. 82, no. 24, p. 4370, 2003.

[30] M. Dimitrievska, A. Fairbrother, X. Fontané, T. Jawhari, V. Izquierdo-Roca, E. Saucedo, and A. Pérez-Rodríguez, “Multiwavelength excitation Raman scattering study of polycrystalline kesterite Cu_2ZnSnS_4 thin films,” Appl. Phys. Lett., vol. 104, no. 2, p. 021901, 2014.

[31] P. A. Fernandes and P. M. P. Salom, “A study of ternary Cu_2SnS_3 and Cu_3SnS_4 thin films prepared by sulfurizing stacked,” vol. 215403.

[32] P. Pistor, R. Mainz, M. D. Heinemann, T. Unold, and R. Scheer, “In Situ Real-Time Characterization of Thin-Film Growth,” in Advanced Characterization Techniques for Thin Film Solar Cells, Wiley-VCH Verlag GmbH & Co. KGaA, 2016, pp. 441–467.

[33] J. Márquez, H. Stange, C. J. Hages, N. Schaefer, S. Levcenko, S. Giraldo, E. Saucedo, K. Schwarzburg, D. Abou-Ras, A. Redinger, M. Klaus, C. Genzel, T. Unold, and R. Mainz, “Chemistry and Dynamics of Ge in Kesterite: Toward Band-Gap-Graded Absorbers,” Chem. Mater., vol. 29, no. 21, pp. 9399–9406, 2017.

[34] G. Kaune, S. Hartnauer, and R. Scheer, “In situ XRD investigation of $Cu_2ZnSnSe_4$ thin film growth by thermal co-evaporation,” Phys. Status Solidi Appl. Mater. Sci., vol. 211, no. 9, pp. 1991–1996, 2014.

[35] S. van Duren, Y. Ren, J. Scragg, J. Just, and T. Unold, “In Situ Monitoring of Cu_2ZnSnS_4 Absorber Formation With Raman Spectroscopy During Mo/Cu_2SnS_3/ZnS Thin-Film Stack Annealing,” IEEE J. PHOTOVOLTAICS, vol. 7, no. 3, pp. 906–912, 2017.

[36] A. Fairbrother, V. Izquierdo-Roca, X. Fontané, M. Ibáñez, A. Cabot, E. Saucedo, and A. Pérez-Rodríguez, “ZnS grain size effects on near-resonant Raman scattering: optical non-destructive grain size estimation,” CrystEngComm, vol. 16, no. 20, p. 4120, 2014.

[37] M. Richter, M. S. Hammer, T. Sonnet, and J. Parisi, “Bandgap extraction from quantum efficiency spectra of Cu(In,Ga)Se_2solar cells with varied grading profile and diffusion length,” Thin Solid Films, vol. 633, pp. 213–217, 2017.

[38] C. C. Katsidis and D. I. Siapkas, “General transfer-matrix method for optical multilayer systems with coherent, partially coherent, and incoherent interference,” Appl. Opt., vol. 41, no. 19, p. 3978, Jul. 2002.

[39] S. J. Byrnes, “Multilayer optical calculations arXiv : 1603 . 02720v2 [physics . comp-ph] 28 Aug 2016,” pp. 1–20, 2016.

[40] S. M. Sze and K. K. Ng, Physics of Semiconductor Devices. Hoboken, NJ, USA: John Wiley & Sons, Inc., 2006.

[41] D. Abou-Ras, T. Kirchartz, and U. Rau, Advanced Characterization Techniques for Thin Film Solar Cells. Weinheim, Germany: Wiley-VCH Verlag GmbH & Co. KGaA, 2016.

6 List of abbreviations and symbols

AM1.5	Air Mass ratio 1.5
a-Si	Amorphous silicon
α	Absorption coefficient
CCD	Charge-coupled device
CIGS	$CuInGaSe_2$
c-Si	Crystalline silicon
CTS	Cu-Sn-S
CZTS/Se	Kesterite, Cu_2ZnSnS_4/Se_4
d	Thickness
δ	Phase shift
η	Efficiency, see also PCE
EDX/EDS	Energy Dispersive X-Ray Spectroscopy
Eg	Band gap
EMA	Effective Medium Approximation
FF	Fill Factor
GIXRD	Grazing Incidence X-Ray Diffraction
h	Planck constant
HZB	Helmholtz-Zentrum Berlin
ICP-OES	Inductively Coupled Plasma Optical Emission Spectroscopy
ICSD	Inorganic Crystal Structure Database
ITO	Indium Tin Oxide
IREC	Catalonia Institute for Energy Research

IV	Current-Voltage characterisation
I_F	Intensity of light travelled through film once
I_S	Intensity of light directly reflected from surface
I_{tot}	Total light intensity directly reflected
I_0	Total incident light intensity
J_{SC}	Short circuit current
J	Current density
J_{MP}	Current density at Maximum Power Point
k	Extinction coefficient; imaginary part of refractive index
k_B	Boltzmann constant
λ	Wavelength
λ_{exc}	Laser excitation wavelength
mc-Si	Multi-crystalline silicon
MPP	Maximum Power Point
MRD	Materials Research Diffractometer
n_c	Complex refractive index of layer *c* = 0,1,2,..
n	Real part of refractive index Positive integer in Braggs law Ideality factor in Diode equation
υ	Wave frequency
nc-SI	Nano-crystalline silicon
NIR	Near infrared
PCE	Photo Conversion Efficiency
PV	Photovoltaics
PVD	Physical Vapour Deposition
q	Elementary charge

QD	Quantum Dots
R_S , T_S	Reflection, transmission coefficient at air/film interface
R_D , T_D	Reflection, transmission coefficient at air/film interface (diffuse/scattered)
R_M	Reflection coefficient at film/molybdenum interface
R_{tot}	Reflection Fresnel coefficient
R_{series}	Series Resistance
R_{shunt}	Shunt/Parallel Resistance
SEM	Scanning Electron Microscopy
σ	Root mean square roughness
θ_0	Angle of incidence
θ_1	Angle of refraction
t_{acq}	Acquisition time
T	Temperature
T_F	Transmission coefficient at film/air interface
UU-ASC	Uppsala University Ångström Solar Center
UV	Ultraviolet
VIS	Visible
V_{oc}	Open circuit voltage
V	Voltage
V_{MP}	Voltage at Maximum Power Point
WLR	White Light Reflectometry
XRD	X-Ray Diffraction
XRF	X-Ray Fluorescence

7 Acknowledgements

First of all I would like to thank the people who gave me the opportunity to continue my interest for research in the field of material science, solar energy and engineering. I am thankful to the project coordinators of KESTCELLS, Dr. Edgardo Saucedo and Dr. José Miguel Sanjuan. To my supervisor, Dr. Thomas Unold, for letting me carry out my research project in his group at the Helmholtz-Zentrum in Berlin. I am grateful for the constructive discussions to the approach of the research project and discussions to sharpen the interpretation of the results. I am grateful for Prof. Dr. Aleksander Gurlo at the Technical University to facilitate my pursuit for a PhD in his group.

I am thankful for all the people within the HZB Energy Materials department, especially Sergej Levcenco and Anastasia Irkhina for the good atmosphere and many discussions related to research and life in general. A special word of thanks to Lars Steinkopf, for his sense of humor and because he was there to assist with solving technical challenges of the PVD system, anytime. Also thanks to Justus Just, Steffen Kretzschmar and Marc Heinemann for the good times and discussions on optics and other science topics. Also, I would like to thank Pascal Becker for the German translation of the summary. I am also grateful to the members of the KESTCELLS project, in particular all my

fellow ESRs, for the collaborations, discussions and good times.

Furthermore, I would like to thank some people for being very helpful and hospitable during my research visits. At Uppsala university, thanks to the members in the department of Engineering Sciences, in particular Dr. Jonathan Scragg, Prof. Dr. Charlotte Platzer-Björkman and Dr. Yi Ren. Thanks to Dr. José Maria Delgado Sanchez and Dr. Rémi Anitat from Soland R&D Center at Abengoa Research. And thanks to all the people of the Solar energy group at IREC, with a special thanks to Dr. Diouldé Sylla, Dr. Mirjana Dimitrievska and Dr. Victor Izquierdo-Roca.

Also, I would like to thank the people that contributed to shape me into the person who I am today. The people and friends I grew up with, in high school and college. My former colleagues. My parents, sister, brother and other family members. And all the people and friends I have met and made during my PhD, with their interesting stories and different backgrounds. Thanks a lot!

Finally, I am very grateful to have a wonderful woman by my side, who has supported me unconditionally throughout the years. Even though we lived separately most of the time during my PhD project, we became even more closely connected. In this period I have realized that it is very special to be with you. And I am looking forward to the many joyful years to come. Thank you Marijke :)

Stephan van Duren

Schriftenreihe **Advanced Ceramic Materials**
Hrsg.: Prof. Dr. Aleksander Gurlo
ISSN 2569-8303 (print)
ISSN 2569-8338 (online)

1: Colmenares, Maria: Ordered mesoporous silica COK-12: mesoscale tailoring, upscaling, continuous synthesis and application in the oxidative coupling of methane. - 2018. - xx, 180 S.
ISBN **978-3-7983-2988-1** (print) EUR **12,00**
ISBN **978-3-7983-2989-8** (online)
DOI 10.14279/depositonce-6744

Universitätsverlag der TU Berlin

Keramische Werkstoffe

Development of in situ methods for process monitoring and control and characterization of Cu-Zn-Sn-S based thin films

In recent years, kesterite Cu_2ZnSnS_4 (CZTS) has become an interesting alternative to copper indium gallium (di)selenide (CIGS) and cadmium telluride (CdTe) due to its non-toxic and earth abundant constituents. A variety of methods is being used to fabricate kesterite thin films, such as coevaporation, sputtering, electrodeposition and spray pyrolysis. Most of them include a high temperature annealing step to stimulate elemental mixing and interdiffusion. Experimental and theoretical studies are needed to investigate the effect of the occurrence of unwanted phases and detrimental defects on the electronical properties of the CZTS based solar devices. In this work non-destructive techniques are investigated and developed for in situ process control and monitoring of Cu-Zn-Sn-S based thin films. In particular, Raman spectroscopy, X-ray diffraction and reflectometry are investigated to study and optimize crucial processing steps such as metal precursor pre-annealing, high temperature annealing and vacuum deposition of Cu-Zn-Sn-S based thin films.

ISBN 978-3-7983-3064-1 (print)
ISBN 978-3-7983-3065-8 (online)

ISBN 978-3-7983-3064-1

http://verlag.tu-berlin.de